LBL-14285

LBL--14285

DE82 016940

PHOTOELECTRON SPECTROSCOPY OF SUPERSONIC MOLECULAR BEAMS

James Edward Pollard

Ph.D. Thesis

Materials and Molecular Research Division
Lawrence Berkeley Laboratory
and
Department of Chemistry
University of California
Berkeley, California 94720

May 1982

DISCLAIMER

This work is supported by the Director, Office of Energy Research, Office of Basic Energy Sciences, Chemical Sciences Division of the U.S. Department of Energy under Contract No. DE-AC03-76SF00098.

PHOTOELECTRON SPECTROSCOPY OF SUPERSONIC MOLECULAR BEAMS

Contents

ABSTRACT vii

I. MOTIVATIONS AND CHRONOLOGY 1

References 5

II. DESIGN OF THE INSTRUMENT 6

Abstract 6

A. Introduction 7

B. Design Criteria 8

C. Description of the MBPES Machine 11

1. Vacuum System and Beam Source 11

2. Photon Sources 13

3. Electron Energy Analyzer 15

4. Electron Lenses 22

5. Detection System 25

6. Data Acquisition 27

D. Performance 28

References 32

Tables 35

Figure Captions 36

Figures 40

III. ROTATIONALLY-RESOLVED PHOTOELECTRON SPECTROSCOPY OF n-H_2, p-H_2, HD, and D_2 59

Abstract 59

A. Introduction..... 60

B. Experimental..... 62

C. Results and Discussion..... 65

1. Spectra..... 65

2. Energy Scale..... 67

3. Vibrational Energy Levels..... 67

4. Vibrational Cross Sections..... 72

5. Rotational Energy Levels..... 78

D. Summary..... 79

References..... 81

Tables..... 84

Figure Captions..... 95

Figures..... 97

IV. ROTATIONALLY-RESOLVED PHOTOELECTRON ANGULAR DISTRIBUTIONS FOR $H_2^+(v'=0)$ AT λ = 584Å and 736Å..... 115

Abstract..... 115

A. Introduction..... 116

B. Experimental..... 118

C. Results and Discussion..... 119

D. Conclusion..... 122

References..... 123

Tables..... 125

Figure Captions..... 127

Figures..... 128

V. ROTATIONAL RELAXATION IN SUPERSONIC BEAMS OF HYDROGEN BY HIGH RESOLUTION PHOTOELECTRON SPECTROSCOPY..... 131

Abstract..... 131

A. Introduction..... 132

B. Experimental..... 134

C. Results..... 137

1. n-H_2 and n-D_2..... 137

2. HD..... 140

3. Modeling the Relaxation of p-H_2..... 141

References..... 146

Tables..... 148

Figure Captions..... 150

Figures..... 152

VI. CONCLUSIONS..... 163

ACKNOWLEDGMENTS..... 168

PHOTOELECTRON SPECTROSCOPY OF SUPERSONIC MOLECULAR BEAMS

James Edward Pollard

Materials and Molecular Research Division
Lawrence Berkeley Laboratory
and
Department of Chemistry
University of California
Berkeley, California 94720

ABSTRACT

A new technique for performing high resolution molecular photoelectron spectroscopy is described, beginning with its conceptual development, through the construction of a prototypal apparatus, to the initial applications on a particularly favorable molecular system. The distinguishing features of this technique are: 1) the introduction of the sample in the form of a collimated supersonic molecular beam, and 2) the use of an electrostatic deflection energy analyzer which is carefully optimized in terms of sensitivity and resolution. This combination makes it possible to obtain photoelectron spectra at a new level of detail for many small molecules. Three experiments are described which rely on the capability to perform rotationally-resolved photoelectron spectroscopy on the hydrogen molecule and its isotopes. The first is a measurement of the ionic vibrational and rotational spectroscopic constants and the vibrationally-selected photoionization cross sections. The second is a determination of the photoelectron asymmetry parameter, β, for selected rotational

transitions. The third is an investigation of the rotational relaxation in a free jet expansion, using photoelectron spectroscopy as a probe of the rotational state population distributions. In the closing chapter an assessment is made of the successes and limitations of the technique, and an indication is given of areas for further improvement in future spectrometers.

I. MOTIVATIONS AND CHRONOLOGY

Molecular photoelectron spectroscopy was discovered approximately twenty years ago and has been used in a large number of laboratories to study the electronic structure of small molecules and ions. Monochromatic UV light, typically with a photon energy of $h\nu = 21.2$ eV, ionizes the molecules in a gaseous sample, and the kinetic energy (E_K) spectra of the resulting photoelectrons are measured, thereby determining the ionization energy (E_I) spectra through the energy balance equation,

$$h\nu = E_I + E_k \tag{1}$$

The work of many researchers in this field has been summarized in several standard texts, the most notable of which are those by Rabalais[1] and by Berkowitz.[2] The typical information derived from these experiments consists of: 1) the ionization energies for the accessible electronic states of the molecular ion at an accuracy of about 10 meV, which are usually compared with Koopmans' theorem ionization energies derived from semiempirical or <u>ab initio</u> electronic structure calculations; and 2) a qualitative picture of the relative photoionization cross sections leading to the various ionic states. Clearly there is a great deal more that could be learned if one could fully resolve the vibrational and rotational structure which underlies most unresolved photoelectron bands. The quality of the experiment

would also benefit from improvements in the signal-to-background ratio, which has traditionally been low enough to obscure many weak (but interesting) spectral features, and to limit the accuracy of the relative cross sections by necessitating a tricky background subtraction.

The present work represents an attempt to come to grips with a number of major obstacles to further progress which had not been seriously addressed since the instrumentation in the field reached its initial maturity in the late 1960's. The design goals for the new instrument described here were: 1) to obtain an electron energy resolution of 10 meV or better, 2) to obtain sufficient sensitivity to work with the number density available in a collimated supersonic molecular beam, 3) to obtain a high signal-to-background ratio, 4) to maintain the transmission of the analyzer relatively constant as a function of kinetic energy, and 5) to protect the critical components of the analyzer from surface contamination by active gases. The spectrometer which was finally produced succeeded in meeting most of the design goals, but not without leaving room for further improvements. In many respects the course which we took had been charted in a 1978 review article by Eland,[3] in which he had predicted that the next major advance would be made by a spectrometer which used a supersonic beam source and a large mean-radius double-electrostatic-deflector with multichannel detection. The present aim was not so much to perform a set of experiments on a particular molecular system (although this thesis is rather narrowly focused on hydrogen), as to build a

general purpose apparatus which would be useful in a variety of applications. We also wished to demonstrate the feasibility of several rather risky design innovations which could serve as benchmarks for future work.

There now follows a brief chronology of the principal events related to this project. The design work on the analyzer began in January 1979 and required about six months to complete. Fabrication began in April of that year. In September 1979 the lenses and preanalyzer were tested in the chamber for the first time. The hemispherical analyzer was first tested with single channel detection in March 1980. A 16:1 two-element lens was initially used between the preanalyzer and the hemispheres, but its poor focusing properties prevented us from obtaining the desired electron energy resolution. Much better performance was achieved with a three-element 8:1 lens which was designed and built in June 1980. During the remainder of 1980 high resolution (ca. 10 meV) spectra of several molecules were recorded with single channel detection. The LSI-11/2 microcomputer was installed in October 1980. The newly designed helium lamp was built and installed in November 1980. The multichannel detector was first tested in an external chamber with an electron gun in April 1980, but the problems encountered with the initial design were not overcome until November 1980. A milestone was reached in January 1981 with the first tests of the hemispherical analyzer with multichannel detection. Experiments with the excimer laser were performed from February through May 1981. The experiments reported in this thesis were carried out between July and December 1981.

The structure of subsequent chapters is as follows. Chapter II is a detailed description of the design of the spectrometer. Chapter III deals with the spectroscopy and photoionization cross sections of hydrogen. Chapter IV covers the rotationally-resolved angular distributions. Chapter V deals with the rotational relaxation of hydrogen in a supersonic expansion. Chapter VI evaluates the performance of the spectrometer with an emphasis on directions for future work.

II. DESIGN OF THE INSTRUMENT*

ABSTRACT

A high resolution photoelectron spectrometer which uses molecular beam sampling is described. Photons from a rare-gas resonance lamp or UV laser are crossed with the beam from a differentially pumped supersonic nozzle source. The resulting photoelectrons are collected by an electrostatic analyzer of a unique design consisting of a 90° spherical sector pre-analyzer, a system of lenses, and a 180° hemispherical deflector. A multichannel detection system based on dual microchannel plates with a resistive anode position encoder provides an increase in counting efficiency by a factor of 12 over the equivalent single channel detector. The apparatus has demonstrated an instrumental resolution of better than 10 meV FWHM, limited largely by the photon source linewidth. A quadrupole mass spectrometer is used to characterize the composition of the molecular beam. Extensive differential pumping is provided to protect the critical surfaces of the analyzer and mass spectrometer from contamination. Because of the near elimination of Doppler and rotational broadenings, the practical resolution is the highest yet obtained in molecular PES.

A. INTRODUCTION

Supersonic beams have achieved considerable popularity in molecular spectroscopy because of their potential for improved resolution and because of the access they afford to the study of weakly-bound complexes. Laser-induced fluorescence of supersonic jets is being used in several laboratories to obtain accurate spectroscopic information on simple van der Waals molecules[1,2] and to study intramolecular energy transfer in larger systems.[3,4] Multiphoton ionization spectroscopy of jet-cooled molecules is being exploited both for the purposes of spectral simplification and to perform linewidth studies.[5,6] The combination of a molecular beam with a vacuum ultraviolet monochromator makes it possible to carry out high resolution photoionization mass spectrometry on small molecules and clusters.[7,8]

Molecular photoelectron spectroscopy (PES) could also be expected to benefit by the application of molecular beams, and progress has been made, both with the PES of clusters[9-11] and in the pursuit of higher resolution.[12,13] A major difficulty in molecular beam photoelectron spectroscopy (MBPES) is the rather low number density (10^{12}-10^{13} cm^{-3}) in the ionization region as compared to that typically used in a gas cell PES machine (10^{14}-10^{15} cm^{-3}). Consequently it has not been feasible until now to work at the best attainable instrumental resolution for reasons of sensitivity. Further, a problem relating specifically to the study of weakly-bound complexes arises because the composition of the molecular beam is rather uncertain in the absence of characterization by mass spectrometry.

We describe here an apparatus designed to make MBPES a more viable technique by overcoming the above difficulties. This MBPES machine also represents a considerable improvement over previous spectrometers in the areas of background reduction and protection from surface contamination.

Design criteria are developed in Section B. In Section C the MBPES machine is described in detail with a subsection devoted to each component. In Section D the performance of the apparatus is evaluated in light of the design criteria.

B. DESIGN CRITERIA

The factors limiting resolution in MBPES were discussed by Dehmer and Dehmer[12] in connection with their work on jet-cooled ethylene. The principal contributions to the observed resolution (FWHM) are included in the expression

$$\Delta E_{obs} = [\Delta E_0^2 + (\Delta E_{photon})^2 + (\Delta E_{Doppler})^2 + (\Delta E_{rotation})^2 + (\Delta E_{fields})^2]^{1/2} \quad , \qquad (1)$$

where ΔE_0 is the theoretical FWHM of the analyzer, ΔE_{photon} is the linewidth of the photon source, $\Delta E_{Doppler}$ is the Doppler broadening, $\Delta E_{rotation}$ is the broadening due to rotational excitation of the target molecules, and ΔE_{fields} is a term combining the effects of

non-ideal spectrometer behavior. In the latter category are the sources of broadening due to power-supply instability, stray magnetic and RF electric fields, surface contamination and charging, field-fringing effects in the analyzer and lenses, and energy-scale shifts from contact potential variations during successive scans. For a spectrometer of moderate resolution ($\Delta E_0 \geq 20$ meV) all terms except ΔE_0 can usually be neglected when using a rare-gas resonance lamp. However, for high-resolution work any of these factors can become the major contributor to ΔE_{obs}, and careful attention must be paid to each.

Supersonic beams provide the most direct method for the elimination of Doppler broadening, by sampling the photoelectrons in a direction perpendicular to the molecular beam axis. Because of the drastic cooling accompanying adiabatic expansion, rotational broadening can also be significantly reduced in MBPES. Molecular beam sources offer the additional advantage of protection from surface contamination, because very effective vacuum isolation can be maintained between the ionization region and the interior of the analyzer, by one or more stages of differential pumping.

The best reported photoelectron energy resolution is 4 meV, for an atomic Ar sample using Ne(I) radiation,[14] for which Doppler and rotational effects do not contribute. By using a supersonic beam and by taking great care to minimize broadening due to the photon source linewidth and to non-ideal behavior, it should also be possible to approach this resolution for molecular systems. Thus it seems

practical to set a design goal resolution of less than 5 meV for an MBPES machine. The rather low number density available in the beam (ca. 10^{13} cm^{-3}) makes it imperative that the analyzer have good collection efficiency if high resolution operation is to be realized. In addition, it is necessary to reduce the background signal from electrons scattered by grids or surfaces, which frequently limits the sensitivity of conventional analyzers. These considerations led us to choose an optimized double electrostatic deflector with a position-sensitive multichannel detection system. It is desired that the transmission of the analyzer be fairly constant over a scan in which the measured kinetic energy varies by up to a factor of 10. There also should be provision for operation over a rather wide range of pass energies to allow for flexibility in the selection of resolution and counting rate. These requirements call for the design of a lens system of greater sophistication than has traditionally been employed. The materials used in the construction of the analyzer should be non-permeable, should show uniform surface potentials, and preferably should be bakeable to maintain a clean ultrahigh vacuum environment. Extensive magnetic shielding is mandated by the need to operate at low pass energies.

A knowledge of what species are present in the molecular beam is essential for the study of weakly-bound complexes. Mass spectrometry using a photoionization source is the most direct method for obtaining this information. Although our uncertainty about the degree of dissociative photoionization often precludes a definitive characterization

of the beam, a mass spectrometer should certainly be of great assistance in optimizing the expansion conditions to suit the production of a particular cluster.

C. DESCRIPTION OF THE MBPES MACHINE

In this section we describe in detail the design of a spectrometer which embodies the criteria set forth in the previous section. A subsection is devoted to each of the principal components of the machine.

1. Vacuum system and beam source.

The apparatus as shown in Fig. 1 is based on a 16-inch diameter stainless steel cross for the main vacuum chamber, with allowance for access by the beam source, the electron energy analyzer, and the quadrupole mass spectrometer. These three flange-mounted units are equipped with individual differential pumping facilities. The main chamber is pumped by two liquid-nitrogen-baffled diffusion pumps (Varian VHS-6) with a combined speed of 1800 ℓsec^{-1}. A conical beam catcher mounted atop one of the pumps was found to be of no benefit except at rather low gas throughput.

The beam source consists of a 70 μm diameter nozzle and a 1.1 mm diameter x 6.4 mm tall skimmer (nozzle-to-skimmer distance = 6.4 mm), backed by an unbaffled 4000 $\ell\ sec^{-1}$ diffusion pump and a 1250 cfm (590 $\ell\ sec^{-1}$) Roots blower. The nozzle may be cooled by a liquid-nitrogen-filled jacket or heated up to 400°C by a noninductively-wired

Nichrome heater cable. For a typical stagnation pressure of 1000 Torr at 25°C, the nozzle throughput is 0.6 Torr ℓ sec^{-1}, the exhaust chamber pressure is 1.5 x 10^{-4} Torr, and the main chamber pressure is 2.0 x 10^{-5} Torr. The efficiency of the molecular beam sampling is measured by the ratio of the photoelectron signal from the beam to that from background gas, which has a typical value of 10-20 under these conditions. For helium-seeded beams this ratio increases due to the concentration of the more massive component near the central beam axis. The maximum beam intensity is limited by scattering of the expanding gas in front of the skimmer when the local pressure becomes too large. Beyond this point the photoelectron signal actually drops when the stagnation pressure is increased further as the collimation of the beam is degraded.

A differentially pumped nozzle source possesses certain advantages over the simple free jet for PES experiments. The primary advantage is the reduction of the background gas load into the main chamber, which eliminates the problem of photoelectrons being scattered by background molecules and also reduces the threat of surface contamination in the analyzer. To achieve a good number density it is necessary to place the free jet source very close to the ionization region, leading to possible effects from surface charging and making the heating and cooling of the nozzle more problematic. In our source the differential pumping wall and the nozzle are 1.9 cm and 3.2 cm from the ionization region, respectively.

The mass spectrometer (Extranuclear Laboratories) is connected with the main chamber through a 0.64 cm diameter aperture for passage by the ions and is pumped by a 500 $\ell\,sec^{-1}$ turbomolecular pump (Pfeiffer TPU-500). The analyzer is connected with the main chamber through a 0.18 cm diameter aperture for passage by the electrons and is pumped in two stages by a pair of liquid-nitrogen-baffled diffusion pumps (Varian VHS-4, Convalex-10 fluid) having a speed of 460 $\ell\,sec^{-1}$ each. Metal seal flanges and bakeable construction have permitted the ultimate pressure in the analyzer to reach 1.0×10^{-9} Torr. With the beam running at a typical throughput, the pressure in the analyzer increases to 3×10^{-9} Torr.

2. Photon sources.

Most of the work with this spectrometer has been carried out with rare-gas resonance lines from a DC discharge in a water-cooled 2 mm diameter x 5 cm long quartz capillary. A 2 mm diameter x 35 cm long quartz collimating capillary directs the photons toward the ionization region. Based on the loss current from a homemade copper photodiode we estimate that the maximum intensity after the collimating capillary for the He($I\alpha$) line is $\sim 10^{13}$ photons sec^{-1}. Two lamps are installed in the spectrometer to allow for a choice of angular geometries. One lamp is oriented normal to the plane of Fig. 1, so that the axis of the photon beam is orthogonal to both the molecular beam axis and to the direction of electron collection. The other lamp is oriented in a position off-normal to the plane of Fig. 1, such that the axis of the

photon beam is at an angle of 54.7° with respect to both the molecular beam axis and to the direction of electron collection. Because the linewidth of the photon source is expected to have a significant effect on the observed resolution of this spectrometer, we have followed the recommendations of Samson[15] for narrowing the linewidth by using a short discharge capillary and by minimizing the length of the cold gas column between the discharge and the differential pumping port. Even so, it is necessary to run at quite low lamp pressures and considerably reduced photon output to obtain the best possible resolution.

Recently we have also made use of a pulsed excimer laser (Lumonics TE-861)[16] operating on the ArF ($h\nu$ = 6.42 eV) and KrF ($h\nu$ = 4.98 eV) lines to perform PES via multiphoton ionization. A special problem arises in this experiment because all of the electrons produced by a given laser pulse arrive at the detector within a period of less than 1 μsec. Since the multichannel detection system requires 6 μsec to process each event (see Section III.E.), it is necessary to work under conditions such that no more than one electron per laser pulse is detected. With the laser running at a repetition rate of 40 Hz the sensitivity of the MBPES machine is sufficient to permit the acquisition of a multiphoton photoelectron spectrum in a few hours with a resolution limited by the linewidth of the laser (ca. 20 meV/photon for ArF). No electron extraction field is used in our experiment.

3. Electron energy analyzer.

The selection of a 180° hemispherical deflector for this spectrometer is indicated by the natural configuration of the hemispherical analyzer for multichannel detection and by its capability for serving as the second stage of a double monochromator. A cylindrical mirror analyzer (CMA) would have the advantage of high collection efficiency, but even with a double-pass CMA we felt that the background would be higher than in the present design. Our design also offers high angular resolution and the consequent capability for angular distribution studies.

Let us consider the factors relating to the design of an optimized hemispherical analyzer, some of which have been discussed by Kuyatt and Simpson.[17,18] We shall restrict our attention to a system which operates at constant pass energy and hence at constant resolution throughout a scan. At least one asymmetric potential lens is therefore needed, to retard or accelerate the electron beam by varying amounts while scanning. A schematic diagram of this lens arrangement is shown in Fig. 2. The "pencil" half-angle α, the electron beam diameter w, and the beam energy E, at the object and image planes of the lens are related by the law of Helmholtz and Lagrange,

$$\alpha' w' (E_k)^{1/2} = \alpha_0 w_0 (E_0)^{1/2} \qquad (2)$$

The spherical deflector has unit magnification from the entrance to the exit plane, and the first nonvanishing aberration term is given by $-2\alpha_0^2$. The energy resolution (FWHM) is

$$\Delta E_0/E_0 = w_0/2R_0 \tag{3}$$

if aberrations are neglected. Kuyatt and Simpson[17] chose the criterion

$$\alpha_0 \leq (w_0/4R_0)^{1/2} = (\Delta E_0/2E_0)^{1/2} \tag{4}$$

to reduce tailing of the lineshape, and we adopt this requirement also. A limitation is thereby placed on the maximum solid angle of acceptance if Eq. (4) is to hold at all kinetic energies. According to Eq. (2), α_0 reaches its maximum value at the maximum kinetic energy, E_k^{max}. So from Eqs. (2) and (4) (using the equality) we have

$$\alpha_0 = \alpha'(w'/w_0)(E_k^{max}/E_0)^{1/2} = (\Delta E_0/2E_0)^{1/2} \tag{5}$$

$$\alpha' = (w_0/w')(\Delta E_0/2E_0)^{1/2}(E_0/E_k^{max})^{1/2} \tag{6}$$

For a source volume of diameter 2r, we can use Eqs. (6) and (3) to obtain an expression for Ω, the maximum solid angle of acceptance.

$$\Omega = (\pi/4)(w'^2/z^2)$$

$$= (\pi/4)(w'^2\alpha'^2/r^2)$$

$$= (\pi/4)(w_0^2/r^2)(\Delta E_0/2E_0)(E_0/E_k^{max}) \tag{7}$$

$$= (\pi/2)(R_0/r)^2(\Delta E_0/E_0)^3(E_0/E_k^{max})$$

For an analyzer with multichannel detection, the size of the energy window ΔE_D for a detector of width w_D is

$$\Delta E_D = E_0 w_D/2R_0 \tag{8}$$

We now wish to calculate the detection rate for an analyzer which meets the pencil angle requirement of Eq. (4). The ionization rate for producing electrons with kinetic energy E_k is

$$\begin{aligned} N(E_k) &= I\ \sigma(E_k)\ n\ V \\ &\sim I\ \sigma(E_k)\ n\ r^3 \end{aligned} \tag{9}$$

where I is the photon intensity, $\sigma(E_k)$ is the ionization cross section for producing electrons with energy E_k, n is the number density of molecules, and V is the ionization volume. The detection rate C is given by the expression

$$C \sim N(E_k)\ \Delta E_D\ \Omega \tag{10}$$

Using Eqs. (7)-(10) we arrive at the result

$$C \sim (I\sigma(E_k)nR_o r w_D \Delta E_o^3)/(E_o E_k^{max}) \qquad (11)$$

Thus to achieve the maximum sensi. ty for a given ΔE_o, we should maximize R_o, r, and w_D, and minimize E_o. The practical lower limit to E_o is imposed by non-ideal effects (i.e., stray fields, charging, etc.), and we have chosen the minimum value of 0.5 eV with this in mind. The limiting maximum value of R_o is determined by the residual magnetic field in a carefully shielded chamber which we estimate to be 0.001 gauss. Roy and Carette[19] have given an expression relating the residual magnetic field H (gauss) to the energy E_o(eV), the path length ℓ (cm), and the maximum beam deviation d(cm),

$$H = 6.74\ E_o^{1/2}\ d/\ell^2 \qquad (12)$$

To maintain a value of d less than the slit diameter in the type of spectrometer proposed here, a maximum value of $R_o \approx 10$ cm is indicated. The detector width w_D is selected to be 3.81 cm for compatibility with 4.0 cm diameter microchannel plates (Varian 8908A). The mean radius R_o is 10.16 cm, and the gap between the hemispheres is 5.08 cm. A large gap is desirable because it avoids the problem of overfilling the analyzer; that is, the maximum deviation of the electron beam passing too close to the hemispheres. In our design the filling factor is always less than 80%, but the large gap necessitates

the use of field termination electrodes (FTE's) to correct for fringing fields. Numerical solutions of Laplace's equation were generated for a variety of FTE configurations, and the equipotential plot for the final design is shown in Fig. 3. The FTE's are a series of concentric, equally-spaced rings in the equatorial plane of the hemispheres with voltages proportional to R^{-1}, thereby simulating R^{-1} variation in the potential across the gap. This gives excellent field termination in the region plotted in Fig. 3. In the critical regions near the entrance slit and the detector, however, the residual fringing field is worse, because it is necessary to cut away the FTE's for a distance of 1-2 cm to avoid blocking the electron beam.

The 90° spherical sector is chosen as the pre-analyzer because of its convenient geometry and because its properties are well understood. The pre-analyzer imposes a triangular slit function (neglecting aberrations) on the electron beam going into the hemispherical analyzer, and we choose the FWHM of this slit function to just fill the energy window presented by the multichannel detector. The resolution (FWHM) of the pre-analyzer is given by

$$\Delta E_1/E_1 = w_1/2R_1 \tag{13}$$

where E_1, w_1, and R_1 are the pass energy, the slit diameter, and the mean radius, respectively, of the pre-analyzer. By using Eqs. (8) and (13) along with the requirement

$$\Delta E_D = \Delta E_1 \tag{14}$$

we obtain the expression

$$w_1 = w_D(R_1/R_o)(E_o/E_1) \tag{15}$$

The value of $E_o/E_1 = 1/8$ is selected in order to reduce the effect of stray fields by keeping the electron beam at higher energy prior to entering the hemispherical analyzer. Thus the lens which transports the electron beam between the analyzers also decelerates it by a factor of 8. A virtual slit is used at the entrance to the hemispherical analyzer, so the spectrometer resolution is critically dependent on the focusing properties of the 8:1 decelerator. For a given value of $\Delta E_o/E_o$, the diameter of the virtual slit, w_o, is determined by Eq. (3). The value for w_1 then follows from Eq. (15), and the magnification of the 8:1 decelerator is $M_{01} = - w_o/w_1$. A three-element cylinder-lens possessing the desired properties was designed using the focal length data of Harting and Read.[20] The two degrees of freedom of the three-element lens are exhausted by the requirements of positioning the image and decelerating the beam, so the magnification M_{01} (and hence the resolution $\Delta E_o/E_o$) can be varied only by fabricating a different three-element lens. This job is considerably more difficult than for a conventional analyzer where $\Delta E_o/E_o$ can be varied by merely changing the slit. Should one wish to improve the resolution by reducing M_{01}, the solid angle of acceptance Ω will, according to Eq. (7), have to be

decreased as the third power of $\Delta E_0/E_0$ if the pencil angle criterion of Eq. (4) is to be maintained. The pre-analyzer has a mean radius of $R_1 = 3.81$ cm and a gap of 1.27 cm, which is sufficient to keep the filling factor less than 80% for all operating conditions. Herzog field correction electrodes[21] are placed at the entrance and exit planes of the 90° deflector. The pre- analyzer has virtual entrance and real exit apertures with diameters $w_1 = 0.179$ cm determined by Eq. (15). The resolution of the hemispherical analyzer is chosen to be $\Delta E_0/E_0 = 0.0077$, so that the entrance slit size is $w_0 = 0.156$ cm, and the magnification of the 8:1 decelerator is $M_{01} = -0.870$.

The analyzers, lenses, and detector are fabricated from bakeable, nonpermeable materials consisting primarily of aluminum, molybdenum, copper, and ceramic, but almost no stainless steel. Aluminum screws were used throughout to assemble the optical elements. Molybdenum and gold-plated OFHC copper have become popular materials for low energy electron optical elements,[19,22,23] but for the large number of components in this spectrometer, the cost and complexity of machining would have been prohibitive for either. The solution we have adopted is to construct all elements from aluminum and to apply a uniform coating of molybdenum (~1500Å thick) by vapor deposition. The performance of the spectrometer, especially at low pass energies, indicates that this is a satisfactory method of surface preparation for electron optics. The background of scattered electrons is reduced so effectively by the double analyzer that the use of a graphite coating on the deflector surfaces is unnecessary. The hemispheres (R_{inner} = 7.62 cm, R_{outer} = 12.70 cm) were machined on a numerical control

lathe[24] to an accuracy of ±5 μm. Two continuous layers of mumetal magnetic shielding material surround the ionization region and electron flight path, and a third innermost layer surrounds the hemispherical analyzer where the electron beam energy reaches its lowest value.

4. Electron lenses.

The kinetic energy scan and pass energy selection are performed by a set of lenses which transports the electron beam from the ionization region to the pre-analyzer entrance slit. The goals were set of being able to vary the pass energy by up to a factor of 16 while scanning from 0.2 eV to 30 eV kinetic energy. Electrostatic lenses tend to be strong focusing and perform poorly for acceleration or deceleration by more than a factor of 10, so a single-stage lens would be inadequate to meet these goals.[17] The design adopted here, as illustrated in Fig. 4, consists of two asymmetric potential, 3-element cylinder-lenses in series, with a field lens at the intermediate image. We reference the energy of the electron beam in the customary way by taking ground potential to be at the kinetic energy of analysis, and by referencing all voltage supplies to a supply set at $-V_k$ with respect to ground. The first stage lens, made up of the elements V_k, V_5, and V_2, has a voltage ratio, V_2:V_k, which is determined on the basis of the pass energy V_1 and which remains constant during the kinetic energy scan. The second stage lens made up of V_2, V_3, and V_1 performs the actual scan by varying the voltage ratio V1:V2 in a manner which is the same for all pass energies. The behavior of these voltage ratios is

listed in Table I. This two-stage approach affords access to a wide range of overall voltage ratios without the need for excessive acceleration or deceleration at a given lens. The design of each of the stages is based on the theoretical focal length data for 3-element asymmetric cylinder-lenses compiled by Harting and Read.[20] For a number of configurations we have calculated the "zoom lens" curves which relate the focusing voltages, V_3 and V_5, to the voltage ratios for their respective lenses. To maintain constant transmission we desire that the magnification of each lens have a constant value of M=-1.00 during the scan, but in principle M must vary, because a three-element lens has only two degrees of freedom. It was possible however to select optimized configurations such that the magnification varies only between -0.94 and -1.06 throughout the proposed range of voltage ratios. A field lens, made up of V_2, V_4, and V_2 is included at the intermediate image for beam angle correction[17] and is used to improve the count rate at the lowest pass energies and also to correct the effect of misalignment of the photon beam. A set of deflectors located at the pre-analyzer entrance slit is seldom used.

Because the lenses have unit magnification we have the result $w' = w_1$, where w' is the diameter of the first defining aperture (see Fig. 2), and w_1 is the pre-analyzer slit diameter. For a given choice of E_0 and E_k^{max}, the allowed solid angle, Ω, can be calculated from Eq. (7). With this result the distance, z, from the ionization region to the first aperture is determined by

$$z = w_1(\pi/4\Omega)^{1/2} \tag{16}$$

Typical values are $z = 2.9$ cm, $w_1 = 0.179$ cm, and $\Omega/4\pi = 2.3 \times 10^{-4}$, which corresponds to an angular acceptance of $\pm 1.8°$ for a point source of electrons. Due to the predominant spherical aberration in electrostatic lenses, the recommended maximum filling factor for good performance is 50%.[17] The limitation we have placed on the pencil angle in the hemispherical analyzer, as expressed through Eq. (7), is sufficient under most conditions to keep the lenses less than 50% filled. The portion of the beam that makes larger excursions off the central axis will tend to be stopped by the pre-analyzer, so overfilling of the first lenses is in any event not a serious problem.

The spectrometer has the convenient property that all voltages are in principle either constant during a scan or are linear functions of the kinetic energy, with the sole exception of V_3, the focusing voltage of the kinetic energy scan lens. The voltages are provided by a system of highly stabilized voltage-programmable power supplies (Kepco PCX and Kepco ABC). For scanning over a small range (<2 eV width) we have found it adequate to drive V_3 linearly with kinetic energy. For wider scans V_3 is programmed by a digital-to-analog converter to follow a polynomial function that is a best fit to the empirically determined zoom lens curve, an example of which is shown in Fig. 5. In this way the transmission of the lenses can be maintained at a nearly constant value for scans where the kinetic energy varies by a factor of 10 or more. The transmission will be considered again in Chapter III.

5. Detection system.

Although the capability of multichannel detection to provide increased sensitivity is well known in ESCA,[26] the use of such a system in lower energy electron spectroscopy is a comparatively recent development.[27-31] We have chosen a multichannel detection system based on position-encoding by the charge division method.[32] An assembly drawing of the detector is shown in Fig. 6. The electron beam is dispersed in energy across a 4.0 cm diameter dual microchannel plate electron multiplier. Each incoming electron is amplified a factor of 10^6 and accelerated to a resistive anode consisting of a carbon film on an Al_2O_3 substrate with an aluminum contact strip at either end of the resistor. The position of the charge centroid is proportional to X1/(X1 + X2), where X1 and X2 are the quantities of charge flowing out the ends of the resistor. A schematic diagram of the position-encoding circuitry is shown in Fig. 7. Signals from the resistive anode are capacitively decoupled from high voltage and fed to a pair of charge-sensitive pre-amplifiers (LeCroy TRA510). Next follow pulse-shaping amplifiers consisting of a single stage of differentiation with pole-zero cancellation and three stages of integration, resulting in quasi-Gaussian output pulses.[33] The quantity X1 + X2 is formed at an analog summing junction, and the position, X1/(X1 + X2), is calculated by successive approximation as an 8-bit digital word. For each valid count the corresponding channel of a 256-word, 14-bit buffer memory is incremented, and is read out by a microcomputer after a specified accumulation time. The time required for the position-encoding system

to process an event is 6 μsec, which permits a maximum random count rate of 10-15 kHz. The resistive anode has an active area of 3.81 cm x 1.11 cm and is spaced 0.20 cm from the back face of the microchannel plate, giving a calculated distributed capacitance of 2 pF. With a strip resistance of 120 kΩ, the calculated RC time constant of the anode is then 240 ns, but in practice the anode time constant is likely to be up to a factor of two larger than this due to additional stray capacitance. The integrating-differentiating time constant of the shaping amplifiers is selected to be 500 ns, which provides a good match to the actual anode time constant. Provisions exist for the use of a double sided resistive anode for two-dimensional imaging, but we have found that the positional linearity is slightly better for the single sided anode. The electron beam in the analyzer is sufficiently well defined that position-encoding in the perpendicular dimension is not needed.

The detector was tested extensively in a small ultrahigh vacuum chamber outfitted with an electron gun. The positional resolution and linearity were evaluated by directing an electron beam at a mask perforated with a uniform grid of pinholes, which was placed over the detector. Resolution and linearity were measured to be better than 1% except for very close to the edges where they were about 2%. These tests give us the assurance that any problems with positional nonlinearity observed in the analyzer must be due not to the detector itself but rather to field-fringing. In order to shield the electron beam in the analyzer from the accelerating voltage on the front of the

microchannel plate, a 70 line-per-inch electroformed copper mesh (90% transmitting) is placed across the top of the detector. Even so, we have found it necessary to reduce the accelerating voltage between the mesh and the microchannel plate to a very low level, or significant distortion of the deflecting field results. Typically the electrons strike the front surface of the multiplier with a nominal impact energy of only 5 eV, and the detection efficiency is reduced by 10% from the value when the impact energy is 100 eV.

6. Data acquisition.

The spectrometer is controlled by a dedicated microcomputer (DEC LSI-11/2) which performs the tasks of data acquisition and storage. The most basic operations for data collection are the control of accumulation by the 256-channel buffer memory and the transfer of a frame of data from the buffer to the computer memory. These functions are carried out via a 16-line parallel I/O module. Other modules are provided for timing, for digital-to-analog conversion, and for interfaces to scalers and to a digital voltmeter. Peripheral devices include a graphic terminal, a line printer, a plotter, a display scope, and a floppy disk unit.

Two modes of data collection are used. In the so-called "normal" mode the kinetic energy is not swept, and the output consists of that portion of the spectrum which falls within a single energy window on the detector. In the "dithering" mode the kinetic energy is swept, and the frame of data from the buffer memory is advanced one channel

after each accumulation period before it is added into the spectral array. In this way electrons of every energy are counted for an equal length of time in each of the 256 channels of the buffer, thereby eliminating the effect of non-uniform sensitivity (the "signature") across the energy window. The kinetic energy step size is not arbitrary, but must be an integral multiple of $\Delta E_D/256$, where ΔE_D is the width of the energy window.[34] If this requirement were not met, a loss in resolution would result as the channels from the spectral array and the buffer array worked their way out of phase.

D. PERFORMANCE

A photographic record of the spectrometer and some of its principal components is given in Figs. 8-14. The He(I) spectrum of N_2 taken with a resolution of 10 meV FWHM (for Ar) is shown in Fig. 15. This spectrum and those reported below are all taken in the 90° geometry; i.e., the photon beam is orthogonal to the electron trajectory. The theoretical resolution at this pass energy (1.0 eV) is 7.7 meV, and the FWHM of the peaks corresponding to the N_2^+ Σ-states is 12 meV. The most striking features of this spectrum are the extremely low background and the high resolution which are characteristic of this apparatus. The signal-to-background ratio is 300:1 in the vicinity of the $X^2\Sigma_g^+(v' = 0)$ peak and is 250:1 near the $B^2\Sigma_u^+$ $(v' = 0)$ peak. For the higher kinetic energy region the background is due entirely to N_2^+ photoelectrons scattered from the surfaces of the hemispheres, whereas at lower kinetic energy there is an additional background component due

to photoemission from wall of the main vacuum chamber. The majority of the latter component is removed by allowing the photon beam to strike a simple windowless photodiode which serves as a trap for low energy electrons. In later experiments this problem was entirely eliminated by cutting a hole in the mumetal shields to allow the photon beam to exit. The total dark count rate of the multichannel detector is 10 sec^{-1}, which adds a negligible contribution to the spectral background. The molecular beam is produced by expanding N_2 at 298 K and 600 Torr through a 0.070 mm diameter nozzle. The spectrum shown here was taken in a single scan which lasted four hours. We generally do not accumulate data with multiple scans, because small energy scale drifts between scans can degrade the resolution. When running low signal experiments we prefer to accumulate a set of single scans and add them together afterwards. The FWHM of the $A^2\Pi_u$ vibrational states is 20 meV as a consequence of the 9.3 meV spin-orbit splitting which can almost be resolved in this spectrum.

The He(I) spectrum of CO shown in Figs. 16 and 17 was taken under conditions identical to those used for N_2. In this case the scan lasted six hours. The $A^2\Pi$ state spin-orbit splitting of 14.6 meV can be clearly resolved thanks to the rotational cooling. The spectrum contains a number of unlabeled features which arise from the He($I\beta$, $I\gamma$,...) photon energies and from a nitrogen impurity.

The analyzer was operated for several months in a single channel mode (using a real exit slit and a Spiraltron multiplier) before installing the multichannel detector in order to assess the relative

advantages of the two systems. The primary benefit of multichannel operation is the enhancement of the data collection rate by a factor of 12 over the equivalent single channel system. This is reasonably close to the predicted enhancement factor of 16, which is obtained from the ratio of the detector widths, taking into account the pre-analyzer slit function. As anticipated, the background is somewhat higher with multichannel detection, but the double analyzer system keeps it at a very low level nevertheless. The limitation of the multichannel count rate to a maximum of 10-15 kHz poses a problem for experiments where a weak signal of interest lies near a very strong peak (e.g., a dimer signal in the presence of an intense monomer peak). To avoid saturating the counting electronics, the rate must be kept below 10 kHz and the counting time consequently must be lengthened. In single channel operation, however, the count rate could conceivably be as high as 100-200 kHz, above which the Spiraltron would suffer a gain loss.

The best resolution we have attained is 6.5 meV FWHM in the He(I) spectrum of Ar as shown in Fig. 18. This spectrum was taken using single channel detection, a pass energy of 0.5 eV, and the lowest possible pressure in the lamp (ca. 0.1 Torr). The theoretical resolution at 0.5 eV pass energy is 3.9 meV. Although at 1.0 eV and higher pass energies the resolution has been comparable for single channel and multichannel detection, at 0.5 eV pass energy the single channel resolution proved to be better. We attribute this discrepancy to the effects of residual stray magnetic fields and to fringing of the

deflecting field above the multichannel detector. Stray fields are expected to be a more serious problem for the multichannel case because of the need to keep the electron beam tracking correctly across the entire active area of the detector.

As an example of the capability of this instrument to perform molecular PES at a new level of detail, we present in Fig. 19 a portion of the He(I) spectrum of ethylene, C_2H_4, which was taken using single channel detection, a pass energy of 1.0 eV, and an instrumental resolution of 11 meV FWHM as measured for Ar (theoretical FWHM = 7.7 meV). The gas was expanded from a stagnation pressure of 600 Torr at 298 K. Because the molecules being ionized are rotationally cold, the individual vibrational members of this band can be observed at nearly instrumental resolution, and much of the vibrational structure is fully resolved here for the first time. The principal vibrational excitation of the $^2B_{3u}$ $C_2H_4^+$ ion is in the symmetric C-C stretching mode, ν_2, which appears as a progression extending out at least to $v(\nu_2) = 5$. Each member of this progression is doubled by a concurrent excitation of two quanta in the torsional mode, ν_4. A second progression involving the additional excitation of one quantum in the symmetric H-C-H bending mode, ν_3, mirrors the first progression. The spectrum contains additional peaks indicating the excitation of one or two other modes of vibration.

REFERENCES

* This chapter (LBL-11250) was published in Rev. Sci. Instrum., 52, 1837 (1981).

1. W.P. Lapatovich, R. Ahmad-Bitar, P.E. Moskowitz, I. Renhorn, R.A. Gottscho, and D.E. Pritchard, J. Chem. Phys., 73, 5419 (1980).
2. C.D. Caldwell, F. Engelke, and H. Hage, Chem. Phys., 54, 21 (1980).
3. S.M. Beck, J.B. Hopkins, D.E. Powers, and R.E. Smalley, J. Chem. Phys., 74, 43 (1981).
4. K.E. Johnson, W. Sharfin, and D.H. Levy, J. Chem. Phys., 74, 163 (1981).
5. J.H. Glownia, S.J. Riley, S.D. Colson, and G.C. Niemann, J. Chem. Phys., 73, 4296 (1980).
6. K. Aron, C. Otis, R.E. Demaray, and P. Johnson, J. Chem. Phys., 73, 4167 (1980).
7. Y. Ono, S.H. Lin, H.F. Prest, C.Y. Ng, and E. Miescher, J. Chem. Phys., 73, 4855 (1980).
8. S.L. Anderson, T. Hirooka, P.W. Tiedemann, B.H. Mahan, and Y.T. Lee, J. Chem. Phys., 73, 4779 (1980).
9. P.M. Dehmer and J.L. Dehmer, J. Chem. Phys., 68, 3462 (1978).
10. P.M Dehmer and J.L. Dehmer, J. Chem. Phys., 69, 125 (1978).
11. F. Carnovale, M.K. Livett, and J.B. Peel, J. Chem. Phys., 71, 255 (1979).
12. P.M. Dehmer and J.L. Dehmer, J. Chem. Phys. 70, 4574 (1979).
13. P.M. Dehmer, J.L. Dehmer, and W.A. Chupka, J. Chem. Phys., 73, 126 (1980).

14. L. Asbrink and J.W. Rabalais, Chem. Phys. Lett., 12, 182 (1971).

15. J.A.R. Samson, Rev. Sci. Instrum., 40, 1174 (1969)

16. On loan from the San Francisco Laser Center.

17. C.E. Kuyatt, Electron Optics Lectures, (unpublished).

18. C.E. Kuyatt and J.A. Simpson, Rev. Sci. Instrum., 38, 103 (1967).

19. D. Roy and J.D. Carette, "Design of Electron Spectrometers for Surface Analysis", H. Ibach, ed., Top. Cur. Phys. 4, 13 (1977).

20. E. Harting and F.H. Read, "Electrostatic Lenses", Elsevier, Amsterdam (1976).

21. H. Wollnik, "Electrostatic Prisms", A. Septier, ed., "Focusing of Charged Particles", Academic, New York (1967).

22. J.H.D. Eland, J. Phys. E., 11, 969 (1978).

23. M.W. Siegel, R.J. Celotta, J.L. Hall, J. Levine, and R.A. Bennett, Phys. Rev. A, 6, 607 (1972).

24. Lawrence Livermore National Laboratory, Livermore, CA.

25. J.L. Gardner and J.A.R. Samson, J. Electron Spectros. 8, 469 (1976).

26. U. Gelius, E. Basilier, S. Svensson, T. Bergmark, and K. Siegbahn, J. Electron Spectros., 2, 405 (1974).

27. L. Karlsson, L. Mattsson, R. Jadrny, R.G. Albridge, S. Pinchas, T. Bergmark, and K. Siegbahn, J. Chem. Phys., 62, 4745 (1975).

28. M.G. White, R.A. Rosenberg, G. Gabor, E.D. Poliakoff, G. Thornton, S.H. Southworth, and D.A. Shirley, Rev. Sci. Instrum., 50, 1268 (1979).

29. S.D. Kevan and D.A. Shirley, Phys. Rev., 22, 542 (1980).

30. P.J. Hicks, S. Daviel, B. Wallbank, and J. Comer, J. Phys. E, 13, 713 (1980).

31. D.E. Eastman, J.J. Donelon, N.C. Hien, and F.J. Himpsel, Nucl. Instrum. Meth., 172, 327 (1980).

32. J.L. Alberi and V. Radalsa, IEEE Trans. Nucl. Sci., NS-23, 251 (1976).

33. F.S. Goulding and D.A. Landis, "Semiconductor Detector Spectrometer Electronics", in Nuclear Spectroscopy and Reactions, Part A, Academic Press, New York (1974).

34. S.D. Kevan, Ph.D. Thesis, University of California, Berkeley (1980).

TABLE I. Voltage ratios for the pass energy selector lens (V_k,V_5,V_2) and the kinetic energy scan lens (V_2,V_3,V_1)

Pass energy selector		Kinetic energy scan	
Pass energy, V_1 (eV)	Voltage ratio, V_2:V_k	Kinetic energy, V_k (eV)	Voltage ratio, V_1:V_2
		0.5	16:1
4	1:2		
		1	8:1
8	1:1		
		2	4:1
16	2:1		
		4	2:1
32	4:1		
		8	1:1
64	8:1		
		16	1:2
		32	1:4

FIGURE CAPTIONS

Figure 1. Schematic top view of the apparatus: (1) beam source, (2) beam catcher; (3) pass energy selector lens, (4) field lens, (5) kinetic energy scan lens, (6) deflectors, (7) 90° spherical sector pre-analyzer, (8) conductance barrier, (9) 8:1 decelerator lens, (10) hemispherical analyzer, (11) multichannel detector, (12) ion extraction lenses, (13) quadrupole mass filter, (14) differential pumping. The photon sources are located above the plane of the drawing. Not shown are two layers of mumetal surrounding the electron flight path.

Figure 2. (a) Schematic diagram of the ionization region and entrance aperture. The source diameter is 2r, the aperture diameter is w', and the distance between them is z. The pencil half-angle is α', and the beam half-angle is θ.

(b) Schematic diagram of a hemispherical deflector with a virtual slit and retarding lens. The pencil half-angle, the beam diameter, and the beam energy are given by α', w', and E_k at the first aperture, and by α_0, w_0, and E_0 at the deflector entrance plane.

Figure 3. Equipotential plot for the hemispherical analyzer entrance region. V_{in}, V_{out}, and V_0 are the inner sphere voltage, the outer sphere voltage, and the mid-sphere voltage, respectively. The field termination electrodes are six concentric, equally spaced rings lying in the

entrance plane. Their voltages correspond to the nominal 1/R-values of the potential.

Figure 4. Electron lens system consisting of two asymmetric, three-element cylinder-lenses in series. The pass energy selector lens (V_k, V_5, V_2) has a voltage ratio, V_2:V_k, determined on the basis of the pre-analyzer pass energy, V_1. The kinetic energy scan lens (V_2, V_3, V_1) has a voltage ratio, V_1:V_2, which is swept during the scan. A field lens (V_2, V_4, V_2) at the intermediate image allows for beam angle adjustment. A set of deflectors, D, is located at the pre-analyzer entrance.

Figure 5. Focusing voltage, V_3, as a function of kinetic energy, V_k, for a pre-analyzer pass energy of E_1 = 16 eV. The points are determined by optimizing the signal for some 25 molecular photoelectron transitions. The lower curve is the least-squares fit, fourth-order polynomial function used to program V_3 via a D/A converter. The upper curve is based on the theoretical lens data of Harting and Read (Ref. 20).

Figure 6. Assembly drawing of the detector.

Figure 7. Schematic of the position-encoding electronics: (Ch)-charge-sensitive pre-amplifier, (Sh)-shaping amplifer, (S/H)-sample and hold, (Pk)-peak detector, (Sm)-summing amplifier, (Th)-threshold detector, (Ov)-overload detector, (Mult D/A)-multiplying D/A converter, (Cm)-comparator,

(SAR)-successive approximation register, (Ck)-2 MHz clock, (Latch)-latched output driver.

Figure 8. View of the analyzer with the outer hemisphere removed, showing the inner hemisphere, the entrance aperture, the field termination wires, and the baseplate.

Figure 9. The inner and outer hemispheres. Note the entrance slit set-up for single channel detection.

Figure 10. View of the analyzer with the outer hemisphere in place.

Figure 11. The preanalyzer and the lens elements for the deflectors and for V_1, V_3, and V_2.

Figure 12. The analyzer chamber. Note the ports leading down to the differential pumping stacks.

Figure 13. View of the apparatus showing the beam source (at left), the analyzer (at right), and the electronics (behind). The large pipe running overhead connects the forearm of the beam source diffusion pump to the Roots blower.

Figure 14. View of the apparatus showing the beam source (at right), the main chamber (at center) with its flange for the quadrupole mass filter (not installed), and the helium inlet manifold (with operator attached). In the foreground is the test chamber for the multichannel detector.

Figure 15. He(I) spectrum of N_2 at an instrumental resolution of 10 meV FWHM. The stagnation pressure and temperature are 600 Torr and 298 K. The analyzer is operated at a pass energy of 1.0 eV with multichannel detection.

Figure 16. He(I) spectrum of CO at an instrumental resolution of 10 meV FWHM. The stagnation pressure and temperature are 600 Torr and 298 K. The analyzer is operated at a pass energy of 1.0 eV with multichannel detection.

Figure 17. A portion of the spectrum of CO shown in Figure 16.

Figure 18. He(I) spectrum of Ar at an instrumental resolution of 6.5 meV FWHM. The stagnation pressure and temperature are 1000 Torr and 298 K. The analyzer is operated at a pass energy of 0.5 eV with single channel detection.

Figure 19. He(I) spectrum of C_2H_4 at an instrumental resolution of 11 meV FWHM. The stagnation pressure and temperature are 600 Torr and 298 K. The analyzer is operated at a pass energy of 1.0 eV with single channel detection. Vibrational levels are identified by the quantum numbers of the modes ν_1, ν_2, ν_3, and ν_4.

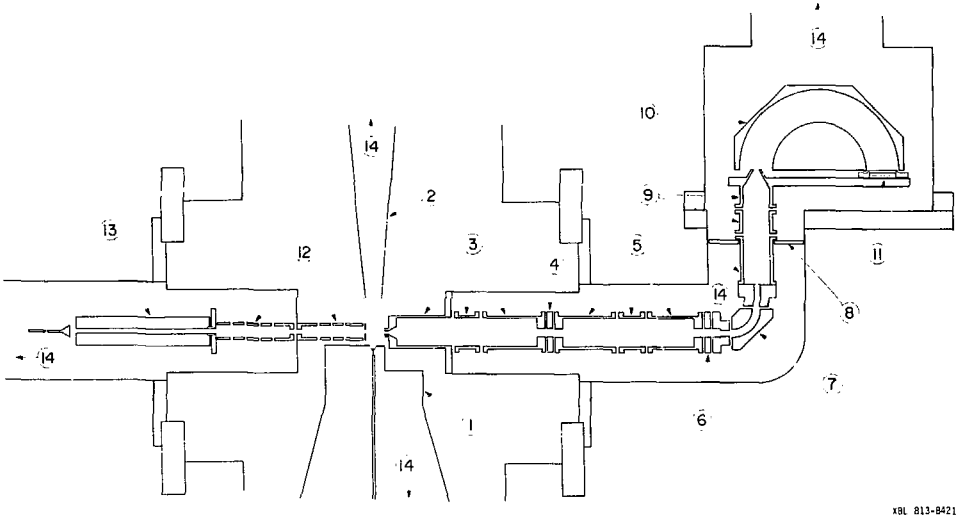

Figure 1

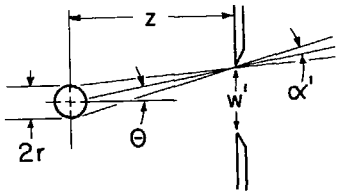

$$\alpha' = \frac{r}{z} \qquad \Theta = \frac{w'}{2z}$$

(a)

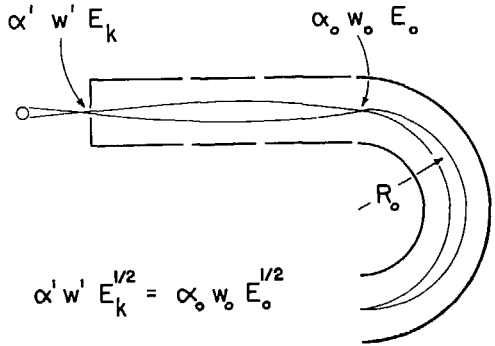

$$\alpha' w' E_k^{1/2} = \alpha_o w_o E_o^{1/2}$$

(b)

XBL 813-8419

Figure 2

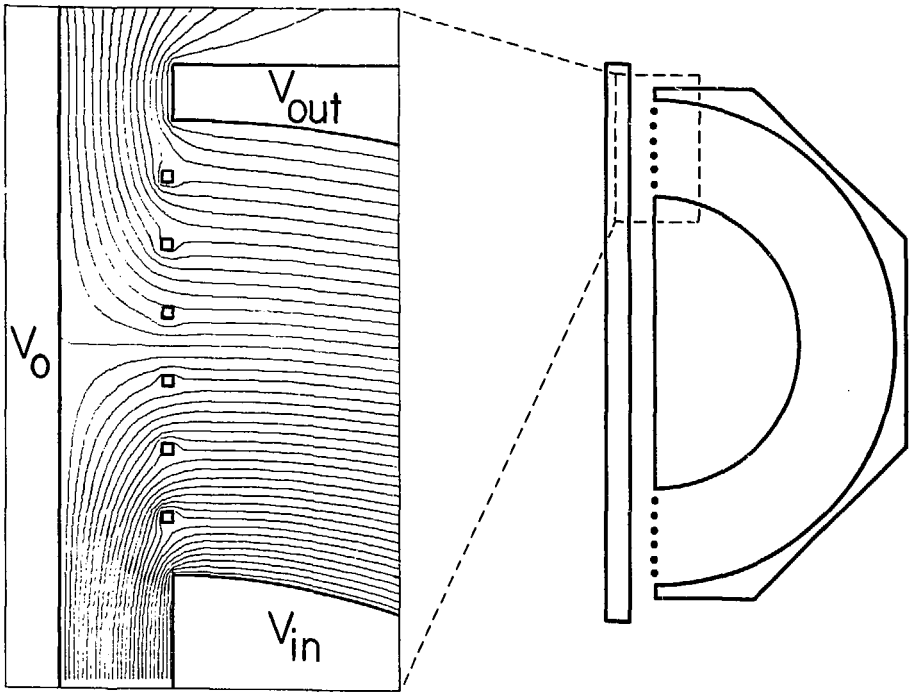

XBL 813-8423

Figure 3

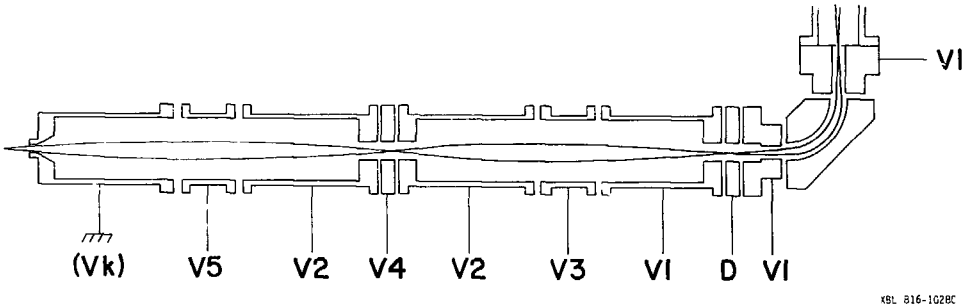

Figure 4

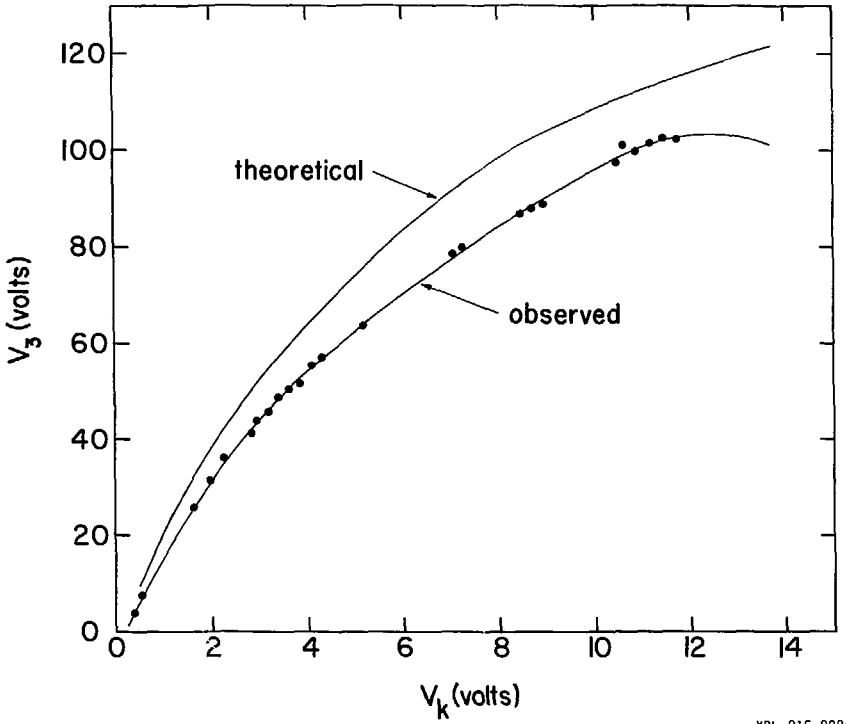

XBL 815-9984

Figure 5

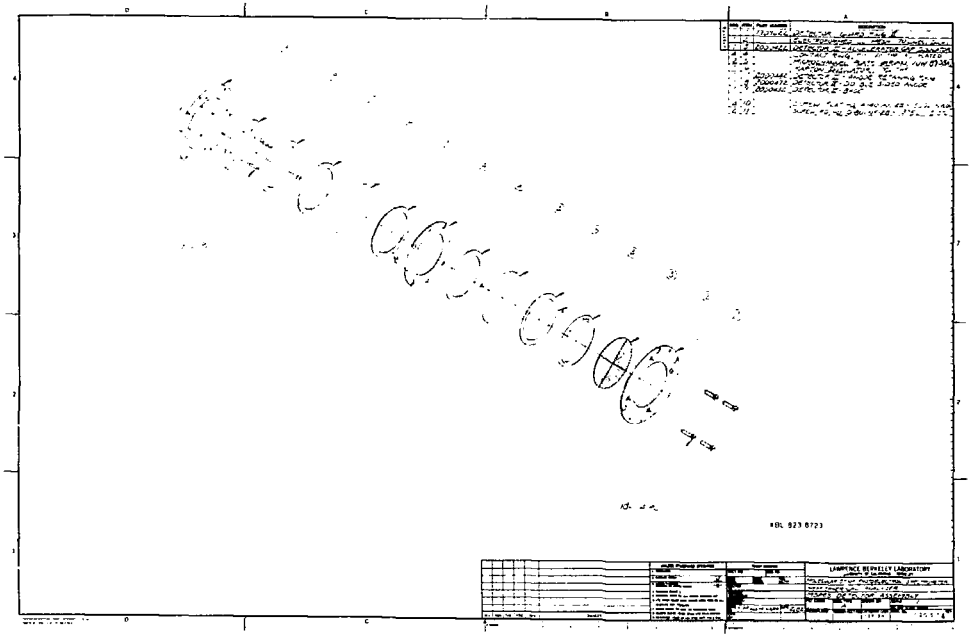

Figure 6

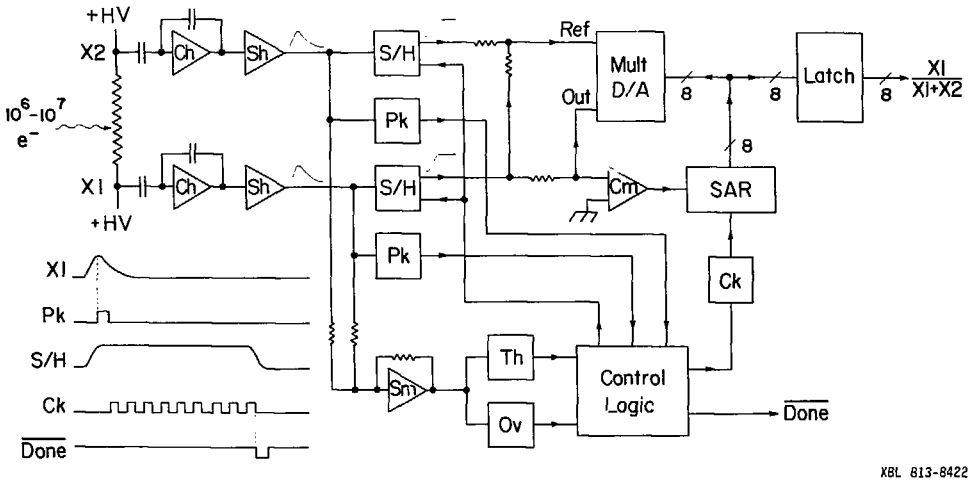
+HV
X2
Ch
Sh
S/H
Ref
Mult
D/A
Out
8
8
Latch
8
X1
X1+X2
10^6-10^7
e^-
Pk
8
X1
Ch
Sh
S/H
Cm
SAR
+HV
Pk
Ck
X1
Pk
S/H
Th
Sm
Control
Logic
Ck
Ov
Done
Done
XBL 813-8422

Figure 7

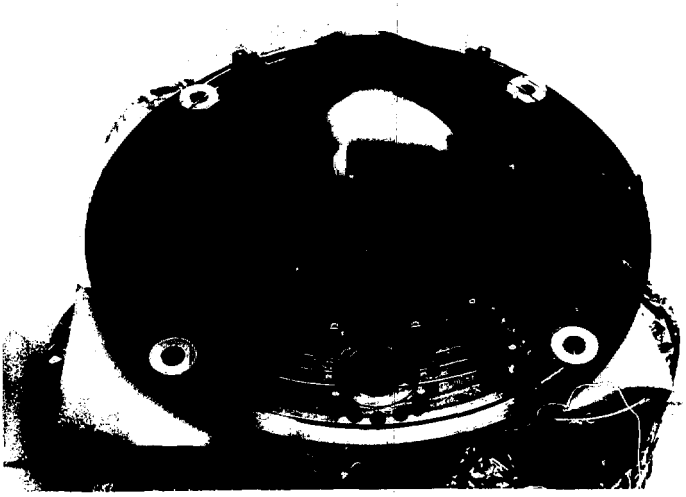

CBB 822-1296

Figure 8

CBB 822-1302

Figure 9

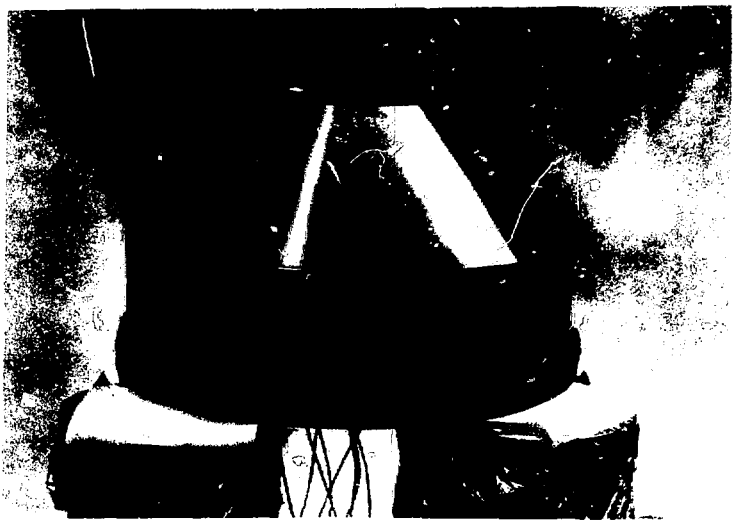

CBB 822-1304

Figure 10

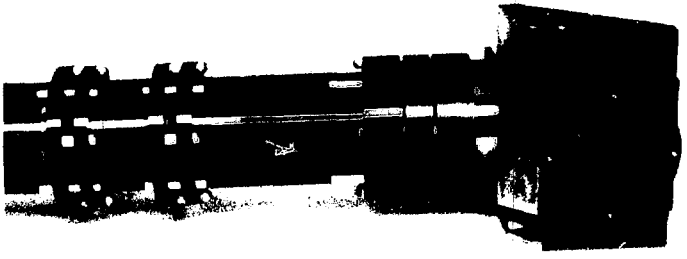

CBB 822-1308

Figure 11

CBB 822-1260

Figure 12

CBB 8010-14311

Figure 13

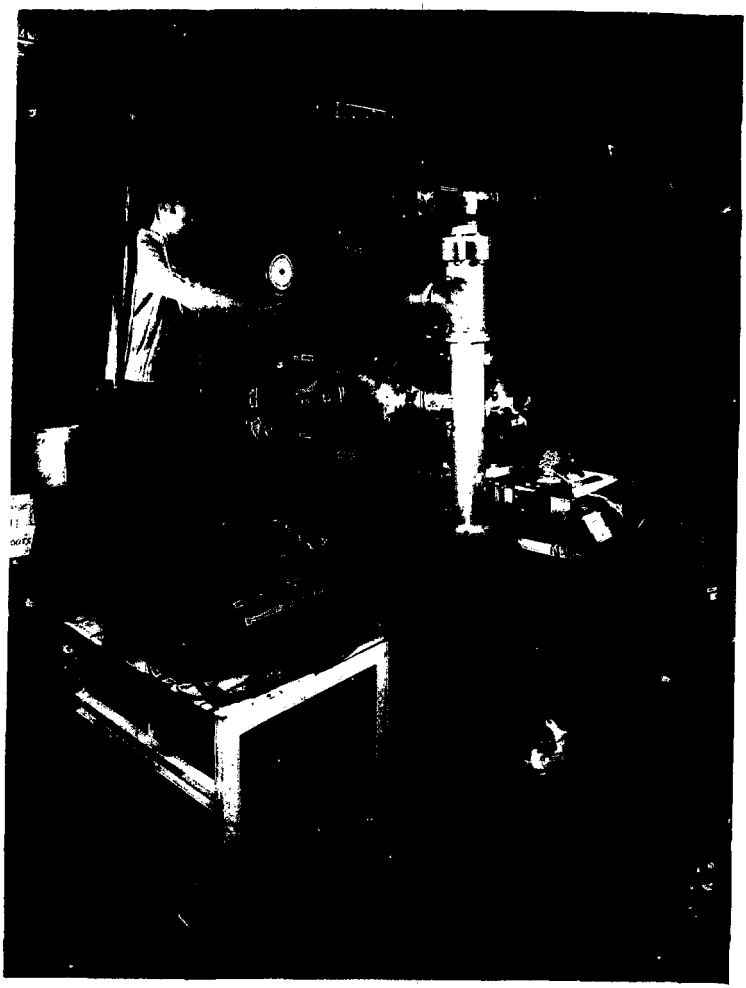

CBB 8010-14307

Figure 14

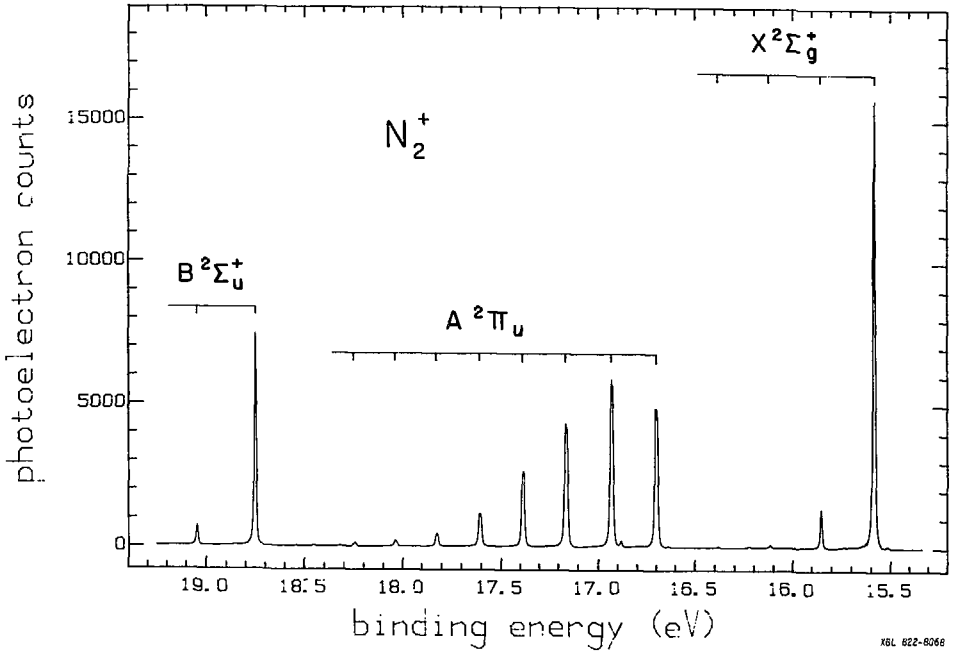
photoelectron counts
15000
10000
5000
0
N_2^+
$X\,^2\Sigma_g^+$
$B\,^2\Sigma_u^+$
$A\,^2\Pi_u$
19.0
18.5
18.0
17.5
17.0
16.5
16.0
15.5
binding energy (eV)
XBL 822-8068

Figure 15

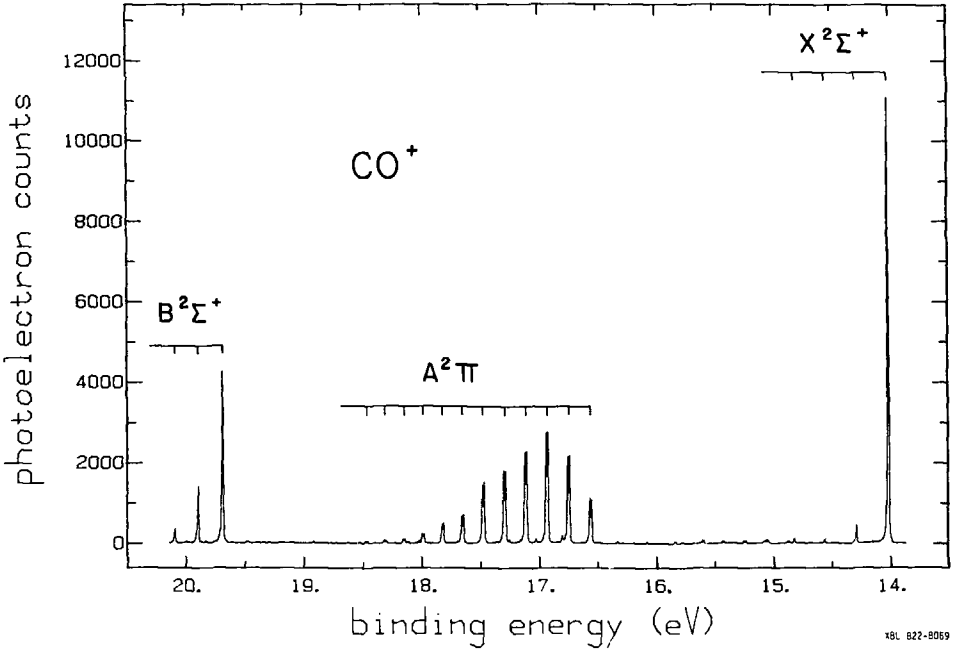
photoelectron counts
12000
10000
8000
6000
4000
2000
0
CO+
X 2Σ+
B 2Σ+
A 2Π
20.
19.
18.
17.
16.
15.
14.
binding energy (eV)
XBL 822-8069

Figure 16

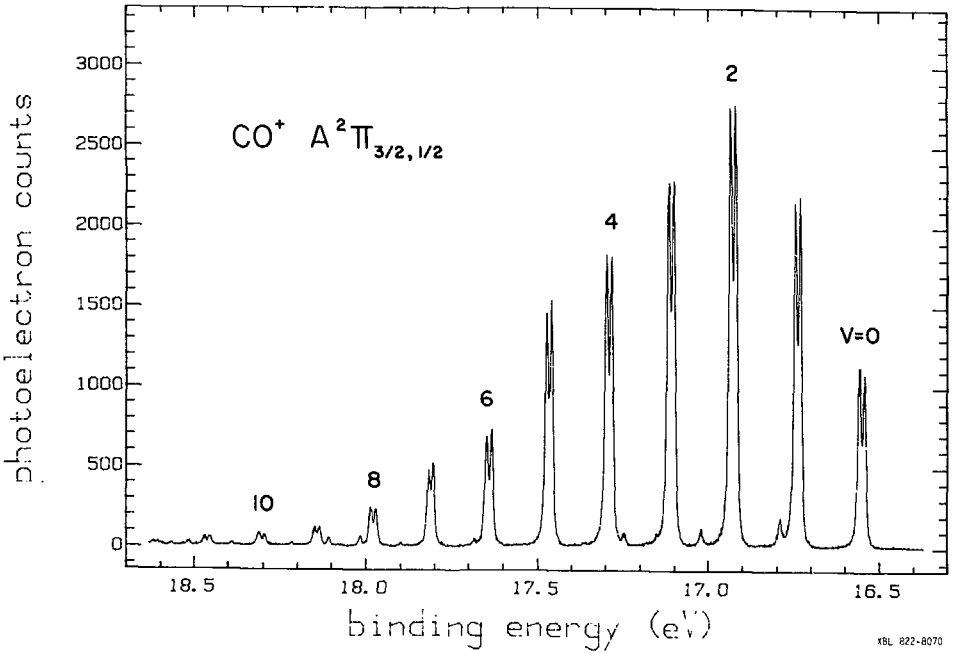
photoelectron counts
3000
2500
2000
1500
1000
500
0
CO+ A 2Π3/2,1/2
10
8
6
4
2
V=0
18.5
18.0
17.5
17.0
16.5
binding energy (eV)
XBL 822-8070

Figure 17

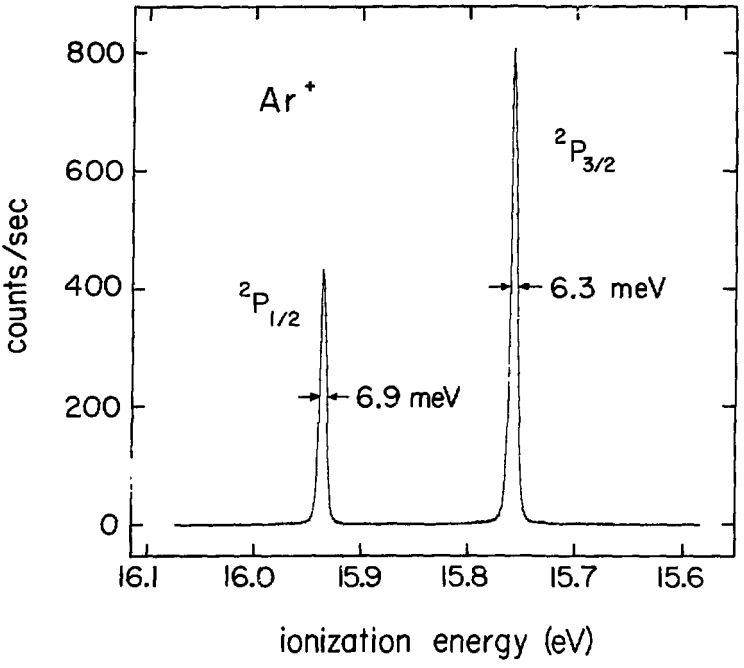

XBL 815-9985

Figure 18

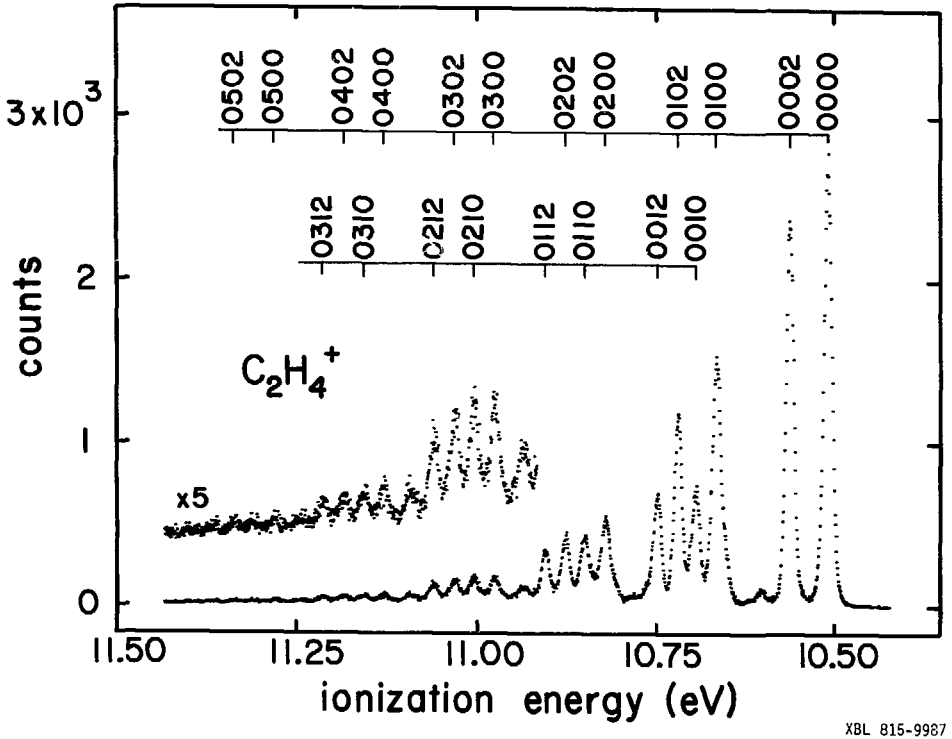

XBL 815-9987

Figure 19

III. ROTATIONALLY-RESOLVED PHOTOELECTRON SPECTROSCOPY OF $n\text{-}H_2$, $p\text{-}H_2$, HD, AND D_2*

ABSTRACT

The 584Å photoelectron spectra of $n\text{-}H_2$, $p\text{-}H_2$, HD, and D_2 were recorded at a resolution of 11 meV FWHM using a supersonic molecular beam source. Spectra were taken at several stagnation temperatures and pressures in order to vary the rotational population distribution in the beam with a corresponding variation in the relative intensities of the rotational transitions. Many of the Q branch components were resolved for the first time. $\Delta G(v+1/2)$ and B_v values were measured for all observed vibrational states of H_2^+, HD^+, and D_2^+ and were used to determine the ionic vibrational and rotational constants: ω_e, $\omega_e x_e$, $\omega_e y_e$, $\omega_e z_e$, B_e, and α_e. The results represent a substantial improvement over previous experimental determinations and were found to be consistent with the available theoretical rotation-vibration energy levels. The measurement of the intensity distribution of photoelectrons as a function of vibrational state yielded photoionization cross sections which were in good agreement with the theoretical values calculated by ONeil and Reinhardt.

A. INTRODUCTION

The photoelectron spectra of H_2, HD, and D_2 can in principle provide a determination of the spectroscopic constants of the H_2^+, HD^+, and D_2^+ molecular ions and the relative pnotoionization cross sections for transitions to the various ionic rotation-vibration energy levels. The ground state potential energy curves for H_2 and H_2^+ are shown for reference in Fig. 1. Although several measurements of the photoelectron spectra have been reported,[1-5] there still exists a need for data of higher resolution and signal-to-background ratio, particularly for the upper vibrational states which are usually obscured by the background of stray electrons. The Doppler broadening in the photoelectron spectra of these light molecules is relatively large and has limited the resolution obtained in previous experiments. The Doppler linewidth at room temperature for H_2^+ (v = 0) with 584Å (HeIα) light amounts to 20 meV, which is several times larger than the best attainable instrumental resolution. Åsbrink[1] used a spectrometer having a resolution of 4-7 meV and a Ne(I) light source (736Å, 744Å) to reduce the Doppler broadening and obtained a rotationally-resolved spectrum of H_2^+ (v = 0 to 5), but the positions of only a few of the rotational lines could be determined accurately because of the overlapping peaks from the two Ne(I) photon energies.

High quality photoelectron spectra would provide a considerable improvement in our experimental knowledge of the rotation-vibration energy levels of H_2^+, HD^+, and D_2^+. The positions of the few lowest energy levels are known from the extrapolation of Rydberg series.[6]

Conventional absorption or emission spectra from a gaseous discharge have not been observed for these ions in the visible or UV regions because all of the excited electronic states are repulsive in the vertical region of the ground state. Furthermore, the triatomic species (e.g. H_3^+) becomes the predominant molecular ion in the discharge before the number density of the diatomic ion is high enough for infrared measurements.[7] The experimental situation has improved considerably in recent years for HD^+, which, because of its dipole moment and the near coincidence of its vibrational frequency with those of certain CO and CO_2 laser transitions, can be observed in absorption by ion-beam-infrared-laser-resonance techniques.[7-9] The accuracy of these measurements is very high ($\pm$ 0.002 cm^{-1}), but only a small number of rotation-vibration transitions have been observed.

Because the hydrogen molecular ions are composed of just three particles, theory provides a much more complete description of the rotation-vibration energy levels than has been available from experiment. Extensive tabulations exist for the bound state levels calculated in the Born-Oppenheimer and adiabatic approximations.[10-12] Calculations have also been reported which include relativistic, radiative, and non-adiabatic effects for many energy levels of HD^+ [13,14] and for a few low-lying levels of the other isotopes.[15,16]

The relative intensities of transitions to the different ionic vibrational states at 584Å have been measured for H_2^+, HD^+, and D_2^+ by Berkowitz and Spohr[2] and for H_2^+ by Gardner and Samson.[4] On the theoretical side, the photoionization cross section as a function of

v-state has been calculated at various levels of sophistication by Villarejo,[17] by Itikawa,[18-21] by Lee and Rabalais,[3] by Ford, Docken, and Dalgarno,[22] and by ONeil and Reinhardt.[23]. The agreement between experiment and theory has been satisfactory in general, but a detailed comparison has awaited higher quality spectra, particularly for the upper v-states for which the limited sensitivity and unresolved rotational structure in previous experiments contribute to the uncertainty in the measured values.

We have recorded the 584Å photoelectron spectra of n-H_2, p-H_2, HD, and D_2 with an apparatus which uses a supersonic molecular beam source to remove Doppler broadening. The spectra reveal considerably more rotational structure than was observed in earlier experiments, and, because of the very low spectrometer background, transitions are observed for states up to one or two vibrational quanta from the dissociation limit. The rotational population distribution of the molecules in the beam can be varied significantly by adjusting the stagnation temperature and pressure, and this provides a useful tool for enhancing or reducing transitions from rotationally-excited states of the neutrals. We report values for the rotational and vibrational constants of H_2^+, HD^+, and D_2^+, as well as the photoionization cross sections for all observed vibrational states.

B. EXPERIMENTAL

The apparatus has received a detailed description elsewhere,[24] so its characteristics will only be outlined here. Hydrogen was

expanded through a 70-μm-diam nozzle located 6.4 mm from the tip of a 0.66-mm-diam x 6.4-mm-tall skimmer. After entering the main chamber the beam of hydrogen was crossed with the photon beam from a helium resonance lamp, and a fraction (~ 10^{-4}) of the resulting photoelectrons passed through the entrance aperture and was transported by a series of lenses to a 90° spherical sector pre-analyzer. From this point the electrons were decelerated into the main analyzer, a 10.16 cm mean radius hemispherical deflector, and were dispersed across a position-sensitive multichannel detector. The principal advantages of this analyzer design are 1) the reduction of background provided by the pre-analyzer, and 2) the enhanced collection efficiency through the use of multichannel detection. For these experiments the analyzer was operated at a constant pass energy of 1.0 eV which gave a resolution of 11 meV FWHM as observed for the Ar 3p doublet with 584Å light. All spectra were taken with the light source at the 90° geometry; that is, with the nominally unpolarized photon beam orthogonal to the electron trajectory.

Each spectrum was accumulated in a single scan of the kinetic energy lasting two to four hours. Data acquisition and storage were controlled by an LSI-11/2 microcomputer. To eliminate the nonuniformity in the response of the multichannel detector the "dithering" procedure was used, wherein each channel of the spectral array received counts from every position on the detector for an equal length of time. The scan width was determined by measuring the voltage of the power supply controlling the kinetic energy with a computer-interfaced precision digital voltmeter (Dana 5900) at four points during the scan.

The calibration of the scan width in the region of importance for hydrogen was checked by measuring the spectrum of nitrogen and determining the N_2^+ X $^2\Sigma_g^+$ (v = 0) to B $^2\Sigma_u^+$ (v = 0) splitting, which is accurately known from emission spectra (25566.0 cm^{-1} = 3.16981 eV).[25] This splitting was reproducible to within ± 0.001 eV (± 8 cm^{-1}) with this apparatus.

The n-H_2 and D_2 samples were obtained commercially, the H_2 being UHP grade (99.999%), and the D_2 being CP grade (99.5%) which nevertheless had a noticeable HD impurity that appears in some of our D_2 spectra. The p-H_2 sample was obtained by transferring a quantity of liquid p-H_2 from a hydrogen liquefier into a standard aluminum gas cylinder. The purity of the p-H_2 gas was approximately 90-95% initially, and the observed half-life for conversion to n-H_2 was 3 to 4 weeks at a pressure of 70 psig. HD was prepared[26] by the reaction of $LiAlH_4$ with D_2O, and the gas was compressed to several hundred psi and stored in an aluminum cylinder. Impurities of H_2 and D_2 amounted to about 1% each in the HD sample.

The quadrupole mass filter was not in the chamber during these experiments, but the fraction of clusters in the molecular beam was expected to be negligible. Even at a stagnation temperature of 77K the backing pressure we used (200 Torr) was an order of magnitude below that needed for significant dimerization.[27]

C. RESULTS AND DISCUSSION

1. Spectra

The 584Å spectra of n-H_2, p-H_2, HD, and D_2 expanded from about one atmosphere at room temperature (297K) are shown in Figs. 2-5 with the ionic vibrational states indicated and the Q branch (J' = J") rotational quantum numbers labeled for a typical vibrational band. The lower vibrational levels of H_2^+ also exhibit partially resolved S branches (J' = J" + 2) which are labeled as such. In most cases a separate scan with better statistics for the higher vibrational levels is also presented in the figure. Small discontinuities in the spectra at kinetic energies of 5.28 and 5.46 eV are due to Ar calibration peaks which have been subtracted out. These hydrogen spectra represent a considerable improvement over previously published results in both the resolution and the signal-to-background ratio (typically 200-300 near the strongest transitions). Even so, the Q branches are not totally resolved, and as a consequence the spectral analysis must rely heavily on deconvolution techniques, limiting the accuracy of the resulting spectroscopic constants. This limitation can be largely overcome by adjusting the nozzle temperature so as to change the rotational population distribution of the molecules in the beam. This temperature dependence is illustrated by three examples in Fig. 6. When hydrogen at 77K undergoes a supersonic expansion the molecules are left almost entirely in their lowest accessible rotational states. For p-H_2 and HD this is the J" = 0 level, but for n-H_2 there is a 1:3 mixture of J" = 0 and J" = 1, and for n-D_2 a 2:1 mixture of J" = 0 and J" = 1.

Thus the 77K spectra of p-H_2 and HD in Figs. 7 and 8 consist primarily of vibrational bands involving only the Q(0) rotationless transitions. The 77K spectrum of D_2 in Fig. 9 is similar in appearance to a rotationless spectrum despite the ~ 33% Q(1) component because the splitting between the Q(0) and Q(1) transitions is only 4-6 meV and is not resolved. The 77K spectra give us the best data on the vibrational properties of H_2^+, HD^+, and D_2^+, namely the ΔG values and photoionization cross sections. We can also produce a rotationally relaxed hydrogen beam starting from room temperature by running with a smaller nozzle at much higher backing pressure (e.g., 40-μm-diam and 100 psi), but the cooling is not as effective as with the nozzle held at 77K. On the other hand the rotationally excited transitions can be enhanced by heating the nozzle, as was done for the high temperature spectra which are shown in Figs. 10-12. These spectra allow us to determine the rotational constants with better accuracy than is possible with the room temperature spectra because the Q branch extends to higher J-states. It was not possible to generate a satisfactory spectrum of HD while heating the nozzle because the sample rapidly converted to a mixture of HD, H_2, and D_2. The spectrum of HD with transitions out to Q(5) in Fig. 11 was taken with the nozzle at room temperature and a very low backing pressure (50 Torr), for which the degree of rotational relaxation was significantly less than for the HD scan at 600 Torr backing pressure shown in Fig. 4. A number of discontinuities are evident in the 50 Torr spectrum of HD, which are due to an air impurity that has been subtracted out. A scan of p-H_2 with the heated nozzle was not attempted because the conversion to n-H_2 was expected to be rapid.

2. Energy Scale

The quantity measured in the photoelectron spectrum is the electron energy distribution in the laboratory frame, and to convert this to the kinetic energy distribution in the center-of-mass frame we must account for the recoil energy of the ion as given by conservation of momentum. This is particularly simple when the electrons are sampled perpendicular to a collimated molecular beam, because we may assume that the molecule initially has zero velocity along the detection direction. For a measured laboratory energy E_{lab}, the ionization energy E_I (equals photon energy minus kinetic energy) is given by

$$E_I = h\nu - (1 + m_e/m_+)\, E_{lab} \qquad (1)$$

where $h\nu = 17119.148\ cm^{-1}$,[28] and $1 + m_e/m_+$ has the values 1.0002722 for H_2^+, 1.0001816 for HD^+, and 1.0001362 for D_2^+. To convert the kinetic energy from electron volts to wave numbers we have used the factor $1.2398520 \times 10^{-4}\ eV/cm^{-1}$ given by Cohen and Taylor.[29] The absolute ionization energy determined in this experiment is subject to an uncertainty of about 10-20 cm^{-1} because of drift in the spectrometer offset due to changing contact potentials. However the present spectroscopic analyses rely only on relative ionization energies (peak splittings) for which the uncertainty is much less.

3. Vibrational Energy Levels

The 77K spectra of p-H_2, HD, and D_2 in Fig. 4 were used to determine the pure vibrational level energies of H_2^+, HD^+, and D_2^+.

Since all transitions originate from the v = 0 level of the neutral hydrogen molecule, the vibrational differences of the molecular ion, $\Delta G(v + 1/2) = G(v + 1) - G(v)$, are obtained directly from the successive vibrational splittings in the photoelectron spectra. The individual vibrational peaks exhibited a FWHM of 90-100 cm^{-1}, and the centers of the transitions could be located visually to an accuracy of about 5 cm^{-1} by plotting the spectrum on a expanded scale. We have been able to reduce considerably the random error inherent in the visual peak-finding process by a least-squares fitting procedure using an empirically derived lineshape function. The response function of the instrument was assumed to be represented by the 584Å spectrum of $Ar^+ \, {}^2P_{3/2}$ taken on the same occasion as a given hydrogen spectrum. The Ar^+ peak, which had a FWHM of 85-95 cm^{-1}, was both broadened by 2-3 cm^{-1} and smoothed via convolution with a 16 cm^{-1} FWHM Gaussian function in order to represent the residual Doppler-broadening in the hydrogen lineshape. The empirical lineshape was similar in appearance near its mean to a Gaussian, with the addition of a small exponential tail on the high kinetic energy side and a larger tail on the low energy side. The function was stored numerically with the area and mean as adjustable parameters and was evaluated along with the necessary partial derivatives for the least-squares procedure by a quadratic interpolation over the stored values. The fitting of the hydrogen peaks was performed interactively using a derivative least-squares fitting routine. An example of this procedure is illustrated in Fig. 13 which shows the v = 2 transition in p-H_2 at 77K with the decomposition into the four rotational components making up this peak. The o-H_2

impurity, as revealed by the Q(1) transition, contributes about 10% of the total area, and the S branch (primarily the $J' = 2 \leftarrow J'' = 0$ transition) contributes about 6%. Because of the limited resolution, it proved to be impractical to obtain a fit without constraining the relative positions of the rotational components in a given vibrational transition. These rotational splittings were calculated using the B_e and α_e values determined from the higher temperature photoelectron spectra as described in Section C.5. Thus the free parameters in the fitting of the 77K vibrational peaks were the position of the Q(0) transition, the areas of the rotational components, and the value of the background function which was assumed to be a constant. The least-squares fitting located the vibrational origins to within standard deviations of 1 cm^{-1} or better for p-H_2 and HD, and 2 cm^{-1} or better for D_2. Based on these results we have assigned a statistical uncertainty ($\pm 2\sigma$) for the measured $\Delta G(v + 1/2)$ values of $\pm$ 2 cm^{-1} for H_2^+ and HD^+, and $\pm$ 5 cm^{-1} for D_2^+. The principal source of systematic error is the drift in the kinetic energy offset during the course of the scan, and its magnitude can be gauged from the reproducibility of the N_2^+ X-B splitting (25566 $\pm$ 8 cm^{-1}) discussed in Section B. Since the $\Delta G(v + 1/2)$ values are 2200 cm^{-1} or less, we obtain a corresponding systematic error of $\pm$ 0.7 cm^{-1} or less.

The experimental $\Delta G(v + 1/2)$ values for H_2^+, HD^+, and D_2^+ are listed in column 2 of Tables I, II, and III, respectively. Column 3 lists the theoretical values of Hunter, Yau, and Pritchard[12] (HYP) for H_2^+ and D_2^+, and of Wolniewicz and Poll[13] (WP) for HD^+. Column

4 contains the available values from Rydberg series limits tabulated by Huber and Herzberg.[6] The agreement between experiment and theory is generally quite good. The number of cases for which the theoretical $\Delta G(v + 1/2)$ falls within our statistical uncertainty is 14 out of 17 for H_2^+, 19 out of 20 for HD^+, and 21 out of 23 for D_2^+. The stated accuracy of the HYP calculations performed in the adiabatic approximation is 0.1-0.2 cm^{-1} for H_2^+ and D_2^+, whereas for HD^+ the WP calculations include relativistic, radiative, and nonadiabatic corrections and are expected to be accurate to 0.001 cm^{-1}. The precision of our results is best in the case of HD^+ for which the Q(0) transitions contribute about 90% of the intensity in each vibrational peak and worst in the case of D_2^+ where the Q(0) components are less than 67% of the total intensity.

The vibrational constants are defined by the expression

$$G(v) = \omega_e(v + 1/2) - \omega_e x_e(v + 1/2)^2 + \omega_e y_e(v + 1/2)^3 + \omega_e z_e(v + 1/2)^4 + \ldots \qquad (2)$$

and can be evaluated by fitting $\Delta G(v + 1/2)$ to a power series in $v + 1/2$. In Fig. 14 are shown the experimental $\Delta G(v + 1/2)$ curves for the three ions. They are similar in shape to the corresponding curve for the X $^1\Sigma_g^+$ ground state of H_2 obtained by Herzberg and Howe[30] from the analysis of the H_2 Lyman bands. The curvature is positive for low $v + 1/2$ with a point of inflection at 7-1/2, 9-1/2, and 10-1/2 for H_2^+, HD^+, and D_2^+ respectively, followed by a region of negative curvature as the dissociation limit is approached. This shape is made more

apparent by removing a linear term from the $\Delta G(v + 1/2)$ curve, an example of which is shown in Fig. 15 for the case of H_2^+. Although Herzberg and Howe found that the full accuracy of their ΔG values ($\pm$ 0.05 cm^{-1}) could not be represented by a single power series expansion, we have been able to represent our data adequately within the statistical uncertainty by least-squares fitting to four-term formulas. The coefficients and the corresponding vibrational constants are presented in Tables IV and V. We have also fitted in the same manner the HYP and WP theoretical energy levels, and although they are not an exact representation of the theoretical energies the resulting vibrational constants are listed for comparison in Table V. It is seen that agreement to within our statistical uncertainty is achieved for all the constants of HD^+ and D_2^+, and that the theoretical constants of H_2^+ are slightly larger in magnitude than our measured values. Because of the inadequacy of the four-term formula in fitting the theoretical energies, it is more meaningful to make a direct comparison of the $\Delta G(v+1/2)$ values to establish the consistency between theory and experiment.

An additional quantity of interest is the dissociation energy, D_0^0, which we have evaluated by integrating $\Delta G(v+1/2)$ from $v+1/2=0$ to the intercept using the parameters given in Table IV. These results are listed together with other experimental and theoretical values in Table VI. Considering the possible inaccuracies in this method of evaluation, the agreement reached is reassuring and constitutes a useful check on the accuracy of the present vibrational constants.

4. Vibrational Cross Sections

The 77K spectra of p-H_2, HD, and D_2 in Figs. 7-9 were used to determine the vibrational intensity distributions, because of the absence of complications arising from rotational structure apparent in the higher temperature spectra. The areas of all observed peaks were determined from the peak-fitting procedure described in the previous section. To convert these areas into photoionization cross sections we must consider the effects of 1) the angular distribution of photoelectrons, and 2) the transmission of the analyzer as a function of kinetic energy.

Because the electrons were sampled at an angle of 90° from the photon propagation direction (rather than at the "magic" angle of 54.7°) the observed peak areas must be corrected to obtain the relative cross sections if the asymmetry parameter, β, varies as a function of vibrational state. The predominant rotational transitions in these spectra are $J'=0 \leftarrow J''=0$, for which Dill[31] has shown that β equals 2.0 independent of the v-state. The higher rotational components of the Q branch (mainly Q(1)) appearing in the 77K spectra are predicted by Itikawa[21] and Dill[31] to have β-values close to 2.0 which change only slightly with v-state. The precision of the experiment does not warrant a correction for this smaller effect. A more appreciable angular distribution effect results from the presence of the S branch (mainly $J'=2 \leftarrow J''=0$) seen as a shoulder on the first few v-states of p-H_2 in Fig. 5. For the S branch β is significantly less than 2.0, and we find that the S branch intensity decreases rapidly relative to

the Q branch with increasing v-state. Since the β-value for the S branch is in some dispute (see Itikawa[21]), we have measured the rotationally-resolved angular distribution of the H_2^+ (v=0) state using two lamps oriented at 90° and 54.7° from the electron trajectory. This measurement will be described fully in Chapter IV, but for the purpose of correcting the present H_2^+ vibrational intensity distribution we have used the values $\beta_Q = 2.0$ and $\beta_S = 1.0$ for all v-states. The correction turns out to be less than 0.5% of the area of the peak for all the transitions of H_2^+, which is less than the statistical uncertainty in the areas. No attempt was made to correct the HD^+ and D_2^+ intensities for the angular distribution effect because the S branch contributions to the areas could not be determined accurately, and the magnitude of the correction would be quite small in any case.

The transmission of the analyzer as a function of kinetic energy provides the principal source of error in the vibrational cross sections. The spectra of N_2 and CO at 584Å were recorded during the course of the present experiments, and the observed intensities were compared with those measured by Gardner and Samson[32] using a calibrated analyzer of moderate resolution (45 meV). The resulting transmission curve for our spectrometer exhibits a decrease of about 20% across the kinetic energy range covered by the hydrogen scans. However, there is considerable scatter in the results despite the likelihood that the actual transmission is a smooth function of kinetic energy. The discrepancies might arise from errors in the vibrationally-resolved β-values for N_2 and CO,[33] or more probably

from the fact that with our higher resolution and sensitivity the spectra take on a rather different appearance, and a direct comparison with Gardner and Samson may not be appropriate. For the case of the hydrogen vibrational cross sections we present both the uncorrected data and the data corrected with a transmission function derived by fitting a linear function to the results from N_2 and CO. In most cases the two sets of cross sections differ by less than 10%, and this provides a reasonable estimate of the maximum systematic error in the results. By comparison the statistical error is always much smaller, being about 1% or less for H_2 and HD.

The present spectra show the vibrational states with a good signal-to-background ratio out to quite near the dissociation limit, thus permitting us to place the vibrational cross sections on an absolute scale by summing the peak areas and equating the sum to the total ionization cross section (less the dissociative ionization cross section). We have taken a weighted average of the values determined by Bennet, et al.[34] (6.51 ± 0.33 Mb), Starr and Lowenstein[35] (6.19 ± 0.31 Mb), and Brolley, et al.[36] (6.48 ± 0.17 Mb) to obtain the value of 6.41 Mb for the 584Å photoionization cross section of H_2. The HD and D_2 cross sections are expected to be equal to that of H_2 at 21.2 eV, since the excitation energy is well above all bound ionic states. The assumption has been verified by Lee, Carlson, and Judge[37] who measured essentially identical absorption cross sections for H_2 and D_2 in the 21 eV region using synchrotron radiation. The fraction of dissociative ionization at 584Å has been measured for H_2 (H^+/H_2^+ = 0.0205)

and D_2 ($D^+/D_2^+ = 0.0080$) by Browning and Fryar,[38] and for HD we have used the theoretical value ($H^+(D^+)/HD^+ = 0.013$) of Ford, Docken, and Dalgarno[22] which is expected to be accurate in light of the good agreement between theory and experiment for H_2 and D_2. (It should also be possible to determine the fraction of dissociative ionization from the ratio of the continuum intensity to the bound state intensity in the 584Å photoelectron spectra. From the p-H_2 spectrum at 77K we arrive at a value of 0.01 to 0.04 depending on how the continuum intensity is extrapolated to zero kinetic energy.) The bound state photoionization cross sections at 584Å are thus 6.28 Mb, 6.33 Mb, and 6.36 Mb for H_2, HD, and D_2, respectively.

Tables VII, VIII, and IX list the measured vibrational cross sections together with the theoretical values which are available in the case of H_2 and D_2. The results are plotted in Fig. 16. The correction for the analyzer transmission is seen to be fairly small relative to the overall variation in the cross section by two orders of magnitude. Probably of greatest interest here are the cross sections for the higher v-states, many of which are reported for the first time. The relative intensities for states with v greater than 9 are rather insensitive to transmission effects because the variation in kinetic energy is less than 1 eV over this portion of the spectrum. Whether one chooses to compare the corrected or the uncorrected results with the theoretical values of ONeil and Reinhardt,[23] the agreement between experiment and theory is quite good for all v-states. The approach of ONeil and Reinhardt uses the molecular frame, Hund's case b description of photoionization, where both the initial and final states are

described by high quality CI wave functions, and the angular momentum of the outgoing wave is not specified. The transition moment, which depends explicitly on the internuclear distance and the photoelectron energy, is calculated using the moment-imaging technique to extract the continuum oscillator strength. The vibrational cross sections are then obtained by numerical integration of the transition moment over the initial and final state vibrational wave functions. The effect of rotation-vibration interaction is neglected, but a direct comparison with the present results is still appropriate, because the spectra are nearly rotationless, and rotational coupling effects have been predicted to be rather small.[17]

The question might be raised as to whether the good agreement between theory and experiment achieved for H_2 and D_2 would also be observed for HD, or whether there would be additional complications in the heteronuclear case. The dipole moment of HD^+ might have an effect on the vibrational cross sections due to long-range interaction between the vibrating core and the outgoing electron (i.e., non-Born-Oppenheimer behavior). Another factor to consider would be the rotational selection rules for HD which permit $\Delta J=\pm 1$ (R and P branches). Our peak fitting procedure for the 77K spectrum of HD indicates that most of the intensity is in the Q and S branches, with the R branch contributing less than about 3%, so that a major effect on the vibrational cross sections is not anticipated. It is hoped that these questions will be answered when accurate theoretical results become available.

The theoretical cross sections of Itikawa[20] which were calculated using a single (ℓ = 1) partial wave are seen to be in good agreement with experiment for the higher v-states but are systematically low for v less than 9. This situation is not changed significantly by the inclusion of higher partial waves,[21] and ONeil and Reinhardt[23] point out that the discrepancy at the lower v-states is due to error in Itikawa's transition moment. The results of Ford, Docken, and Dalgarno[22] rely on a more approximate theory but nevertheless agree fairly well with experiment for v greater than 4.

The present cross sections may be compared with previously reported relative photoelectron intensities by an appropriate scaling of the data, and we find that the agreement is fairly good (within 5 - 10%) for the results of Berkowitz and Spohr[2] on H_2^+, HD^+, and D_2^+ (v = 0 to 9 or 10) and of Gardner and Samson[4] on H_2^+ (v = 0 to 9). However, Gardner and Samson give intensities significantly lower than ours for v = 10 to 15. The source of the discrepancy is most likely the the noticeable background and unresolved rotational components falling between the predominant Q(1) transitions in their room temperature spectrum of n-H_2 (see Fig. 2 of this paper for comparison). This led Gardner and Samson to conclude that Itikawa's cross sections[17] were too high at the upper v-states, whereas our data support a different conclusion, namely that Itikawa's results are accurate for high v but too low for v less than 9. The good agreement between the present values and those of ONeil and Reinhardt indicates that the vibrational photoionization cross sections of hydrogen have now been both

measured experimentally and understood theoretically in a very satisfactory manner.

5. Rotational Energy Levels

The rotational constants of H_2^+, HD^+, and D_2^+ were determined from the higher temperature spectra shown in Figs. 10-12. In the case of H_2^+ the room temperature spectrum of p-H_2 was also used. The peaks were located visually to an accuracy of 5 to 10 cm^{-1}, because the incomplete resolution made it impractical to use a fitting procedure. The Q branch transitions were analyzed by least-squares fitting to the formula

$$\nu = \nu_0 + (B_v' - B_0'')\, J(J + 1) - (D_v' - D_0'')\, J^2(J + 1)^2 \qquad (3)$$

where the second order term was used only in the case of H_2^+ for which it was justified by the precision of the data. From Huber and Herzberg[6] we obtained the B_0'' values of 59.336, 44.670, and 29.907 cm^{-1} for H_2, HD, and D_2 and the D_0'' value of 0.046 cm^{-1} for H_2. The ionic rotational constants are listed in Table X and are plotted in Figs. 17 and 18. The B_v' curves were least-squares fitted to the formula

$$B_v = B_e - \alpha_e(v + 1/2) \qquad (4)$$

and the resulting equilibrium rotational constants and internuclear distances are presented in Table XI. The values for B_e and r_e are in agreement with the Rydberg series results to within our statistical

uncertainty, but the present α_e values are consistently lower than those measured previously. This is a consequence of the fact that the B_v curves initially have a slight positive curvature, so that the slope is steeper over the region observed in Rydberg series than it is for the higher v-states. Also shown in Fig. 17 is the theoretical B_v curve of H_2^+ obtained by Beckel, Hansen, and Peek[11] by fitting a fourth order polynomial in J(J+1) to their calculated rotational energies (which were essentially identical to the rotational energies of HYP). In general the theoretical curve falls within our error limits, although the measured values seem to be systematically higher than the theoretical ones, a trend which is also apparent in the photoelectron-derived data of Morioka, Hara, and Nakamura.[5]

D. SUMMARY

The high resolution 584Å photoelectron spectra of n-H_2, p-H_2, HD, and D_2 were measured in a molecular beam experiment to obtain improved spectroscopic constants for H_2^+, HD^+, and D_2^+, and to determine the photoionization cross sections as a function of ionic vibrational state. The vibrational differences, $\Delta G(v+1/2)$, for the ions were measured to an accuracy of about 2 cm^{-1} for H_2^+ and HD^+ and about 5 cm^{-1} for D_2^+, and in nearly all cases these results were in agreement with the theoretical $\Delta G(v+1/2)$ values to within our expected accuracy. These experiments do not constitute a definitive test of the theory, because the calculated level energies should be considerably more accurate than our measured values, as has been confirmed for some levels

of HD^+ by infrared laser experiments.[7,8] However, the present measurements do provide a valuable check on the correctness of the theory for many ionic levels that are likely to be very difficult to observe by optical techniques. The $\Delta G(v+1/2)$ curves were least-squares fitted to four-term formulas, thereby giving ω_e, $\omega_e x_e$, $\omega_e y_e$, and $\omega_e z_e$ for each of the three ions. D_0^0, B_e, α_e, and r_e were also determined and found to be consistent with previous experimental and theoretical results.

The vibrational photoionization cross sections were measured for nearly all the bound states of H_2^+, HD^+, and D_2^+ to an accuracy of 5-10%, with the transmission function of the analyzer being the principal source of uncertainty. The results were in very good agreement with the theoretical H_2^+ and D_2^+ cross sections of ONeil and Reinhardt,[23] calculated using the body-frame Hund's case b description and the Stieltjes moment-imaging procedure. The discrepancy that existed in the literature between experiment and theory for the high v-states of H_2^+ has now been resolved.

We have not discussed the rotational intensity distributions in the photoelectron spectra of hydrogen, because this topic is closely related to the study of the rotational relaxation of the molecules in a supersonic expansion. We have performed measurements of the rotational populations as a function of stagnation temperature and pressure by photoelectron spectroscopy, and these results will be discussed in Chapter V.

REFERENCES

* This chapter (LBL-13696) was submitted to the Journal of Chemical Physics for publication.

1. L. Åsbrink, Chem. Phys. Lett., 7, 549 (1970).
2. J. Berkowitz and R. Spohr, J. Electron. Spectros. Relat. Phenom., 2, 143 (1973).
3. T. H. Lee and J. W. Rabalais, J. Chem. Phys., 61, 2747 (1974).
4. J. L. Gardner and J. A. R. Samson, J. Electron. Spectros. Relat. Phenom., 8, 123 (1976).
5. Y. Morioka, S. Hara, and M. Nakamura, Phys. Rev. A, 22, 177 (1980).
6. K. P. Huber and G. Herzberg, Constants of Diatomic Molecules, Van Nostrand Reinhold, New York (1979).
7. W. H. Wing, G. A. Ruff, W. E. Lamb, Jr., and J. J. Spezeski, Phys. Rev. Lett., 36, 1488 (1976).
8. A. Carrington, J. Buttenshaw, and P. G. Roberts, Mol. Phys., 38, 1711 (1979).
9. A. Carrington and J. Buttenshaw, Mol. Phys., 44, 267 (1981).
10. G. Hunter and H. O. Pritchard, J. Chem. Phys., 46, 2153 (1967).
11. C. L. Beckel, B. D. Hansen, and J. M. Peek, J. Chem. Phys., 53, 3681 (1970).
12. G. Hunter, A. W. Yau, and H. O. Pritchard, At. Data Nucl. Data Tables, 14, 11 (1974).
13. L. Wolniewicz and J. D. Poll, J. Chem. Phys., 73, 6225 (1980).
14. D. M. Bishop and L. M. Cheung, J. Chem. Phys., 75, 3155 (1981).
15. D. M. Bishop, Mol. Phys., 28, 1397 (1974).

16. D. M. Bishop and L. M. Cheung, Phys. Rev. A, 16, 640 (1977).

17. D. Villarejo, J. Chem. Phys., 49, 2523 (1968), and references contained therein.

18. Y. Itikawa, J. Electron. Spectros. Relat. Phenom., 2, 125 (1973).

19. Y. Itikawa, Chem. Phys., 28, 461 (1978).

20. Y. Itikawa, Chem. Phys., 30, 109 (1978).

21. Y. Itikawa, Chem. Phys., 37, 401 (1979).

22. A. L. Ford, K. K. Docken, and A. Dalgarno, Astrophys. J., 195, 819 (1975).

23. S. V. ONeil and W. P. Reinhardt, J. Chem. Phys., 69, 2126 (1978).

24. J. E. Pollard, D. J. Trevor, Y. T. Lee, and D. A. Shirley, Rev. Sci. Instrum., 52, 1837 (1981); and this thesis, Chapter II.

25. A. Lofthus and P. H. Krupenie, J. Phys. Chem. Ref. Data, 6, 113 (1977).

26. I. Wender, R. A. Friedel, and M. Orchin, J. Amer. Chem. Soc., 71, 1140 (1949).

27. S. L. Anderson, T. Hirooka, P. W. Tiedemann, B. H. Mahan, and Y. T. Lee, J. Chem. Phys., 73, 4779 (1980).

28. C. E. Moore, Atomic Energy Levels, NBS Circular 467 (1949).

29. E. R. Cohen and B. N. Taylor, J. Phys. Chem. Ref. Data, 2, 663 (1973).

30. G. Herzberg and L. L. Howe, Can. J. Phys., 37, 636 (1959).

31. D. Dill, Phys. Rev. A, 6, 160 (1972).

32. J. L. Gardner and J. A. R. Samson, J. Electron. Spectrosc. Relat. Phenom., 8, 469 (1976).

33. J. Kreile and A. Schweig, . Electron. Spectrosc. Relat. Phenom., 20, 191 (1980).

34. S. W. Bennet, J. B. Tellinghuisen, and L. F. Phillips, J. Phys. Chem., 75, 719 (1971).

35. W. L. Starr and M. Lowenstein, J. Geophys. Res. 77, 4790 (1972).

36. J. E. Brolley, L. E. Porter, R. H. Sherman, J. K. Theobald, and J. C. Fong, J. Geophys. Res., 78, 1627 (1973).

37. L. C. Lee, R. W. Carlson, and D. L. Judge, J. Quant. Spectrosc. Radiat. Transfer, 16, 873 (1976).

38. R. Browning and J. Fryar, J. Phys. B: Atom. Molec. Phys., 6, 364 (1973).

Table I. Vibrational differences, $\Delta G(v+1/2)$, of the H_2^+ ground state $^2\Sigma_g^+$, in cm^{-1}

v+1/2	Present results	HYP theory[a]	Rydberg series[b]
.5	2190.9	2191.32	2191.2
1.5	2065.2	2064.09	2064.2
2.5	1941.8	1941.08	1940.8
3.5	1822.1	1821.64	
4.5	1706.2	1705.13	
5.5	1591.1	1590.90	
6.5	1477.7	1478.32	
7.5	1367.0	1366.75	
8.5	1257.8	1255.51	
9.5	1145.8	1143.88	
10.5	1031.9	1031.09	
11.5	913.3	916.31	
12.5	796.6	798.59	
13.5	676.4	676.86	
14.5	548.4	549.97	
15.5	415.4	416.62	
16.5	280.3	275.96	
17.5		131.26	

[a]G. Hunter, A. W. Yau, and H. O. Pritchard, At. Data Nucl. Data Tables, 14, 11 (1974).
[b]G. Herzberg and Ch. Jungen, J. Mol. Spectrosc., 41, 425 (1972).

Table II. Vibrational differences, $\Delta G(v+1/2)$, of the HD^+ ground state $^2\Sigma_g^+$, in cm^{-1}

v+1/2	Present results	WP theory[a]	Rydberg series[b]
.5	1913.1	1912.994	1913.1
1.5	1817.2	1816.862	1816.7
2.5	1722.7	1723.587	1723.7
3.5	1631.8	1632.799	
4.5	1543.0	1544.134	
5.5	1456.8	1457.231	
6.5	1372.0	1371.735	
7.5	1287.5	1287.287	
8.5	1201.7	1203.524	
9.5	1119.4	1120.066	
10.5	1035.2	1036.522	
11.5	951.3	952.469	
12.5	866.2	867.459	
13.5	779.8	781.002	
14.5	693.2	692.557	
15.5	600.6	601.522	
16.5	507.2	507.237	
17.5	409.0	408.975	
18.5	306.1	306.048	
19.5	203.0	198.460	
20.5		90.67	

[a]L. Wolniewicz and J. D. Poll, J. Chem. Phys., 73, 6225 (1980).
[b]K. P. Huber and G. Herzberg, Constants of Diatomic Molecules, Van Nostrand Reinhold, New York (1979).

Table III. Vibrational differences, $\Delta G(v+1/2)$, of the D_2^+ ground state $^2\Sigma_g^+$, in cm^{-1}

v+1/2	Present results	HYP theory[a]	Rydberg series[b]
.5	1583.5	1577.15	1577.3
1.5	1510.0	1512.47	1512.1
2.5	1450.3	1449.40	
3.5	1388.4	1387.81	
4.5	1326.3	1327.51	
5.5	1271.0	1268.36	
6.5	1211.2	1210.18	
7.5	1157.3	1152.83	
8.5	1091.7	1096.13	
9.5	1044.7	1039.95	
10.5	985.8	984.10	
11.5	927.0	928.41	
12.5	872.7	872.73	
13.5	814.3	816.86	
14.5	759.3	760.60	
15.5	702.4	703.77	
16.5	644.7	646.12	
17.5	584.9	587.43	
18.5	523.9	527.43	
19.5	463.7	465.84	
20.5	399.6	402.35	
21.5	327.3	336.63	
22.5	271.0	268.41	
23.5		197.52	
24.5		124.61	
25.5		54.77	
26.5		11.07	

[a]G. Hunter, A. W. Yau, and H. O. Pritchard, At. Data Nucl. Data Tables, 14, 11 (1974)
[b]K. P. Huber and G. Herzberg, Constants of Diatomic Molecules, Van Nostrand Reinhold, New York (1979).

Table IV. Least squares coefficients derived from fittir of the experimental data to the formula $\Delta G(v+1/2) = a_0 + a_1(v+1/2) + a_2(v+1/2)^2 + a_3(v+1/2)^3$, in cm^{-1}

	H_2^+	HD^+	D_2^+
a_0	2257.5	1963.8	1612.7
a_1	-132.80	-100.85	-67.11
a_2	2.815	1.951	1.017
a_3	-0.1232	-0.0724	-0.0308

Table V. Hydrogen molecular ion vibrational constants, in cm^{-1}. Stated error limits are statistical uncertainties ($\pm 2\sigma$) from the least-squares fit. Theoretical constants were obtained by fitting to published energy levels.

	H_2^+			HD^+			D_2^+		
	Present results		HYP theory[a]	Present results		WP theory[b]	Present results		HYP theory[a]
ω_e	2324.4	±2.6	2326.6	2014.6	±1.8	2015.2	1646.4	±5.2	1645.2
$\omega_e x_e$	67.84	±0.64	68.71	51.42	±0.39	51.58	34.07	±0.96	34.20
$\omega_e y_e$	1.00D	±0.059	1.085	0.687	±0.030	0.709	0.354	±0.065	0.371
$\omega_e z_e$	-0.0308	±0.0017	-0.0332	-0.0181	±0.0007	-0.0188	-0.0077	±0.0014	-0.0080

[a]G. Hunter, A. W. Yau, and H. O. Pritchard, At. Data Nucl. Data Tables, 14, 11 (1974).
[b]L. Wolniewicz and J. D. Poll, J. Chem. Phys., 73, 6225 (1980).

Table VI. Hydrogen molecular ion dissociation energies, D_0^o, in cm^{-1}. The first two entries are experimental; the remainder are theoretical.

	H_2^+	HD^+	D_2^+
Present results	21375	21515	21687
Huber and Herzberg[a]	21379.8	21516.4	21711.9
HYP[b]	21379.17	21515.91	21711.47
Bishop[c]	21379.39	21515.99	21711.51
WP[d]		21516.073	

[a]K. P. Huber and G. Herzberg, Constants of Diatomic Molecules, Van Nostrand Reinhold, New York (1979).
[b]G. Hunter, A. W. Yau, and H. O. Pritchard, At. Data Nucl. Data Tables, 14, 11 (1974).
[c]D. M. Bishop, Mol. Phys., 28, 1397 (1974).
[d]L. Wolniewicz and J. D. Poll, J. Chem. Phys. 73, 6225 (1980).

Table VII. Photoionization cross sections (in Mb) for $H_2^+X^2\Sigma_g^+(v') \leftarrow H_2X^1\Sigma_g^+(v''=0)$ at 584Å. Error limits are the statistical uncertainties (± 2σ). Experimental values have been corrected for β. Columns 2 and 3 are the results uncorrected and corrected for analyzer transmission. Columns 4, 5, and 6 are theoretical values.

v'	Uncorrected	Corrected	ONeil and Reinhardt[a]	Itikawa (ℓ = 1)[b]	Ford, et al.[c]
0	.447±.006	.477±.006	.4533	.3879	.53
1	.868±.008	.907±.008	.8639	.7428	1.00
2	1.021±.008	1.048±.008	1.0036	.8722	1.15
3	.966±.007	.975±.007	.9313	.8206	1.05
4	.799±.006	.793±.006	.7656	.6845	.85
5	.611±.005	.598±.005	.5866	.5332	.65
6	.462±.004	.446±.004	.4315	.3971	.47
7	.329±.004	.315±.004	.3105	.2893	.33
8	.236±.003	.223±.003	.2211	.2082	.24
9	.168±.003	.157±.003	.1568	.1493	.16
10	.1183±.0007	.1095±.0007	.1113	.1069	.12
11	.0842±.0006	.0773±.0005	.07927	.0769	.08
12	.0596±.0006	.0543±.0005	.05659	.0554	.06
13	.0416±.0012	.0377±.0011	.04038	.0396	
14	.0293±.0003	.0264±.0003	.02856	.0282	
15	.0199±.0002	.0179±.0002	.01969	.0197	
16	.0124±.0002	.0111±.0002	.01273	.0128	
17	.0077±.0002	.0068±.0002	.006933	.0069	
18			.002162	.0021	
19			.000098		
Sum	6.280	6.280	6.083	5.434	6.69

[a]S. V. ONeil and W. P. Reinhardt, J. Chem. Phys., 69, 2126 (1978).
[b]Y. Itikawa, Chem. Phys., 30, 109 (1978).
[c]A. L. Ford, K. K. Docken, and A. Dalgarno, Astrophys. J., 195, 819 (1975).

Table VIII. Photoionization cross sections (in Mb) for $HD^+ X^2\Sigma_g^+ (v') \leftarrow HD\ X^1\Sigma_g^+ (v''=0)$ at 584Å. Error limits are the statistical uncertainties (± 2σ). Columns 2 and 3 are the results uncorrected and corrected for analyzer transmission.

v'	Uncorrected	Corrected
0	.283±.006	.302±.007
1	.635±.008	.667±.008
2	.877±.009	.907±.009
3	.895±.008	.912±.008
4	.809±.007	.813±.007
5	.685±.006	.679±.006
6	.552±.005	.541±.005
7	.419±.004	.406±.004
8	.321±.004	.307±.004
9	.241±.003	.229±.003
10	.172±.003	.162±.003
11	.128±.002	.119±.002
12	.0918±.0016	.0849±.0015
13	.0662±.0014	.0608±.0013
14	.0485±.0012	.0443±.0011
15	.0354±.0010	.0321±.0009
16	.0260±.0007	.0235±.0006
17	.0185±.0006	.0167±.0005
18	.0125±.0005	.0112±.0004
19	.0084±.0004	.0075±.0004
20	.0057±.0004	.0051±.0003
Sum	6.330	6.330

Table IX. Photoionization cross sections (in Mb) for $D_2^+ X^2\Sigma_g^+(v') \leftarrow D_2 X^1\Sigma_g^+ (v''=0)$ at 584Å. Error limits are the statistical uncertainties (± 2σ). Columns 2 and 3 are the results uncorrected and corrected for analyzer transmission. Column 4 lists the theoretical values.

V'	Uncorrected	Corrected	ONeil and Reinhardt[a]
0	.171±.031	.182±.033	.1744
1	.452±.016	.475±.017	.4597
2	.702±.035	.728±.037	.7008
3	.826±.031	.846±.032	.8160
4	.821±.030	.831±.030	.8097
5	.738±.027	.739±.027	.7247
6	.631±.024	.625±.024	.6054
7	.503±.022	.493±.021	.4825
8	.386±.016	.374±.016	.3725
9	.294±.013	.283±.012	.2815
10	.218±.012	.208±.012	.2099
11	.161±.010	.153±.009	.1553
12	.123±.009	.115±.008	.1145
13	.0913±.0027	.0851±.0025	.08435
14	.0663±.0021	.0614±.0019	.06227
15	.0491±.0018	.0452±.0016	.04614
16	.0363±.0015	.0332±.0014	.03433
17	.0276±.0013	.0251±.0012	.02566
18	.0204±.0011	.0185±.0010	.01925
19	.0155±.0010	.0140±.0009	.01447
20	.0109±.0009	.0098±.0008	.01087
21	.0083±.0007	.0074±.0006	.008101
22	.0051±.0005	.0046±.0004	.005925
23	.0037±.0005	.0033±.0005	.004164
24			.002680
25			.001411
26			.000339
27			.000048
Sum	6.360	6.360	6.227

[a]S. V. ONeil and W. P. Reinhardt, private communication.

Table X. Hydrogen molecular ion rotational constants, in cm^{-1}. Stated error limits are statistical uncertainties ($\pm 2\sigma$) from the least-squares fit.

v	H_2^+ B_v	H_2^+ D_v	HD^+ B_v	D_2^+ B_v
0	29.6±2.5	.03±.08	22.6±1.7	14.9±0.2
1	28.1±1.1	.04±.04	21.5±1.0	14.0±0.4
2	26.4±1.1	.03±.03	20.3±1.1	13.6±0.5
3	24.8±0.5	.02±.02	19.8±1.2	13.1±0.5
4	23.6±1.1	.03±.04	18.7±0.9	13.2±0.6
5	22.3±0.4	.03±.01	18.0±0.4	12.4±0.1
6	21.0±1.3	.02±.04	16.9±0.6	11.8±0.2
7	19.0±0.3	.00±.01	16.6±0.5	11.2±0.2
8	18.3±0.5	.04±.03	15.6±0.3	10.7±0.2
9	17.2±0.6	.05±.03	14.0±0.4	10.3±0.4
10	15.0±0.8	.00±.04	14.0±0.5	9.8±0.4
11	14.5±0.5		14.4±1.6	9.8±0.4
12	12.8±0.6		11.4±0.5	9.0±0.3
13	11.1±0.5		11.9±0.8	8.4±0.4
14	9.9±1.4		9.5±0.7	8.4±0.7
15	8.3±1.0		9.9±1.3	7.6±0.6
16			7.5±1.0	7.2±1.0
17			6.1±1.0	6.4±0.3
18			6.1±1.0	5.4±0.1
19				6.4±0.1

Table XI. Hydrogen molecular ion rotational constants and internuclear distances. Stated error limits are statistical uncertainties ($\pm 2\sigma$) from the least-squares fit.

	H_2^+		HD^+		D_2^+	
	Present results	Rydberg series[a]	Present results	Rydberg series[a]	Present results	Rydberg series[a]
$B_e(cm^{-1})$	29.99±.30	30.2_1	23.03±.63	22.45_2	14.89±.28	15.016
$\alpha_e(cm^{-1})$	1.388±.033	1.68_5	0.901±.057	1.00_1	0.471±.024	0.560
r_e(Å)	1.056±.005	1.052	1.044±.014	1.057	1.060±.005	1.0559

[a]K. P. Huber and G. Herzberg, Constants of Diatomic Molecules, Van Nostrand Reinhold, New York (1979).

FIGURE CAPTIONS

Fig. 1. The electronic ground state potential energy curves for H_2 and H_2^+, adapted from T. E. Sharp, At. Data, 2, 119 (1971).

Fig. 2. The 584Å photoelectron spectrum of n-H_2 expanded from 800 Torr at 297K. The ionic vibrational states and the rotational quantum numbers of a typical Q branch are indicated in the figure. The S branch is also labeled for the first three v-states.

Fig. 3. The spectrum of p-H_2 expanded from 800 Torr at 297K.

Fig. 4. The spectrum of HD expanded from 600 Torr at 297K.

Fig. 5. The spectrum of D_2 expanded from 1000 Torr at 297K.

Fig. 6. Three examples of the dependence of the rotational excitation on the nozzle temperature.

Fig. 7. The spectrum of p-H_2 expanded from 200 Torr at 77K.

Fig. 8. The spectrum of HD expanded from 200 Torr at 77K.

Fig. 9. The spectrum of D_2 expanded from 200 Torr at 77K.

Fig. 10. The spectrum of n-H_2 expanded from 600 Torr at 473K.

Fig. 11. The spectrum of HD expanded from 50 Torr at 297K.

Fig. 12. The spectrum of D_2 expanded from 400 Torr at 403K.

Fig. 13. The H_2^+ (v'=2) transition for p-H_2 expanded from 77K. (a) Experimental points with the line representing the least-squares fit. (b) Experimental points with the decomposition into the four labeled rotational components.

Fig. 14. The vibrational differences of H_2^+, HD^+, and D_2^+ determined from photoelectron spectra of p-H_2, HD, and D_2 at 77K shown in Figs. 7-9.

Fig. 15. The vibrational differences of H_2^+ as in Fig. 7, but with a linear term, 2242.6 - 116.93 (v + 1/2), subtracted. The curve is derived from the HYP theoretical energy levels.

Fig. 16. The vibrational photoionization cross sections of H_2, HD, and D_2 determined from the 584Å photoelectron spectra at 77K shown in Figs. 7-9. Theoretical values are from ONeil and Reinhardt (Ref. 23).

Fig. 17. The rotational constants of H_2^+ determined from the spectra of n-H_2 at 473K shown in Fig. 10 and p-H_2 at 297K shown in Fig. 3. Error bars are statistical uncertainties (± 2σ) from the least-squares fit to Eq. (3). The solid line gives the theoretical B_v values of Beckel, Hansen, and Peek (Ref. 11).

Fig. 18. The rotational constants of HD^+ and D_2^+ determined from the spectra of HD and D_2 shown in Figs. 11 and 12. Error bars are statistical uncertainties (± 2σ) from the least-squares fit to Eq. (3) omitting the second order term.

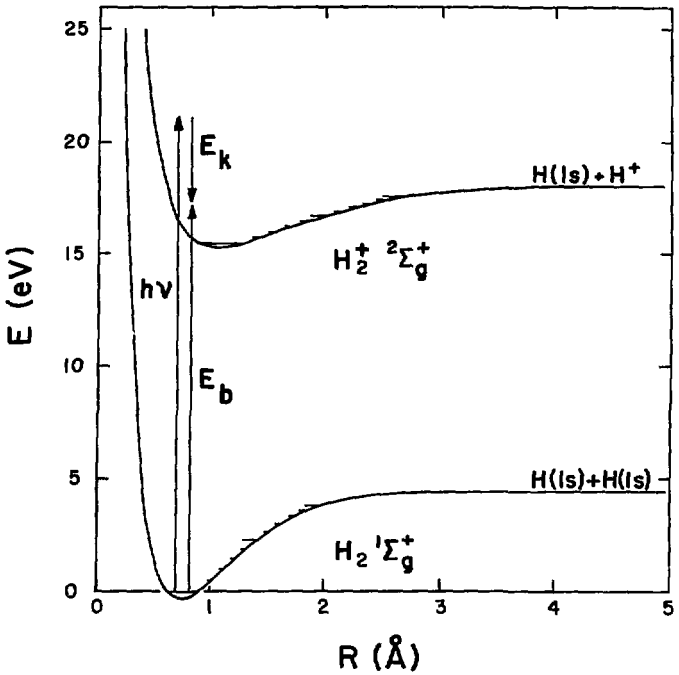

XBL 8110-12222

Figure 1

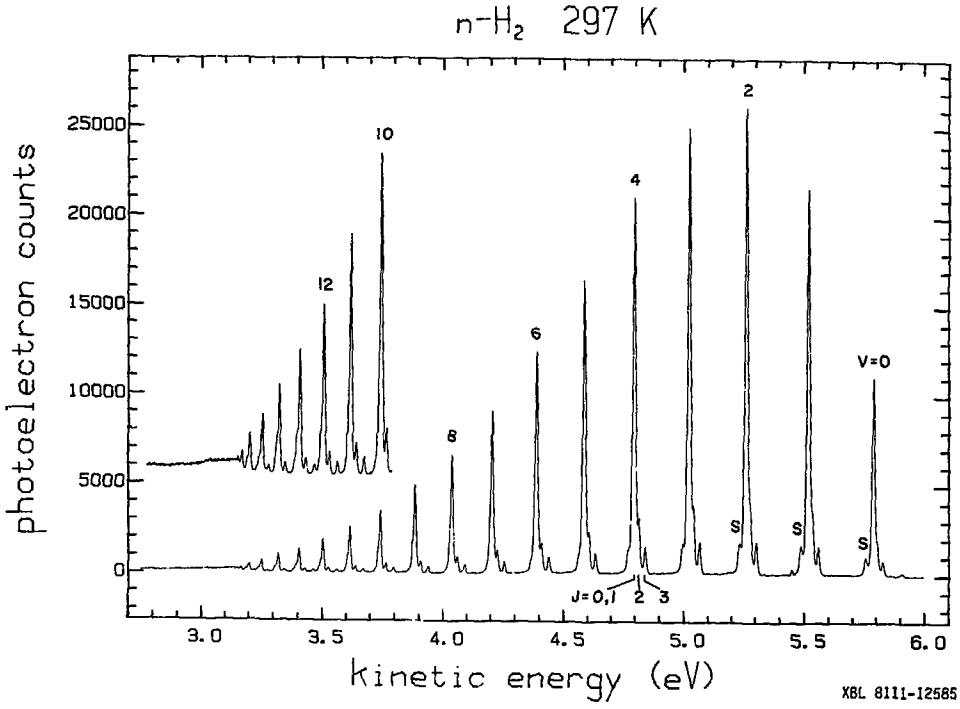
n-H2 297 K
photoelectron counts
25000
20000
15000
10000
5000
0
3.0
3.5
4.0
4.5
5.0
5.5
6.0
kinetic energy (eV)
12
10
8
6
4
2
V=0
S
S
S
J=0,1
2
3
XBL 8111-12585

Figure 2

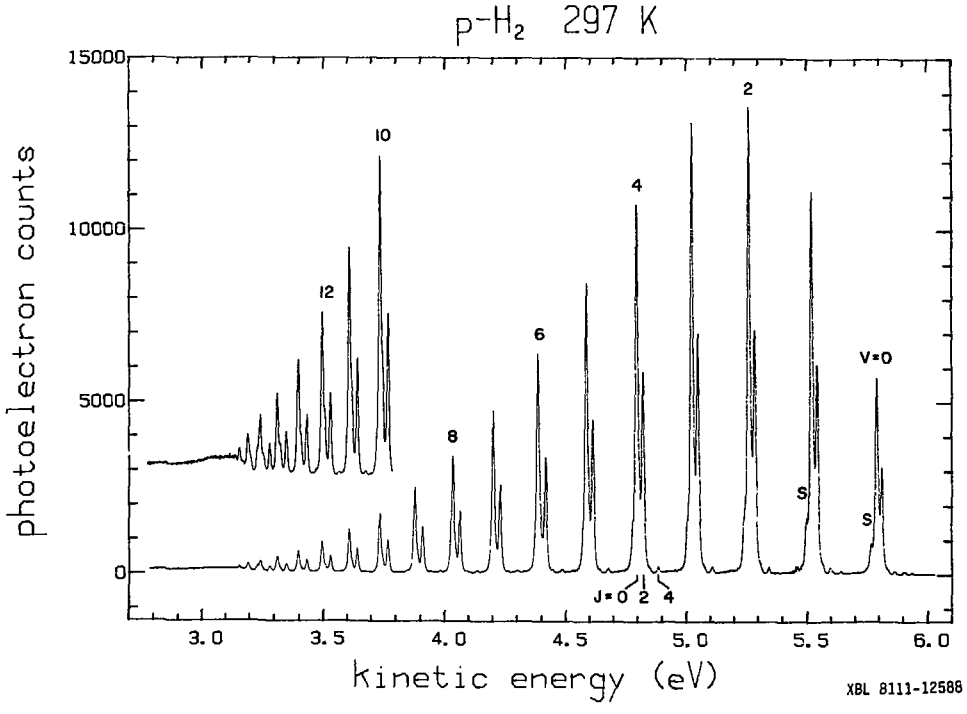
p-H2 297 K
15000
10000
5000
0
photoelectron counts
12
10
8
6
4
2
V=0
S
S
J=0 2 4
3.0
3.5
4.0
4.5
5.0
5.5
6.0
kinetic energy (eV)
XBL 8111-12588

Figure 3

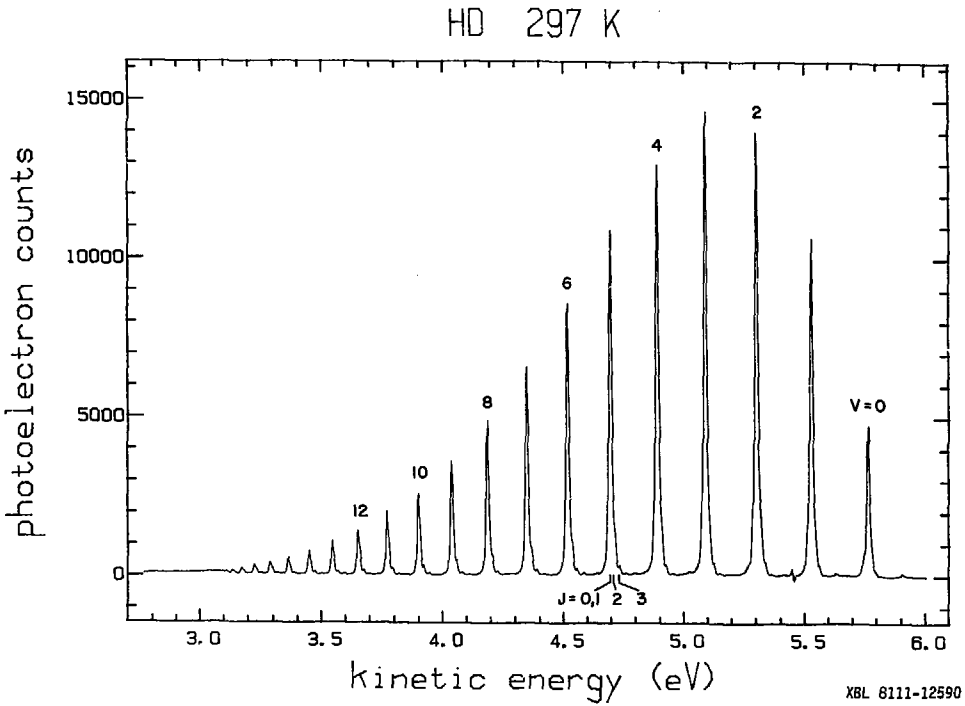
HD 297 K
photoelectron counts
15000
10000
5000
0
3.0
3.5
4.0
4.5
5.0
5.5
6.0
kinetic energy (eV)
12
10
8
6
4
2
V=0
J=0,1 2 3
XBL 8111-12590

Figure 4

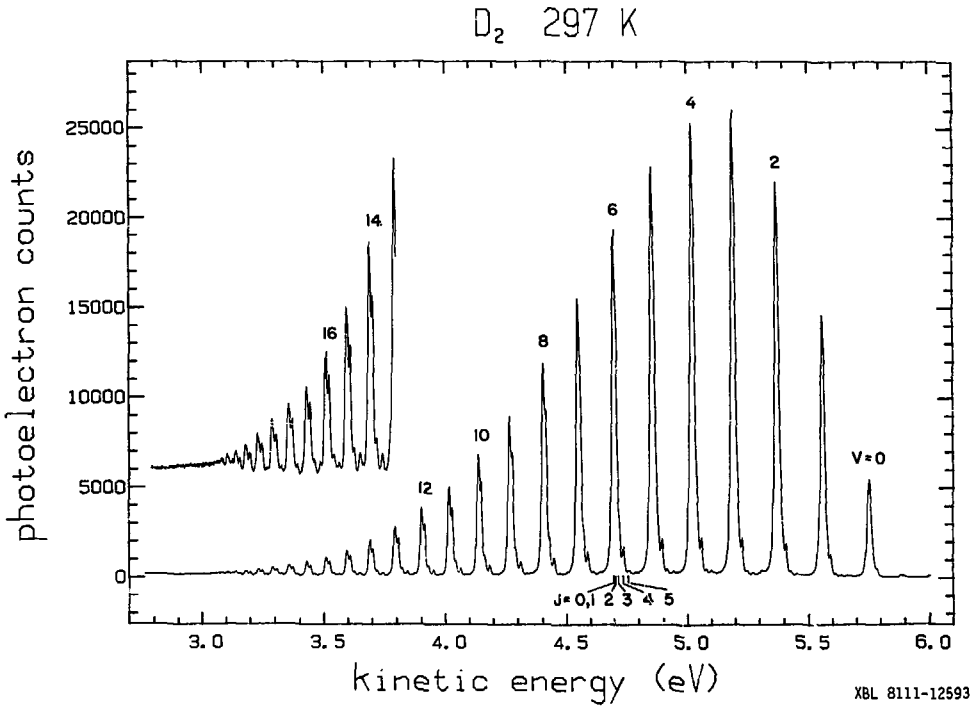
D2 297 K
photoelectron counts
25000
20000
15000
10000
5000
0
16
14
12
10
8
6
4
2
V=0
J=0,1 2 3 4 5
3.0
3.5
4.0
4.5
5.0
5.5
6.0
kinetic energy (eV)
XBL 8111-12593

Figure 5

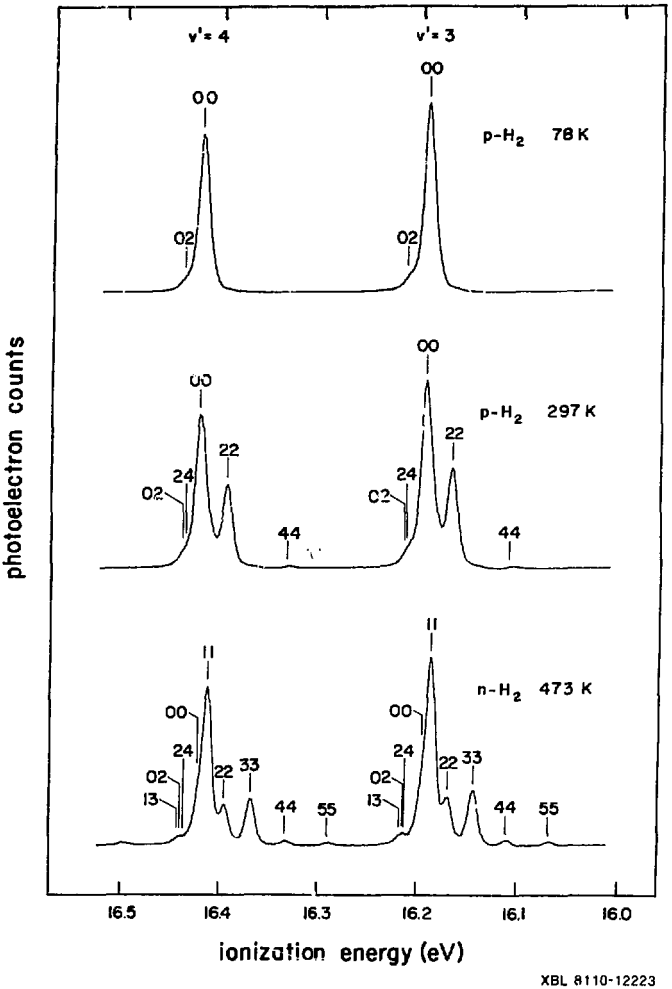

XBL 8110-12223

Figure 6

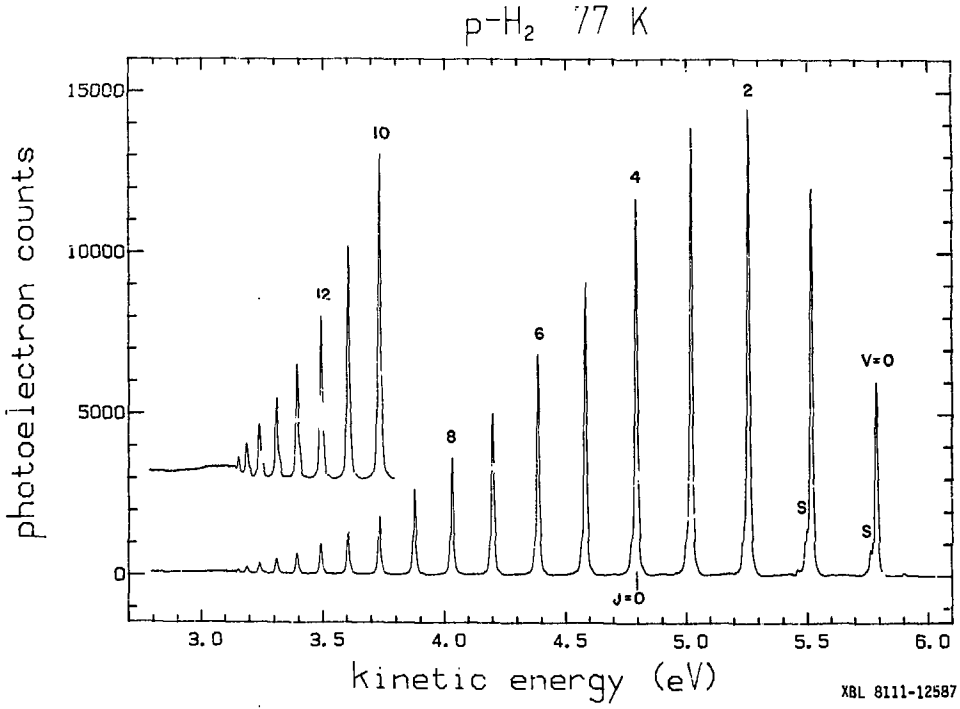
p-H2 77 K
photoelectron counts
15000
10000
5000
0
3.0
3.5
4.0
4.5
5.0
5.5
6.0
kinetic energy (eV)
12
10
8
6
4
2
V=0
S
S
J=0
XBL 8111-12587

Figure 7

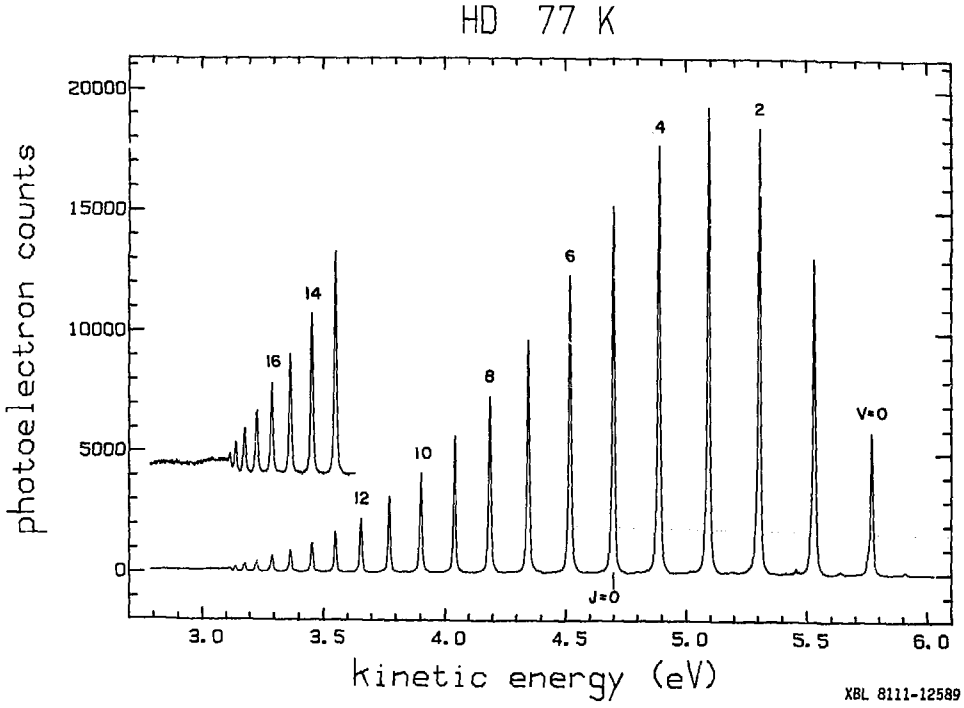
HD 77 K
photoelectron counts
20000
15000
10000
5000
0
16
14
12
10
8
6
4
2
V=0
J=0
3.0
3.5
4.0
4.5
5.0
5.5
6.0
kinetic energy (eV)
XBL 8111-12589

Figure 8

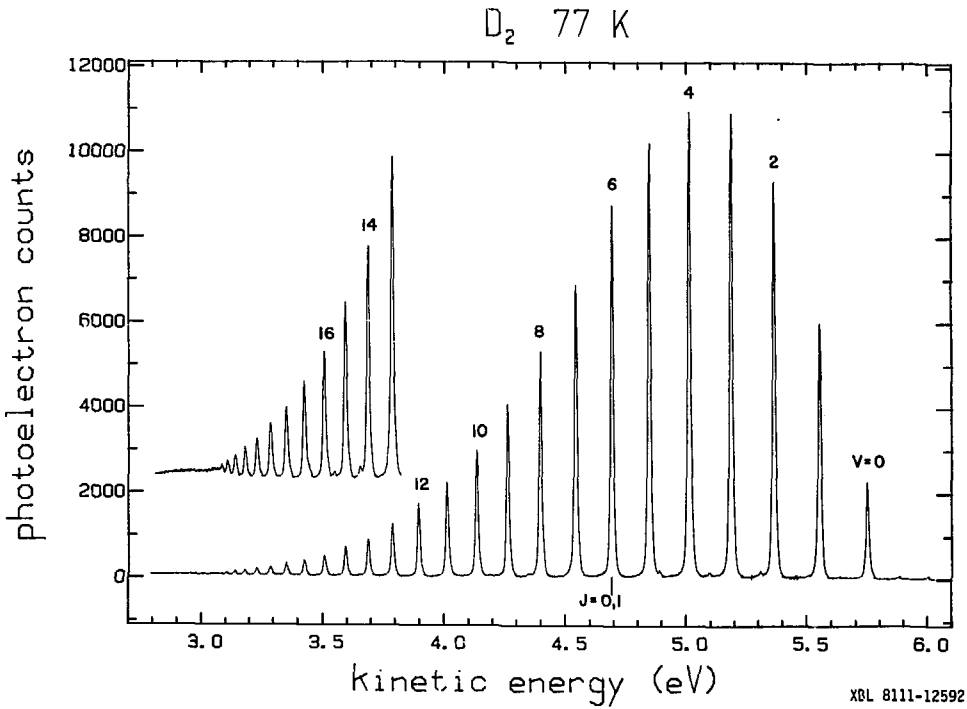
D2 77 K
photoelectron counts
12000
10000
8000
6000
4000
2000
0
3.0
3.5
4.0
4.5
5.0
5.5
6.0
kinetic energy (eV)
16
14
12
10
8
6
4
2
V=0
J=0,1
XBL 8111-12592

Figure 9

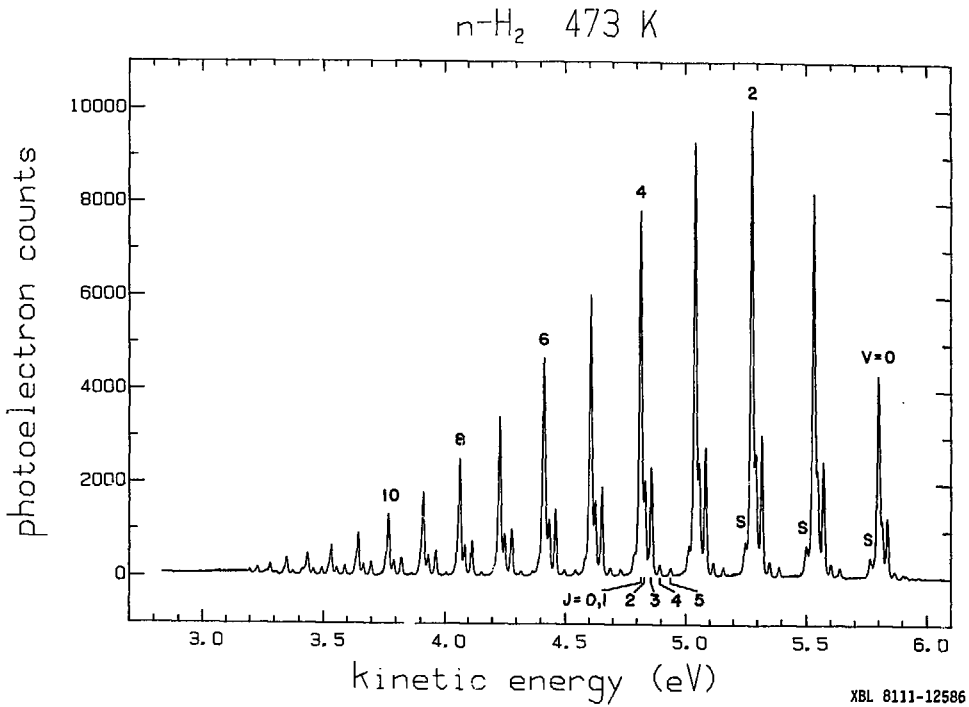
n-H2 473 K
photoelectron counts
10000
8000
6000
4000
2000
0
3.0
3.5
4.0
4.5
5.0
5.5
6.0
kinetic energy (eV)
10
8
6
4
2
V=0
S
S
S
J=0,1 2 3 4 5
XBL 8111-12586

Figure 10

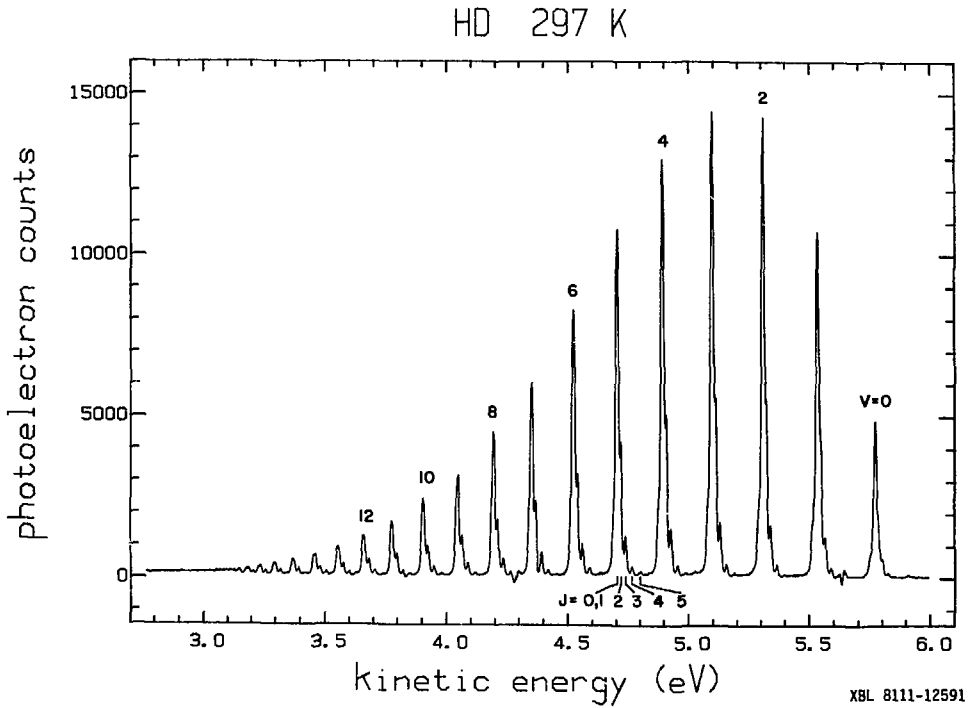
HD 297 K
photoelectron counts
15000
10000
5000
0
3.0
3.5
4.0
4.5
5.0
5.5
6.0
kinetic energy (eV)
12
10
8
6
4
2
V=0
J= 0,1 2 3 4 5
XBL 8111-12591

Figure 11

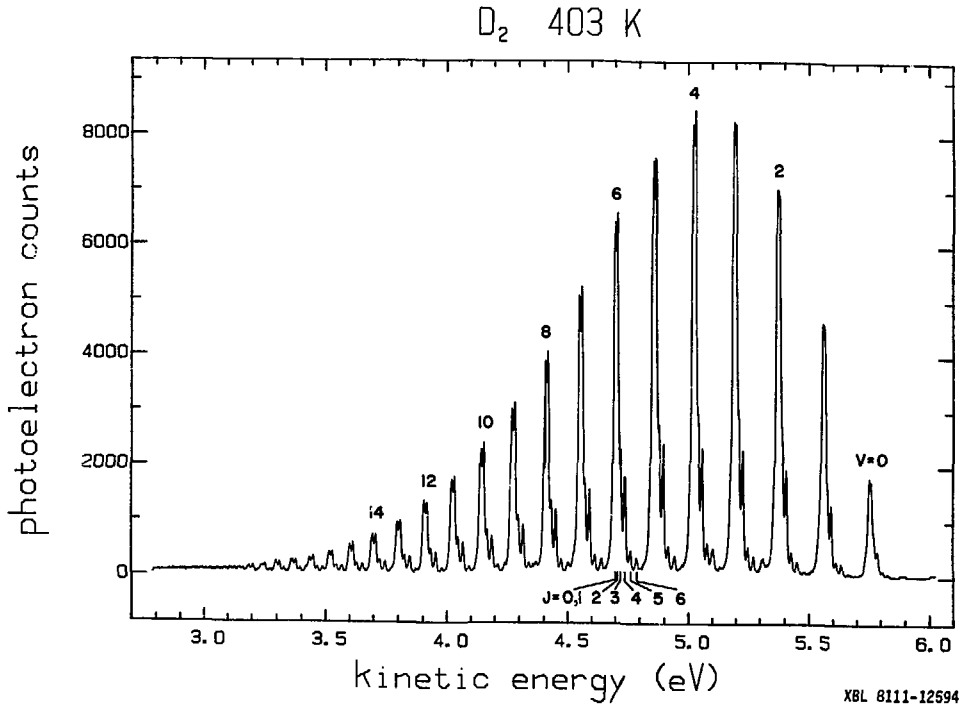
D2 403 K
photoelectron counts
8000
6000
4000
2000
0
3.0
3.5
4.0
4.5
5.0
5.5
6.0
kinetic energy (eV)
14
12
10
8
6
4
2
V=0
J=0,1 2 3 4 5 6
XBL 8111-12594

Figure 12

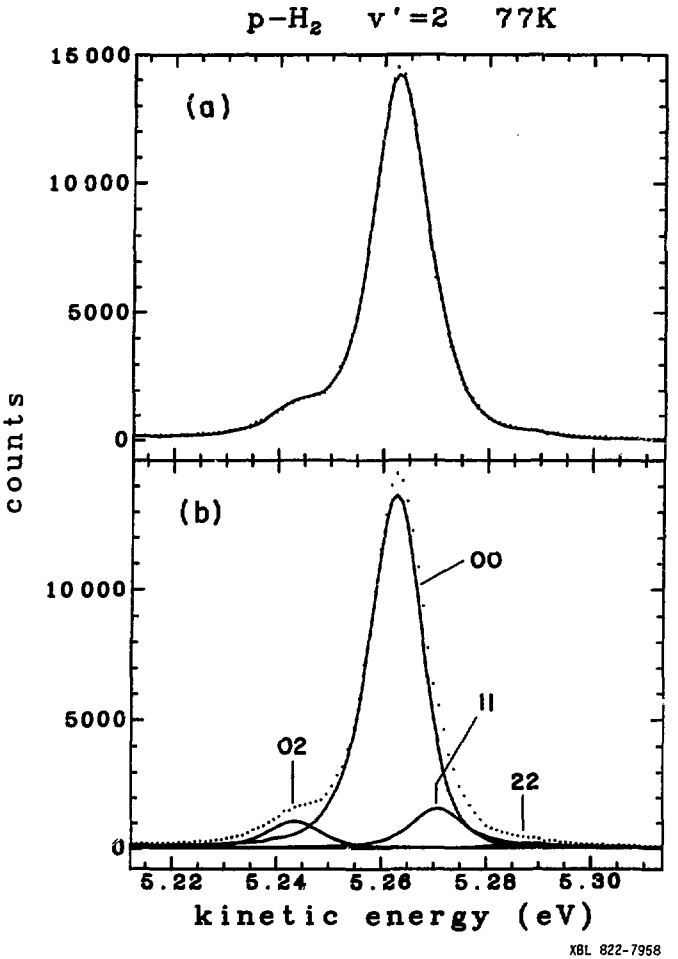

XBL 822-7958

Figure 13

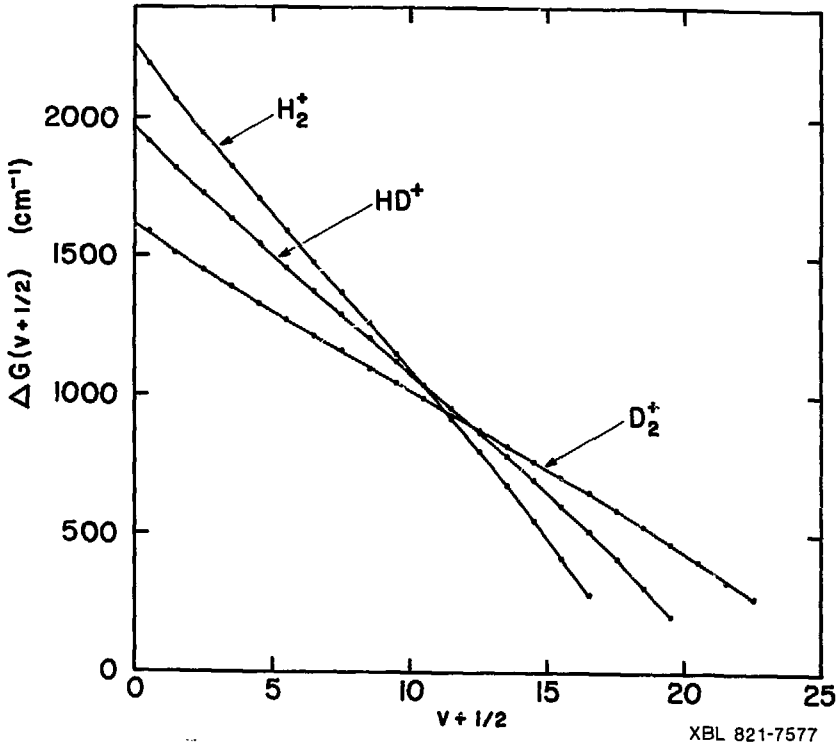
2000
1500
1000
500
0
$\Delta G(v+1/2)$ (cm^{-1})
H_2^+
HD^+
D_2^+
0
5
10
15
20
25
$v+1/2$
XBL 821-7577

Figure 14

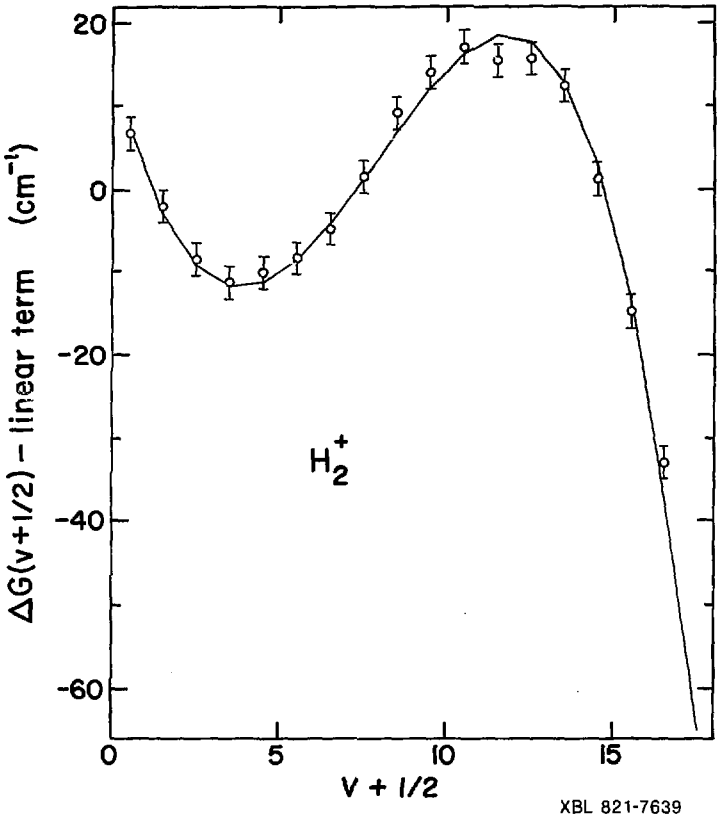

Figure 15

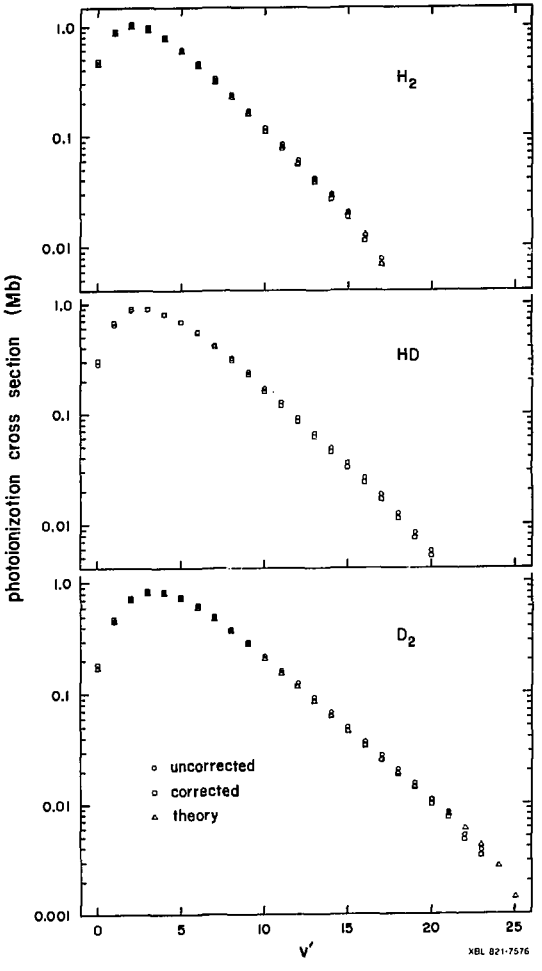
photoionization cross section (Mb)
1.0
0.1
0.01
0.001
H2
HD
D2
uncorrected
corrected
theory
0
5
10
15
20
25
v'
XBL 821-7576

Figure 16

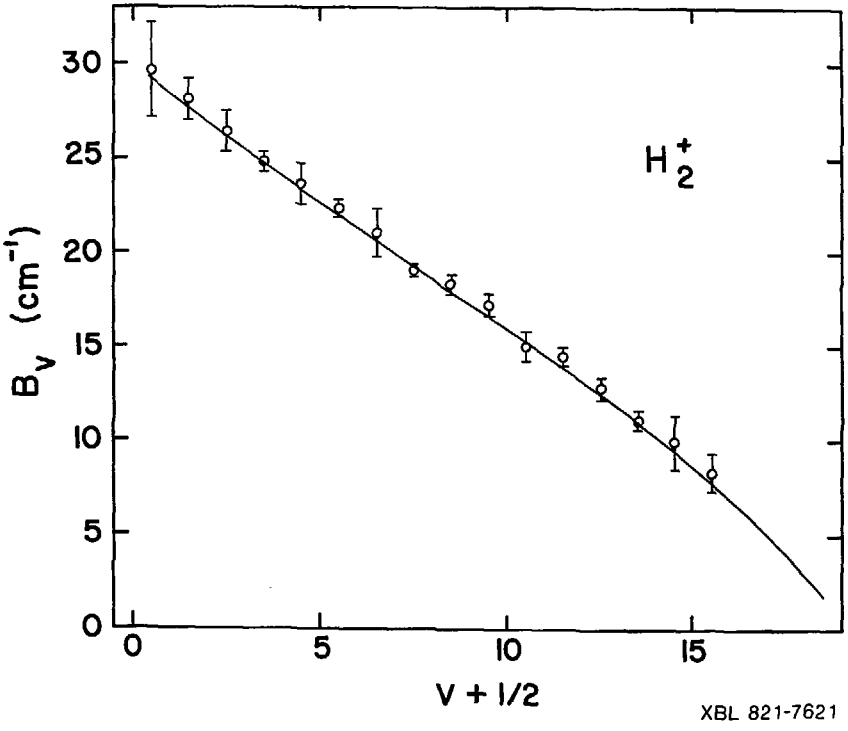

Figure 17

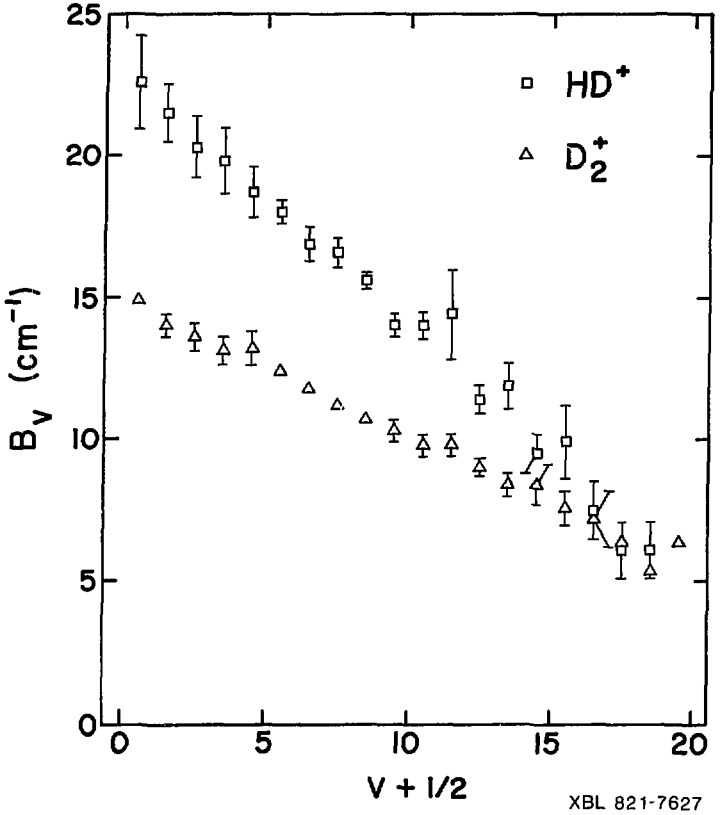

Figure 18

IV. ROTATIONALLY-RESOLVED PHOTOELECTRON ANGULAR DISTRIBUTIONS FOR H_2^+ (v'=0) AT λ=584 Å AND 736Å*

ABSTRACT

The photoelectron asymmetry parameter for H_2^+ (v'=0) was measured for the S rotational branch at λ=584Å and 736Å using a supersonic beam of n-H_2. Comparison with the theoretical β-values of Itikawa demonstrates the importance of coupling between the p and f photoelectron waves at higher photon energy.

A. INTRODUCTION

The measurement of photoelectron angular distributions for selected rotational transitions of molecules should be a valuable probe of the dynamics of the photoionization process as well as a very sensitive test of the theoretical description of the behavior of photoelectrons in the continuum. The only case for which this measurement is feasible with present experimental techniques is the photoionization of the hydrogen molecule

$$H_2\ (X^1\Sigma_g^+,\ v'',\ J'') + h\nu \rightarrow H_2^+\ (X^2\Sigma_g^+,\ v',\ J') + e^-\ (E_k,\ \ell) \quad . \qquad (1)$$

In the photoelectron spectrum of H_2 the rotational structure of each vibrational band can be partially resolved if the experimental arrangement allows the energy resolution to be on the order of 10 meV. The rotational selection rules for this process were shown to be $J'=J''$ (Q branch) and $J'=J''\pm 2$ (S and O branches) by Sichel [1], by Dixon, et al. [2], and by Dill [3]. The photoelectron asymmetry parameter β, which characterizes the angular distribution, is defined by the expression for the differential cross section in the electric dipole approximation

$$\frac{d\sigma}{d\Omega} = \frac{\sigma}{4\pi}\quad 1 - \frac{\beta}{4}\,(3\cos^2\theta - 1) \qquad (2)$$

where the light is assumed to be unpolarized, and θ is the angle between the photon propagation vector and the direction of electron collection. β has been determined theoretically for specific

rotational transitions by Dill [3], by Ritchie and Tambe [4], by Chandra [5], and by Itikawa [6-8]. The essential conclusions to be drawn from these calculations are 1) that $\beta_Q(J'=J')$ has a value close to 2.0 and is rather insensitive to which theoretical method is used, and 2) that $\beta_S(J'=J''\pm 2)$ has a value much less than 2.0 and depends strongly on the method of coupling the $p(\ell=1)$ and $f(\ell=3)$ photoelectron partial waves.

Rotationally-resolved photoelectron spectra of H_2 have been observed by Åsbrink [9], by Niehaus and Ruf [10], and by Pollard, et al. [11]. In accordance with the selection rules, the predominant rotational transition is observed to be the Q branch, with the S branch intensity being lower by at least a factor of 10. Niehaus and Ruf [10] made the only previous angular distribution measurement for specific rotational transitions, reporting values for the asymmetry parameters of $\beta_Q = 1.95 \pm 0.03$ and $\beta_S = 0.85 \pm 0.14$ for H_2^+ $(v'=1)$ at $\lambda=736$Å. Chang [12] has questioned the method used by Niehaus and Ruf in the analysis of their data and has published revised values of $\beta_Q = 1.95 \pm 0.01$ and $\beta_S = 0.45 \pm 0.87$ based on his re-analysis.

In this letter we report values for β_S at 584Å and 736Å for H_2^+ $(v'=0)$, measured with a high resolution photoelectron spectrometer which uses a collimated supersonic beam of hydrogen to remove Doppler broadening. The results provide evidence for the importance of coupling between the p and f waves at the higher photon energy.

B. EXPERIMENTAL

The apparatus has been described in detail elsewhere [13]. A supersonic beam of n-H_2 (99.999% purity) was expanded through a 70-μm-diam nozzle at a stagnation pressure of 200 Torr and temperature of 77K, and was crossed with the photon beam from a resonance lamp operating at the HeIα (584Å, 21.22 eV) and NeIα (736Å, 16.85 eV) lines. The electron kinetic energy spectra were measured with an analyzer consisting of a double electrostatic deflector with multi-channel detection. The analyzer was operated at a resolution of 11 meV FWHM (for Ar) and an angular acceptance of ±1.8° (assuming a point source). The angular distributions were measured by orienting the unpolarized photon beam at two angles with respect to the analyzer, which remained in a fixed position. One lamp was placed so that the photon beam was orthogonal to both the molecular beam axis and the direction of electron collection. A second lamp was oriented such that the photon beam was at an angle of approximately 53° with respect to both the molecular beam axis and the direction of electron collection. The experiment consisted of measuring the Q-to-S branch intensity ratio for H_2^+ (v'=0) at the two angles. The spectra were accumulated by taking a series of 1-hour-long scans of the v'=0 transition (2-3 scans at 90° and 10-11 scans at 53°) and summing the scans together after shifting the peaks as necessary to account for the drift in the kinetic energy offset. The angle of the off-normal lamp was subsequently measured to be 52.6° ± 1°.

C. RESULTS AND DISCUSSION

The complete spectrum of n-H_2 recorded with the 90° lamp under the conditions used in the present angular distribution study is shown in Fig. 1. The hydrogen molecules in the beam consist of a 1:3 mixture of the J"=0 and J"=1 rotational states with the fraction of J"=2 less than 0.5%, so that the Q branch has contributions from the (J'=0 ← J"=0) and (J'=1 ← J"=1) components and the S branch has contributions from (J'=2 ← J"=0) and (J'=3 ← J"=1). The simplification of the rotational structure achieved by running at 77K is advantageous for the purpose of determining the Q-to-S branch intensity ratio.

The areas of the rotational components of the v'=0 transition were determined by least-squares fitting using an empirically-derived line-shape function as we have described elsewhere [11]. The spectra at 584Å and 736Å at the two angular geometries are shown in Figs. 2 and 3. The background is higher for the 53° spectra than for the 90° spectra, because the 53° photons strike the inside of the vacuum chamber (after crossing the molecular beam) at a point which is undesirably close to the entrance aperture of the analyzer. This background is especially bad at 736Å where the v'=0 peak is at a low kinetic energy (1.4 eV). The Q-to-S intensity ratios are listed in Table I. To obtain the asymmetry parameters we use the formula for the differential cross section given in Eq. 2. Putting in the values $\theta = 90°$ and $\theta = 52.6° \pm 1°$ we obtain an expression for the ratio of the photoelectron intensities at the two angles,

$$I_{90}/I_{53} = (1 + \beta/4)/(1 + \epsilon\beta/4) \tag{3}$$

where ϵ would equal zero if the off-normal lamp were at $\theta = 54.7°$ but in the present case has the value $\epsilon = -0.104 \pm 0.050$. Eq. 3 leads to the expression relating the intensity ratios at the two angles to the Q and S branch asymmetry parameters,

$$\left(\frac{I_{90}(Q)}{I_{90}(S)}\right)\left(\frac{I_{53}(S)}{I_{53}(Q)}\right) = \left(\frac{1+\beta_Q/4}{1+\epsilon\beta_Q/4}\right)\left(\frac{1+\epsilon\beta_S/4}{1+\beta_S/4}\right) \quad . \tag{4}$$

Although we apparently cannot determine β_Q and β_S independently based on the present data, it is possible to make a reasonable estimate of the value of β_Q and thereby obtain a value for the more interesting quantity β_S. For the ($J'=0 \leftarrow J''=0$) transition, which contributes 25% of the intensity to the Q branch, Dill [3] and Itikawa [6] have shown that β equals 2.0 for all v-states. The ($J'=1 \leftarrow J''=1$) transition, which contributes the remaining 75%, has been predicted to have a β close to 1.9 by Itikawa [8] for both 584Å and 736Å. The previous experimental value of $\beta_Q(v'=1,\ 736Å) = 1.95$ [10,12] is consistent with our expectations from theory. We have adopted the value $\beta_Q(v'=0) = 1.90 \pm 0.10$ and used it to calculate β_S for both photon energies.

There is a rather wide variation represented in the available experimental and theoretical values for β_S which are listed in Table II. The present result at 584Å is the only experimental value available, and it is in good agreement with the theoretical value calculated by Itikawa [8] using coupled p and f partial waves. Our value at 736Å is the lowest of any tabulated and is actually in better agreement with

the theories which do not include the f wave. Nevertheless, the substantial increase in β_S as the photoelectron energy varies from 1.4 eV (at 736Å) to 5.8 eV (at 584Å) is well represented by Itikawa's coupled wave β-values. The source of the increase is clearly the enhancement of the f wave at the higher energy, because the effect is not predicted by the theories that use only the p wave.

The fact that our measured β_S is less than the predicted values at 736Å is conceivably a consequence of autoionization, which is not included in the theory. This effect was investigated by Raoult and Jungen [14] who calculated rotationally averaged β-values for H_2 from 790Å to 760Å, a spectral region with many strongly autoionizing transitions. The asymmetry parameter for each v-state undergoes large oscillations at resonances near the corresponding vibrational threshold, but the effect is largely damped out for v'=0 at wavelengths of 760Å or less. These authors also showed that the rotational branching ratio shifts dramatically at the resonances from the J'=J" channel to the J'=J"±2 channel. We can use our measured intensities and β-values to determine this branching ratio with the results: $\sigma(S)/\sigma(Q) = 0.095 \pm 0.004$ (at 584Å) and 0.061 ± 0.002 (at 736Å). Clearly, at 736Å for the v'=0 channel there is no large resonance of the type considered by Raoult and Jungen, for which we would observe $\sigma(S)/\sigma(Q)$ to be much greater than 0.1. The high resolution photoionization spectrum of H_2 by Dehmer and Chupka [15] exhibits some weak structure near 736Å but does not provide evidence for a major effect from autoionization. Berkowitz [16] also examined the photoionization spectrum in this region and

reached the same conclusion. We should note that the present rotational branching ratios are significantly smaller than are predicted by Itikawa [8], whose theoretical cross sections lead to the values of $\sigma(S)/\sigma(Q) = 0.157$ (at 584Å) and 0.139 (at 736Å) for a 1:3 mixture of $H_2(J''=0)$ and $H_2(J''=1)$.

The possibility exists that a systematic error could be present in our results due to a partial alignment of the rotational angular momentum vectors induced by the supersonic expansion. Such an alignment was observed in the case of sodium dimer, Na_2, by Sinha, Caldwell, and Zare [17]. These authors proposed a classical model to explain the effect, based on the exchange of angular momentum in an inelastic collision between a hard ellipsoid (the dimer) and a hard sphere (the monomer). We believe that there is no appreciable alignment in our hydrogen beam for at least two reasons. First, the hydrogen molecule is somewhat more spherical in shape that the sodium dimer, which means that collisions are less effective in causing alignment. Second, the rotational levels of hydrogen at 77K are almost fully relaxed behind the nozzle, so that there are few rotationally-inelastic collisions during the expansion.

D. CONCLUSION

We have measured the photoelectron asymmetry parameter for the S branch of $H_2^+(v'=0)$ with the results: $\beta_S(584Å) = 0.87 \pm 0.19$ and $\beta_S(736Å) = 0.08 \pm 0.15$. The trend toward higher β_S with increasing photon energy is well accounted for by the theory of Itikawa [8], and is a manifestation of coupling between the p and f photoelectron waves.

REFERENCES

* This chapter (LBL-13998) was submitted to Chemical Physics Letters for publication.

1. J. M. Sichel, Mol. Phys. 18 (1970) 95.
2. R. N. Dixon, G. Duxbury, M. Horani, and J. Rostas, Mol. Phys. 22 (1971) 977.
3. D. Dill, Phys. Rev. A 6 (1972) 160.
4. B. Ritchie and B. R. Tambe, J. Chem. Phys. 68 (1978) 755.
5. N. Chandra, in: Abstracts of Papers, 10th Intern. Conf. Phys. Electron Atom. Coll. (Commisariat a l'Energie Atomique, Paris, 1977) p. 1210.
6. Y. Itikawa, Chem. Phys. 28 (1978) 461.
7. Y. Itikawa, Chem. Phys. 30 (1978) 109.
8. Y. Itikawa, Chem. Phys. 37 (1979) 401.
9. L. Åsbrink, Chem. Phys. Lett. 7 (1970) 549.
10. A. Niehaus and M. W. Ruf, Chem. Phys. Lett. 11 (1971) 55.
11. J. E. Pollard, D. J. Trevor, J. E. Reutt, Y. T. Lee, and D. A. Shirley, J. Chem. Phys. (in press); and this thesis, Chapter III.
12. E. S. Chang, J. Phys. B: Atom. Molec. Phys. 11 (1978) L69.
13. J. E. Pollard, D. J. Trevor, Y. T. Lee, and D. A. Shirley, Rev. Sci. Instrum. 52 (1981) 1837; and this thesis, Chapter II.
14. M. Raoult and Ch. Jungen, J. Chem. Phys. 74 (1981) 3388.
15. P. M. Dehmer and W. A. Chupka, J. Chem. Phys. 65 (1976) 2243.

16. J. Berkowitz, Photoabsorption, Photoionization, and Photoelectron Spectroscopy (Academic Press, New York, 1979) p. 189.

17. M. P. Sinha, C. D. Caldwell, and R. N. Zare, J. Chem. Phys. 61 (1974) 491.

Table I. Intensity ratios for H_2^+ (v'=0). Stated error limits are statistical uncertainties ($\pm\sigma$) from the least-squares peak fitting.

	584Å	736Å
$I_{90}(Q)/I_{90}(S)$	12.79 ± 0.21	23.59 ± 0.29
$I_{53}(Q)/I_{53}(S)$	10.26 ± 0.24	15.55 ± 0.32

Table II. S branch asymmetry parameters, β_S, for H_2^+ (v'=0).

	584Å	736Å
Experiment:		
Present results	0.87 ± 0.19	0.08 ± 0.15
Niehaus and Ruf (v'=1)[a]		0.85 ± 0.14
Chang (v'=1)[b]		0.45 ± 0.87
Theory:		
Dill (direct PI)[c]	0.2	0.2
Ritchie and Tambe[d]	1.215	0.740
Chandra[e]		0.20 - 0.38
Itikawa (p wave)[f]	0.2338	0.2069
Itikawa (p+f waves)[f]	0.7494	0.3484

[a]A. Niehaus and M. W. Ruf, Chem. Phys. Lett. 11 (1971) 55.

[b]E. S. Chang, J. Phys. B: Atom. Molec. Phys. 11 (1978) L69.

[c]D. Dill, Phys. Rev. A 6 (1972) 160.

[d]B. Ritchie and B. R. Tambe, J. Chem. Phys. 68 (1978) 755.

[e]N. Chandra, in: Abstracts of Papers, 10th Intern. Conf. Phys. Electron Atom. Coll. (Commisariat a l'Energie Atomique, Paris, 1977) p. 1210.

[f]Y. Itikawa, Chem. Phys. 37 (1979) 401.

FIGURE CAPTIONS

Fig. 1. The 584Å photoelectron spectrum of n-H_2 expanded from 200 Torr at 77K.

Fig. 2. The $H_2^+(v'=0)$ transition at 584Å for two angular geometries. The curve is the least-squares fit, and the points are the data minus the fit (shifted upward for visibility.)

Fig. 3. The $H_2^+(v'=0)$ transition at 736Å for two angular geometries. The curve is the least squares fit, and the points are the data minus the fit (shifted upward for visibility.)

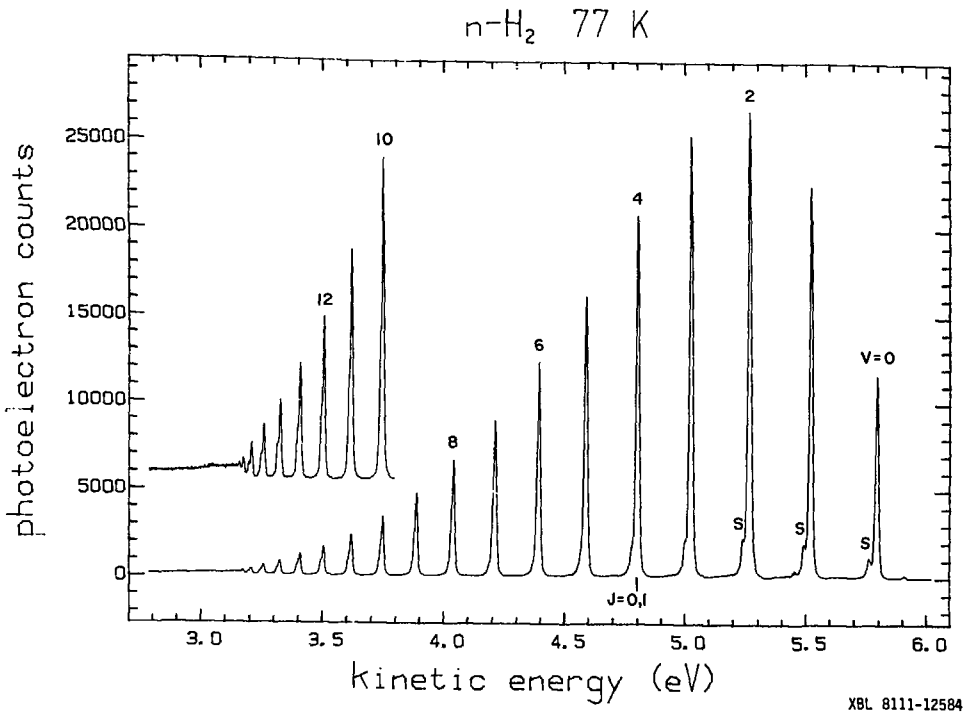
n-H2 77 K
photoelectron counts
25000
20000
15000
10000
5000
0
3.0
3.5
4.0
4.5
5.0
5.5
6.0
kinetic energy (eV)
12
10
8
6
4
2
V=0
S
S
S
J=0,1
XBL 8111-12584

Figure 1

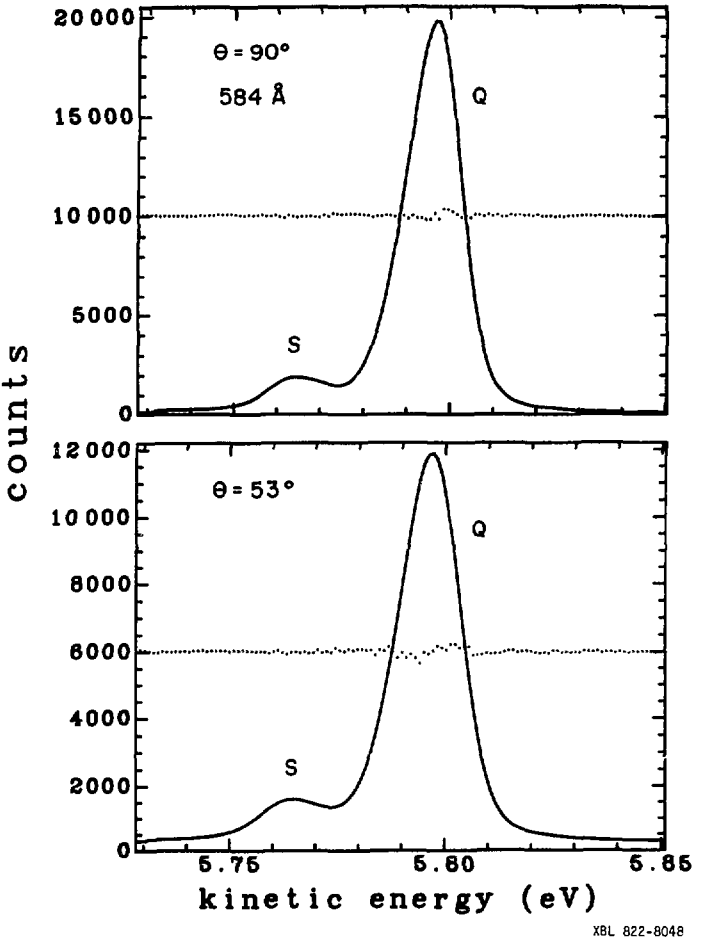
20 000
15 000
10 000
5000
0
θ = 90°
584 Å
Q
S
counts
12 000
10 000
8000
6000
4000
2000
0
θ = 53°
Q
S
5.75
5.80
5.85
kinetic energy (eV)
XBL 822-8048

Figure 2

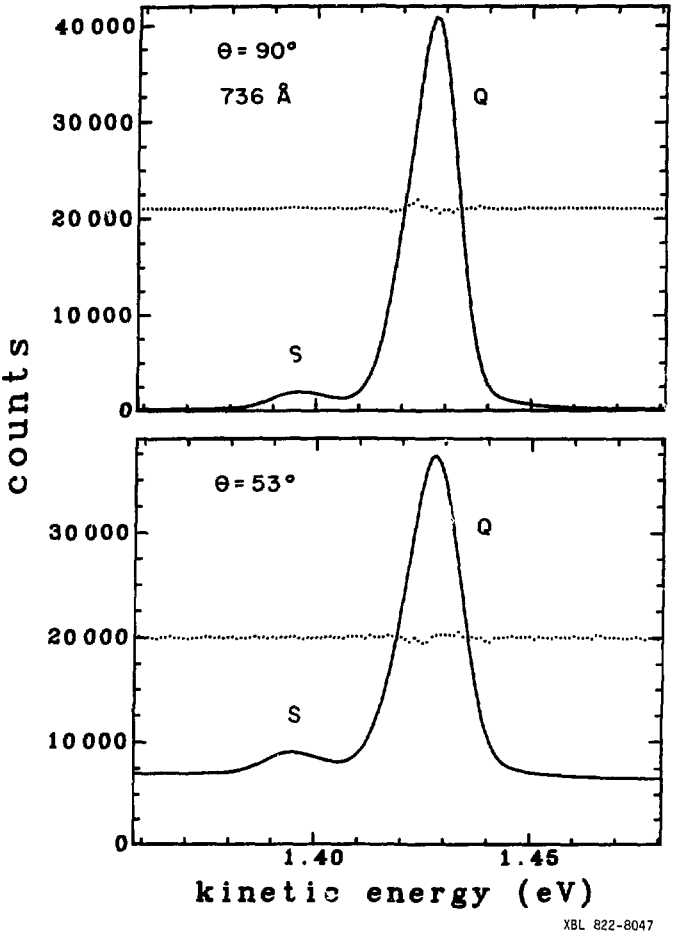
40 000
30 000
20 000
10 000
0
θ = 90°
736 Å
Q
S
counts
θ = 53°
30 000
20 000
10 000
0
Q
S
1.40
1.45
kinetic energy (eV)
XBL 822-8047

Figure 3

V. ROTATIONAL RELAXATION IN SUPERSONIC BEAMS OF HYDROGEN BY HIGH RESOLUTION PHOTOELECTRON SPECTROSCOPY*

ABSTRACT

The rotational relaxation of n-H_2, p-H_2, HD, and n-D_2 in a free jet expansion was studied by means of rotationally-resolved photoelectron spectroscopy using a collimated supersonic molecular beam. Rotational state distributions were determined from the relative intensities of the Q branch rotational components for a wide range of stagnation pressures with nozzle temperatures from 300K to 700K. Significant deviations from a Boltzmann distribution were observed for those cases where the degree of rotational relaxation was substantial. HD was found to relax after undergoing only one-tenth of the number of collisions required to relax H_2 or D_2. The relaxation of p-H_2 was modeled using the state-to-state rate constants method of Rabitz and Lam, which was shown to be quite effective in accounting for the experimentally observed population distributions.

A. INTRODUCTION

A free jet expansion constitutes a system in which the internal degrees of freedom of the molecules are initially in contact with a rapidly cooling translational bath. In the early (collisional) part of the expansion the internal modes can relax by transferring energy into translation until the point at which collisions become very infrequent, and communication with the bath is cut off. The details of this relaxation process can be elucidated by measuring the rotational and vibrational state distributions of the molecules in the beam as a function of the stagnation conditions. Such experiments have been performed for a number of molecular systems using a variety of spectroscopic techniques.[1] We have recently succeeded in obtaining rotationally-resolved photoelectron spectra from supersonic beams of hydrogen,[2] and the present investigation is an extension of this technique to the study of rotational relaxation in supersonic expansions.

Hydrogen is in several respects an unusual system. The very large rotational energy spacings allow only a few levels to be thermally populated at room temperature. Vibrational excitation is negligible for H_2 below 1000K. The large rotational energy gaps and the small anisotropy of the interaction potential mean that R-T energy transfer is inefficient compared to heavier molecules. In addition the various isotopic species of hydrogen should exhibit substantially different relaxation behavior because of the variation in the spacings of the rotational energy levels and in the separation between the center of

mass and the center of the charge distribution. Finally, for H_2 and D_2 the lack of conversion between the ortho and para forms will lead to large deviations from a Boltzmann distribution of rotational states for high Mach number expansions.

There have been several previous experimental investigations of rotational relaxation in beams of hydrogen. Gallagher and Fenn[3] measured time-of-flight velocity distributions for n-H_2 at stagnation temperatures from 300K to 1900K and used the energy balance criterion to derive rotational temperatures and collision numbers. They found that the rotational collision number increases from 300 to 500 over this temperature range. Buck et al.[4] performed time-of-flight measurements on HD, n-D_2, and o-D_2 with stagnation temperatures of 300K or below and assumed a Boltzmann rotational distribution to derive the state populations. Verberne, et al.[5] used molecular beam magnetic resonance to measure the populations of n-H_2 with stagnation temperatures from 300K to 1000K and found that the distribution could not be characterized by a unique rotational temperature. Godfried, et al.[6] used Raman scattering to measure the number density and populations in free jets of n-H_2 and n-D_2 with a stagnation temperature of 293K. They compared their results with the predictions of a model which treats the time evolution of the state populations and uses a single rotational collision number. They also reported an axial density profile for n-H_2 which corresponds to that expected for a monatomic ($C_p/C_v = 1.67$) expansion. Huber-Wälchli and Nibeler[7] measured CARS spectra of n-H_2 and n-D_2 in free jets with a 300K stagnation

temperature. They analyzed their data in terms of a single rotational temperature which served as an input parameter in their CARS spectral simulation. The minimum number density required for Raman or CARS experiments on hydrogen is approximately 10^{16} cm^{-3}, so that it is necessary to use an unskimmed free jet. The present measurements employ a collimated molecular beam which more closely approximates the experimental arrangement common to crossed beam scattering studies. The number density ranges from about 10^{11} to 10^{13} cm^{-3}. We report level populations for fully expanded jets of n-H_2 and n-D_2 over a wider range of stagnation conditions than have been reported previously, and we also extend the population measurements to p-H_2 and HD for the first time. We observe departures from a Boltzmann distribution for strong expansions. The results for p-H_2 are analyzed in terms of the theoretical framework of Rabitz and Lam,[8] which uses a set of state-to-state rate constants and combines the master kinetic equations with the equations of fluid mechanics.

B. EXPERIMENTAL

The photoelectron spectrometer used in this work was described in detail in an earlier publication.[9] The electron energy analyzer was a double electrostatic deflector with multichannel detection and was operated at a resolution of 11 meV FWHM (for Ar) with HeIα (584Å, 21.217 eV) light. Photoelectrons were sampled at an angle of 90° with respect to the photon beam. Two beam source configurations were used: (1) a 70-μm-diam nozzle located 6.4 mm from the tip of a

0.66-mm-diam X 6.4-mm-tall conical skimmer, and (2) a 40-μm-diam nozzle located 9.6 mm from the tip of a 0.66-mm-diam X 12.7-mm-tall conical skimmer. The photon beam crossed the molecular beam at 32 mm downstream from the nozzle in configuration (1) and at 41 mm downstream from the nozzle in configuration (2). The nozzles were made from molybdenum electron microscope apertures, and were of the converging type. The pressure in the beam source exhaust chamber was typically less than 5×10^{-4} torr, and in the main chamber the pressure was less than 2×10^{-5} torr. The nozzle could be heated to a maximum of 700K with a coil of non-inductively-wound two-wire Semflex heater cable (Semco, Inc.). Some care was necessary when running at high temperature, because the electron kinetic energy offset drifted rapidly as surfaces near the ionization region warmed up. For this reason the scan time was usually restricted to 30 minutes or less when running with the heated nozzle. The samples and other experimental details were the same as we used in our previous work on hydrogen.[2]

Rotational populations were determined from the relative intensities of the Q branch components for a selected vibrational state of the molecular ion. The Q branch can be more fully resolved for the higher v-states, until the point at which the adjacent vibrational transitions begin to overlap. The optimal v-states for this experiment were $H_2^+(v'=5)$, $HD^+(v'=7)$, and $D_2^+(v'=8)$. The areas of the rotational components were calculated by least-squares fitting of the spectra using an empirically derived lineshape function which we have described previously.[2] Standard deviations from the least-squares

fits were generally in the range of 1-3% of the area of a given rotational component, although for those cases where the population of the state was less than 1%, the standard deviation was about 10-20% of the area. The S branch was also included in the fit and contributed about 4% of the total area for H_2 and about 2% for HD and D_2. To convert the photoelectron intensities measured at the present 90° angular geometry to rotational populations it is necessary to consider the rotational dependence of the cross section, σ_J, and the photoelectron asymmetry parameter, β_J. The observed intensity of a given Q branch transition is proportional to the product of the rotational level population and the factor $\sigma_J(1 + \beta_J/4)$. Itikawa[10] has given theoretical values of σ_J and β_J at λ=584Å for $H_2^+(v'=5)$ which indicate that the corrections necessary for obtaining the rotational population from the photoelectron intensities measured at 90° are less than 1-2% of the intensity of each rotational component. An approximate experimental verification of Itikawa's cross sections has been reported by Morioka, et al.[11] In order to judge whether a correction is warranted for the present data, we have compared our measured intensities at 297K and 25 torr stagnation conditions (70 μm nozzle) with the populations derived from a Boltzmann distribution, assuming a 3:1 ortho-para ratio for n-H_2 and 2:1 ortho-para ratio for n-D_2. For n-H_2, p-H_2, and n-D_2 the results agreed with a Boltzmann distribution to within the statistical uncertainty of the data, although for HD a systematic deviation was noted because the rotational distribution had relaxed to some extent even at the lowest pressure. Thus we have applied no correction for the

rotational dependence of σ_J and β_J and have used the Q branch intensities directly to determine the populations.

Figure 1 shows a series of spectra which are typical of the data obtained in this experiment. The $H_2^+(v'=5)$ transition from n-H_2 at 696K is shown for several stagnation pressures for which the rotational relaxation is particularly dramatic.

Table I lists the rotational energies and degeneracies which were used in the analysis of the rotational population data.

C. RESULTS

1. n-H_2 and n-D_2

The rotational populations measured for n-H_2 and n-D_2 expanded from 297K through the 70 μm nozzle are shown in Fig. 2 as a function of pd, the product of the stagnation pressure (p) and the nozzle diameter (d). At the lowest observed pd there is only a slight relaxation of the rotational energy, and the populations are very close to those expected for a Boltzmann distribution at 297K. As pd is increased the levels relax, but the populations cannot generally be described by a unique Boltzmann temperature. This is demonstrated in Fig. 3, which shows $\ln(n_J/g_J)$ vs. E_J at two nozzle temperatures for n-H_2 and n-D_2. These plots would be linear if there were a unique rotational temperature, but in fact a positive curvature is observed in each case. The R-T energy transfer is therefore less efficient for the higher rotational levels, which is in accord with the fact that the energy gaps

are higher for these states. Another way of visualizing the non-Boltzmann nature of the population distributions is to use the two-level temperature relative to the J=0 level, T_{J0}, which is defined by

$$n_J/n_0 = (g_J/g_0) \exp(-E_J/kT_{J0}) \tag{1}$$

T_{J0} is shown in Fig. 4 for the same data sets that were presented as Boltzmann-type plots in Fig. 3, and it is apparent that T_{J0} increases appreciably with increasing J.

The average rotational energy is a well defined quantity in all cases and is given by $E = \sum_J n_J E_J$. We wish to correlate the measured rotational energy with a parameter that includes the effects of the three variables investigated in this work -- the stagnation pressure, temperature, and nozzle diameter. The inverse Knudsen number, $(Kn_0)^{-1}$, is an appropriate scaling parameter for this purpose. $(Kn_0)^{-1}$ is the ratio of the nozzle diameter, d, to the mean free path, Λ_0, and is given by

$$\begin{aligned}(Kn_0)^{-1} &= d/\Lambda_0 = \sqrt{2}\,\pi\, a^2\, p\, d\, /\, k\, T \\ &= 36800 \times p(\text{torr}) \times d(\text{cm})\, /\, T(K)\end{aligned} \tag{2}$$

where a = 2.93Å is the gas kinetic collision diameter (from Gallagher and Fenn[3]). $(Kn_0)^{-1}$ is very roughly the number of collisions that a molecule undergoes in the expansion. Figs. 5 and 6 show the results of plotting the fraction of retained rotational energy, $(E - E_0)/(E_T - E_0)$, against the inverse Knudsen number for n-H_2 and n-D_2. E_T and E_0 are the rotational energy at the stagnation temperature and at zero K, respectively (assuming no ortho-para conversion). These plots are seen to be fairly successful in correlating the final rotational energy with the stagnation conditions, although some systematic deviations are noted. With the exception of the results for n-H_2 at 297K, the data points corresponding to the 70 μm nozzle have higher rotational energy than those for the 40 μm nozzle at the same $(Kn_0)^{-1}$. A likely source of this difference is the skimmer interference, which we expect to be less important for the configuration used with the 40 μm nozzle (described in Section B). Using $(Kn_0)^{-1}$ as the scaling parameter does not take into account the variation of the rotational collision number with temperature. The data for n-H_2 in the high $(Kn_0)^{-1}$ region are consistent with the observation of Gallagher and Fenn[3] that the rotational collision number increases slightly over our temperature range. The data for n-D_2 do not exemplify this trend however. A difficulty which applies only to D_2 is that the rotational levels above J=6 are not observed, because they overlap with the next vibrational state. Although these levels contribute only about 4% of the total intensity

even at 694K, the fraction of the rotational energy residing in these states is about 0.5% at 297K, 5% at 475K, and 15% at 694K.

Before leaving n-H_2 and n-D_2 we list in Table II the rotational populations for each data set at the pressure for which the relaxation was most complete. In general we observed that the intensity of the beam was reduced and the rotational energy of the beam was increased for pressures higher than those listed, due to collisions with the background gas molecules in the region between the nozzle and the skimmer. It will be noted that the ortho-para ratios exhibit some variation around the expected values of 3:1 for H_2 and 2:1 for D_2. This is attributed to error arising from the deconvolution of the J=0 and J=1 transitions which are not resolved in the spectra. We generally obtained the correct ortho-para ratio for the less fully relaxed cases where the intensity is spread out over several well-resolved transitions.

2. HD

The rotational populations of HD as a function of pd are shown in Fig. 7 for the case of the 70 μm nozzle at 297K. High temperature scans for HD were not feasible because the sample was found to convert to a mixture of HD, H_2, and D_2 when the nozzle was heated. The populations measured at the lowest pd in Fig. 7 have relaxed somewhat from the initial thermal distribution, even though H_2 and D_2 do not show any relaxation under these conditions. The departure from a Boltzmann distribution is also more pronounced for HD, as is seen in

Fig. 8 which shows $\ln(n_J/g_J)$ vs. E_J at several stagnation pressures. We again observe positive curvature in these plots, showing that the relaxation is least effective for the highest rotational levels. Figure 9 shows the rotational energy as a function of $(Kn_0)^{-1}$, comparing the results for HD and p-H_2. These molecules are alike in the sense that both would have a rotational energy of zero at zero K, so that there are no complications from an "ortho-para" effect. The major difference between them is that the rotational constant is effectively four times larger for p-H_2 than for HD. The result of this difference in energy gaps is reflected in Fig. 9, which shows that to remove half of the rotational energy ten times as many collisions are needed for p-H_2 as for HD. The relaxation of HD is also facilitated by the fact that it rotates about a center of mass which is displaced from the geometrical center of the molecule. This additional anisotropy in the interaction potential for HD leads to a larger rotational relaxation cross section than is found for the homonuclear species.

3. Modeling the relaxation of p-H_2

Rabitz and Lam[8] have given a theoretical method for simulating the rotational relaxation of hydrogen in a free jet expansion, which we have applied to p-H_2 to gain a better understanding of the present observations. This model starts with the theoretical rotational energy transfer cross sections of Zarur and Rabitz,[12] which were calculated using an effective potential formalism. State-to-state energy transfer rate constants are determined for a given translational temperature by

integrating the energy dependence of the cross section over a Maxwell-Boltzmann velocity distribution. The rate constants are used in the master equations of kinetics, which are coupled to the fluid mechanical equations appropriate to a one-dimensional uniform flow under steady-state conditions (Ref. 8, Eq. 25). The unknowns in this set of first order differential equations are: $P_i(x)$, the population of state i; $T(x)$, the translational temperature; $v(x)$, the flow velocity; $p(x)$, the local pressure; and $\rho(x)$, the number density. x is the distance along the flow from the orifice, which is assumed to be thin or at least rapidly converging. Following Rabitz and Lam we have assumed the Ashkenas-Sherman[13] formula (with either two or three terms) for the Mach number at x greater than x*, and an exponential form at x less than x* (Ref. 8, Eqs. 37,38). The parameter x* is typically chosen to be equal to one nozzle diameter. $\rho(x)$ can be calculated from the isentropic equation relating it to the Mach number,

$$\rho(x) = \rho_0 \left(1 + (1/2)(\gamma - 1)\, M(x)^2\right)^{1/(1-\gamma)} \tag{3}$$

where ρ_0 is the stagnation number density, $M(x)$ is the Mach number, and $\gamma = C_p/C_v$. With this assumed form for $\rho(x)$, one of the equations in the set can be eliminated, and the remaining equations can be manipulated into the following new set which is convenient for numerical integration,

$$\frac{dP_i}{dx} = \frac{\rho}{v} \sum_j \sum_\ell \sum_{m \geq \ell} \Big(- P_i P_j k(ij\ell m;T) + P_\ell P_m k(\ell m ij;T) \Big)\, G(ij\ell m) \tag{4a}$$

$$\frac{dT}{dx} = \frac{2}{3} T \left(\frac{1}{\rho} \frac{d\rho}{dx} - \frac{1}{kT} \sum_i \epsilon_i \frac{dP_i}{dx} \right) \tag{4b}$$

$$\frac{dv}{dx} = - \frac{1}{m_o v} \left(\frac{5}{2} k \frac{dT}{dx} + \sum_i \epsilon_i \frac{dP_i}{dx} \right) \tag{4c}$$

$$\frac{dp}{dx} = - \rho \, m_o v \frac{dv}{dx} \tag{4d}$$

where $G(ij\ell m)$ is a symmetry factor, ϵ_i is the rotational energy of state i, m_o is the mass of H_2, and $k(ij\ell m;T)$ is the rate constant for the process,

$$H_2(i) + H_2(j) \rightarrow H_2(\ell) + H_2(m) \tag{5}$$

The rate constants must be recalculated for the new T(x) at each step in the integration. To make this more convenient we used a cubic least-squares fit to the cross sections, $\sigma(ij\ell m;E)$ vs. E in Table V of Ref. 12, so that the necessary integrals over the velocity distribution could be evaluated analytically. It should be noted that only the low kinetic energy region (E_k less than 0.3 eV) is of importance when calculating $k(ij\ell m;T)$ for T less than 300K. Eqs. (4) were integrated with a fourth-order Runge-Kutta routine for $-4 \leq (x/d) \leq +4$, for a range of initial values which included the starting conditions used in the present measurements. These calculations included the rotational levels of p-H_2 with J=0, 2, and 4.

Fig. 10 shows the rotational populations of p-H_2 measured with the 70 μm nozzle at 297K, together with the calculated curve. In Fig. 9

the calculated curve for the rotational energy as a function of $(Kn_0)^{-1}$ appears with the experimental points for p-H_2. The comparison between theory and experiment is somewhat clouded by the uncertainty in the assumed form of $\rho(x)$ in Eq. 3. The adjustable parameters at our disposal are γ, x^*, and the number of terms in the Ashkenas-Sherman formula (either two or three). The heat capacity ratio appropriate to this problem is likely to lie somewhere between the monatomic ($\gamma = 1.67$) and the diatomic ($\gamma = 1.40$) values. Rather surprisingly, the number density measurements of Godfried, et al.[6] for pd = 300 torr-mm suggest that the monatomic value is the correct one for n-H_2 at $x/d > 1$. It will be seen below that the rotational relaxation is essentially confined to the region where $x/d < 1.5$, for which the Ashkenas-Sherman formula may not be correct. Therefore the choice of x^*, which is the point where the exponential extrapolation to smaller x begins, is expected to have an appreciable effect on the results. Because of the importance of the small x region, it seems advisable to use the three term formula for M(x) (which is valid down to $x/d = 1.0$, according to Ref. 13) rather than the two-term formula which was adopted by Rabitz and Lam. The calculated curves in Figs. 9 and 10 were generated by using $\gamma = 1.40$ and $x^*/d = 0.8$ with the three-term formula for M(x). The rotational energy curve in Fig. 9 shifts downward for larger values of γ or x^*, yielding poorer agreement with experiment. The curve shifts upward if the two-term formula is used, yielding somewhat better agreement with experiment. The model of Rabitz and Lam is thus seen to be a fairly realistic one, but the remaining uncertainty about $\rho(x)$ seems

to preclude a more definitive test of the correctness of the rotational energy transfer cross sections.

A very valuable aspect of this model is the detailed picture that it gives of the dynamics of the free jet expansion. As an example of this we show in Fig. 11 the populations $P_0(x)$, $P_2(x)$, and $P_4(x)$, and the values of $\rho(x)$, $T(x)$, $v(x)$, and $p(x)$ calculated for a stagnation pressure of 1600 torr. It can be seen that the rotational populations have approached their asymptotic values for $x/d \approx 1.5$, at which point the temperature is about 65K and the Mach number is about 3. The temperature actually continues to cool until much further downstream, and the Mach number reaches a terminal value estimated to be between 10 and 20 (cf. Ref. 4). Rotational relaxation ceases for x/d greater than 1.5 primarily because the energy transfer rate constants have dropped by several orders of magnitude from their room temperature values (see Ref. 8, Fig. 1). In this model the temperature profile, $T(x)$, is nearly independent of the stagnation pressure. Thus the effect of increasing the pressure is simply to increase the number of collisions that occur before the temperature is too low for R-T energy transfer. This point is reached at $x/d \approx 1.5$ for all stagnation pressures.

We have shown that the theoretical approach of Rabitz and Lam can give a rather good account of the rotational relaxation in a free jet of $p\text{-}H_2$. It would be of interest to apply this method to HD if the necessary cross sections become available, to see how well it predicts the much more facile relaxation that we have observed for this system.

REFERENCES

* This chapter (LBL-14279) was submitted to the Journal of Chemical Physics for publication.

1. D. Bassi, A. Boschetti, S. Marchetti, G. Scoles, and M. Zen, J. Chem. Phys., 74, 2221 (1981); and references cited therein.
2. J. E. Pollard, D. J. Trevor, J. E. Reutt, Y. T. Lee, and D. A. Shirley, J. Chem. Phys. (in press); and this thesis, Chapter III.
3. R. J. Gallagher and J. B. Fenn, J. Chem. Phys., 60, 3487 (1974); and 60, 3492 (1974).
4. U. Buck, F. Huisken, J. Schleusener, and J. Schaefer, J. Chem. Phys., 74, 535 (1981); and J. Andres, U. Buck, F. Huisken, J. Schleusener, and F. Torello, J. Chem. Phys., 73, 5620 (1980).
5. J. Verberne, I. Ozier, L. Zandee, and J. Reuss, Mol. Phys., 35, 1649 (1978).
6. H. P. Godfried, I. F. Silvera, and J. Van Straaten, 12th International Symposium on Rarefied Gas Dynamics (Charlottesville, 1980) part 2, p. 772.
7. P. Huber-Walchli and J. W. Nibeler, J. Chem. Phys., 76, 273 (1982).
8. H. Rabitz and S.-H. Lam, J. Chem. Phys. 63, 3532 (1975).
9. J. E. Pollard, D. J. Trevor, Y. T. Lee, and D. A. Shirley, Rev. Sci. Instrum., 52, 1837 (1981); and this thesis, Chapter II.
10. Y. Itikawa, Chem. Phys., 30, 109 (1978).
11. Y. Morioka, S. Hara, and M. Nakamura, Phys. Rev. A, 22, 177 (1980).

12. G. Zarur and H. Rabitz, J. Chem. Phys., 60, 2057 (1974).

13. H. Ashkenas and F. S. Sherman, 4th International Symposium on *Rarefied Gas Dynamics* (Toronto, 1964) vol. 2, p. 84.

Table I. Rotational energies (in cm^{-1}) and degeneracies for the v=0 level in the ground electronic state of n-H_2, HD, and n-D_2.

	n-H_2		HD		n-D_2	
J	E_J	g_J	E_J	g_J	E_J	g_J
0	0.	1	0.	1	0.	6
1	118.49	9	89.24	3	59.77	9
2	354.37	5	267.09	5	179.04	30
3	705.51	21	532.36	7	357.26	21
4	1168.76	9	883.26	9	593.63	54
5	1740.09	33	1317.48	11	887.05	33
6	2414.74	13	1832.28	13	1236.18	78

Energies are derived from the rotational constants of K. P. Huber and G. Herzberg, Constants of Diatomic Molecules, Van Nostrand Reinhold, New York (1979).

Table 11 Rotational populations for n-H_2 and n-D_2. For a given nozzle diameter, d, and temperature, T, the populations are listed for the stagnation pressure, p, at which the most complete relaxation was observed.

	p(torr)	d(μm)	T(K)	J=0	J=1	J=2	J=3	J=4	J=5	J=6
H_2										
	1830	70	297	19.5	70.8	6.8	2.8	0.1		
	2350	70	480	14.2	59.0	12.3	12.8	0.8	0.9	
	11100	40	297	21.2	75.1	2.9	0.8			
	19000	40	492	19.4	69.6	7.3	3.7			
	32000	40	696	23.0	63.0	8.7	5.3			
D_2										
	1830	70	297	33.2	28.5	31.0	4.5	2.5	0.3	
	1420	70	475	18.6	19.9	34.6	12.0	11.2	1.9	1.8
	8600	40	297	46.2	31.8	19.8	1.3	0.9		
	24000	40	505	41.5	31.7	23.7	1.8	1.2	0.1	
	40000	40	694	34.3	31.8	2[illegible].2	3.6	2.0	0.1	

FIGURE CAPTIONS

Fig. 1. The v'=5 transition from n-H_2 expanded through a 40μm nozzle at 696K for several stagnation pressures. The transitions are labeled with the Q branch rotational quantum numbers.

Fig. 2. Rotational populations of n-H_2 and n-D_2 expanded through a 70μm nozzle at 297K.

Fig. 3. Boltzmann plot of the populations for n-H_2 and n-D_2 expanded through a 70μm nozzle at 1830 torr.

Fig. 4. Two - level temperatures, T_{J0}, for n-H_2 and n-D_2 expanded through a 70μm nozzle at 1830 torr.

Fig. 5. Fraction of retained rotational energy vs. inverse Knudsen number for n-H_2 with the nozzle diameters and stagnation temperatures indicated. E_T is the initial energy, and E_0 is the energy at zero K for a 3:1 ortho-para ratio (88.87 cm^{-1}).

Fig. 6. Fraction of retained rotational energy vs. inverse Knudsen number for n-D_2 with the nozzle diameters and stagnation temperatures indicated. E_T is the initial energy, and E_0 is the energy at zero K for a 2:1 ortho-para ratio (19.92 cm^{-1}).

Fig. 7. Rotational populations of HD expanded through a 70μm nozzle at 297K.

Fig. 8. Boltzmann plot of the populations for HD expanded through a 70μm nozzle at several stagnation pressures. The lines are

weighted least-squares fits to the data. They correspond to temperatures of 273K, 210K, 145K, and 99K, for 25, 100, 400, and 1830 torr, respectively.

Fig. 9. Fraction of retained rotational energy vs. inverse Knudsen number for p-H_2 and HD with a 70μm nozzle at 297K. The curve is the result of the calculation which is explained in the text.

Fig. 10. Rotational populations of p-H_2 expanded through a 70μm nozzle at 297K. The curves are the results of the calculation which is explained in the text.

Fig. 11. Model calculation of the p-H_2 expansion with a 70μm nozzle at 297K and 1600 torr stagnation pressure. x/d is the distance in nozzle diameters along the centerline from the orifice. The upper graph shows the populations of the J=0, 2, and 4 rotational states. The lower graph shows the number density ρ, the translational temperature T, the flow velocity v, and the local pressure p, all normalized to the same scale. This calculation uses the three-term Ashkenas-Sherman formula for the Mach number and assumes $\gamma = 1.40$ and $x^*/d = 0.8$.

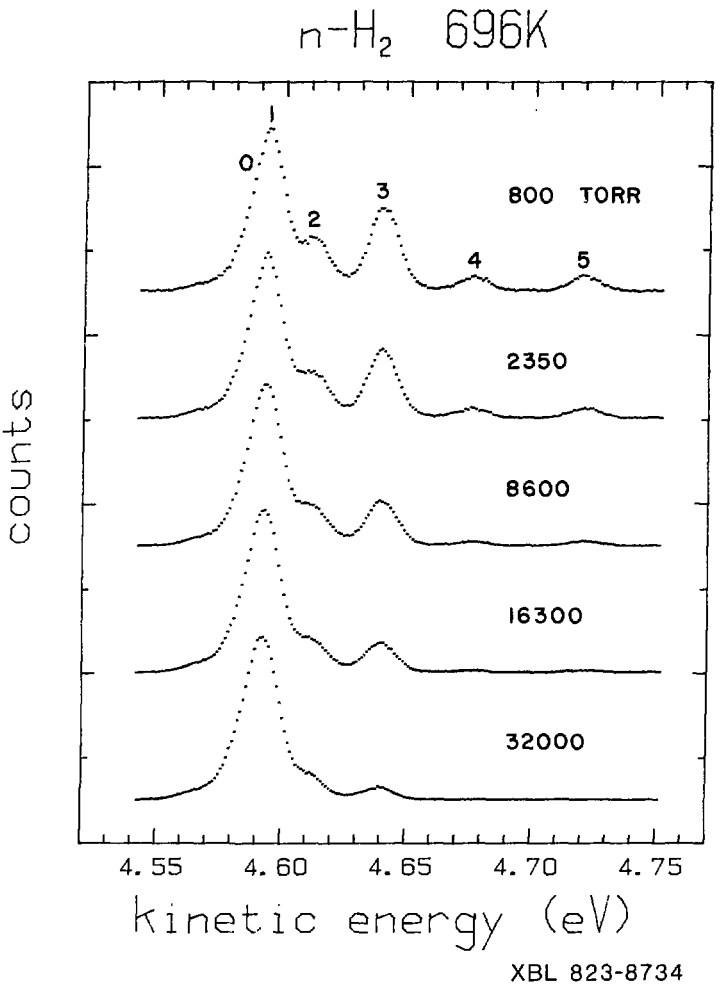
n-H2 696K
0
1
2
3
4
5
800 TORR
2350
8600
16300
32000
counts
4.55
4.60
4.65
4.70
4.75
kinetic energy (eV)
XBL 823-8734

Figure 1

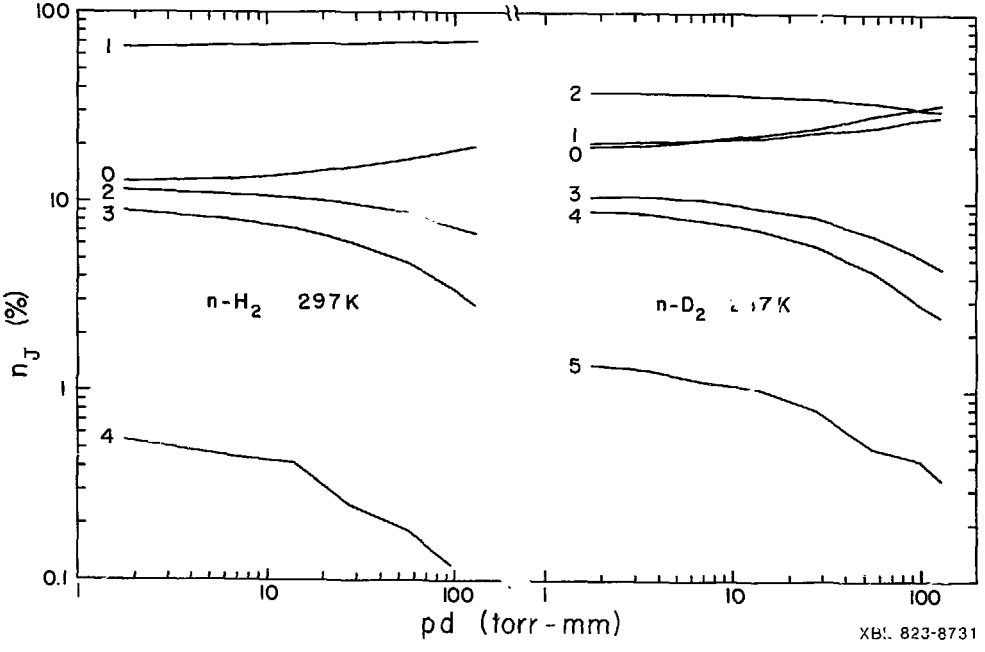
100
10
1
0.1
n_J (%)
1
0
2
3
4
n-H_2 297K
2
1
0
3
4
5
n-D_2
1
10
100
pd (torr-mm)
XBL 823-8731

Figure 2

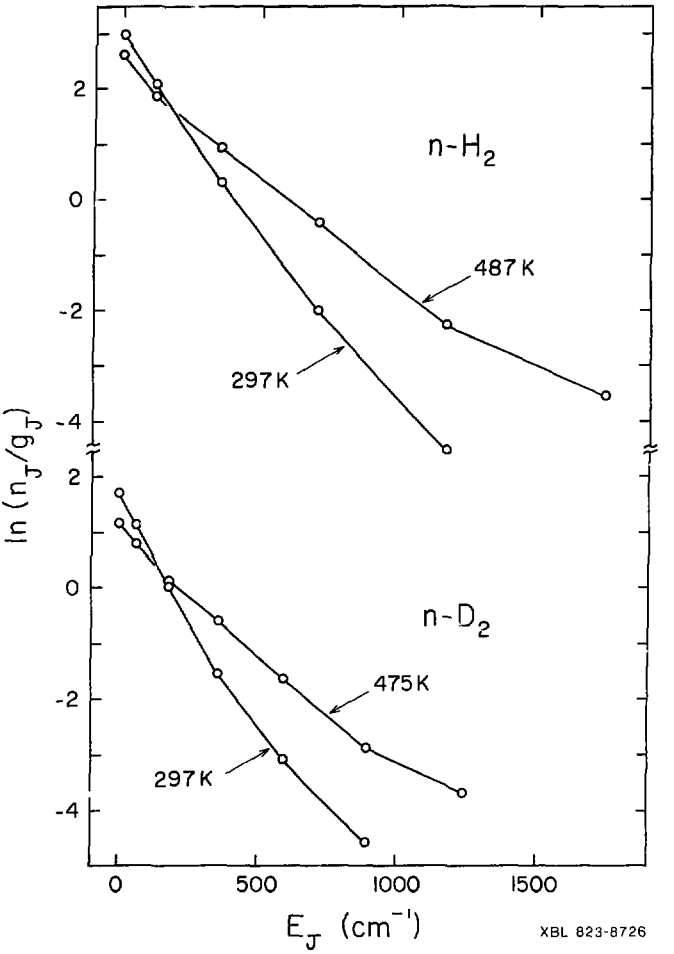
n-H2
487 K
297 K
n-D2
475 K
297 K
ln (nJ/gJ)
EJ (cm-1)
0
500
1000
1500
2
0
-2
-4
XBL 823-8726

Figure 3

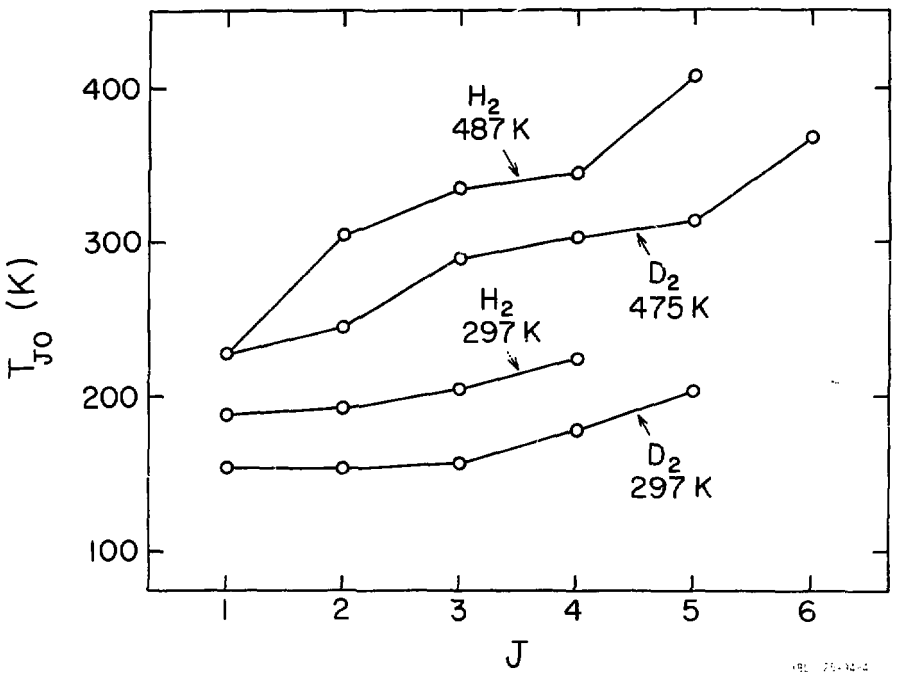

Figure 4

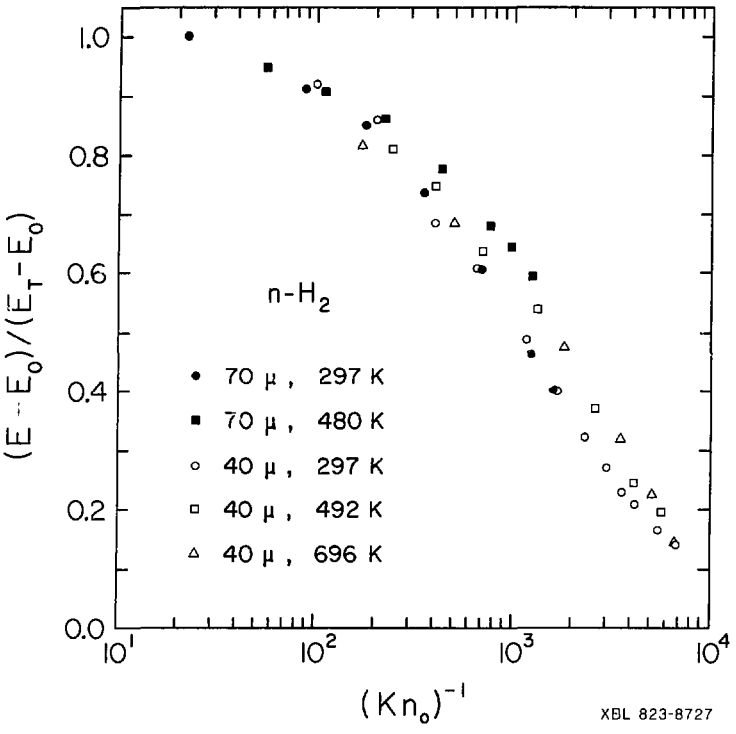
1.0
0.8
0.6
0.4
0.2
0.0
$(E - E_0)/(E_T - E_0)$
n-H_2
70 μ , 297 K
70 μ , 480 K
40 μ , 297 K
40 μ , 492 K
40 μ , 696 K
10^1
10^2
10^3
10^4
$(Kn_0)^{-1}$
XBL 823-8727

Figure 5

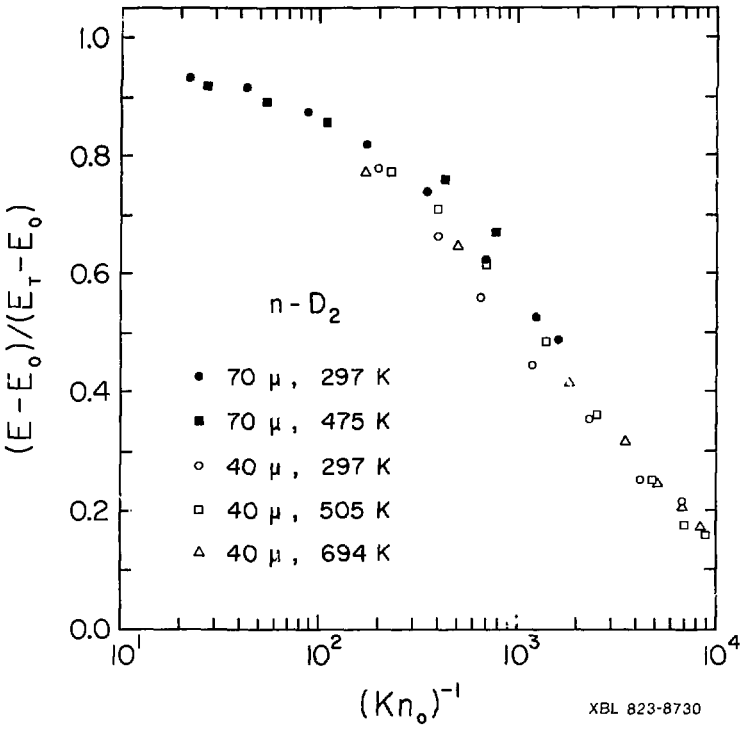
1.0
0.8
0.6
0.4
0.2
0.0
$(E-E_0)/(E_T-E_0)$
n - D_2
70 μ , 297 K
70 μ , 475 K
40 μ , 297 K
40 μ , 505 K
40 μ , 694 K
10^1
10^2
10^3
10^4
$(Kn_0)^{-1}$
XBL 823-8730

Figure 6

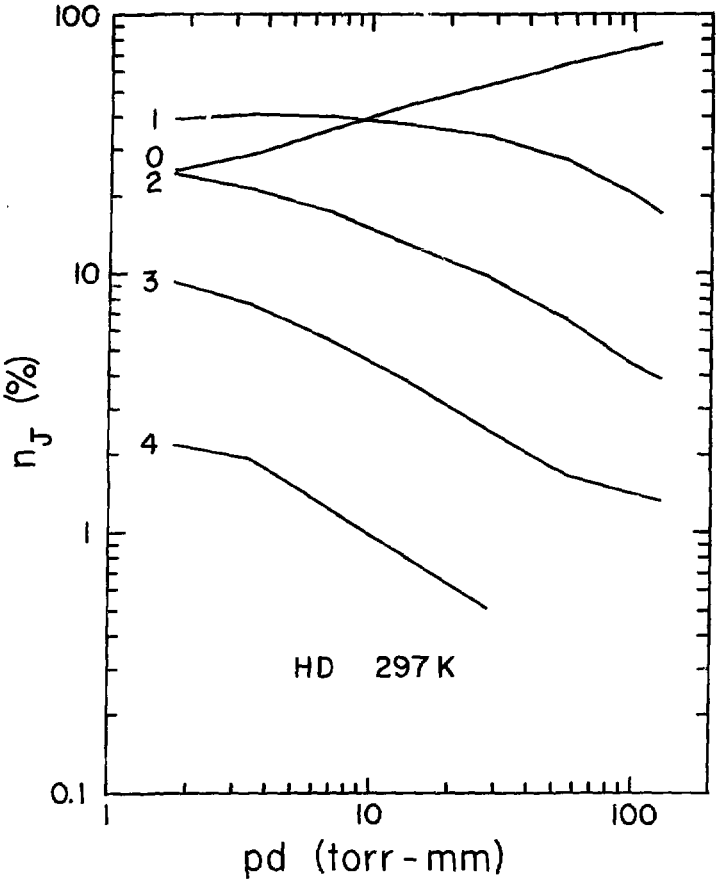

XBL 823-8733

Figure 7

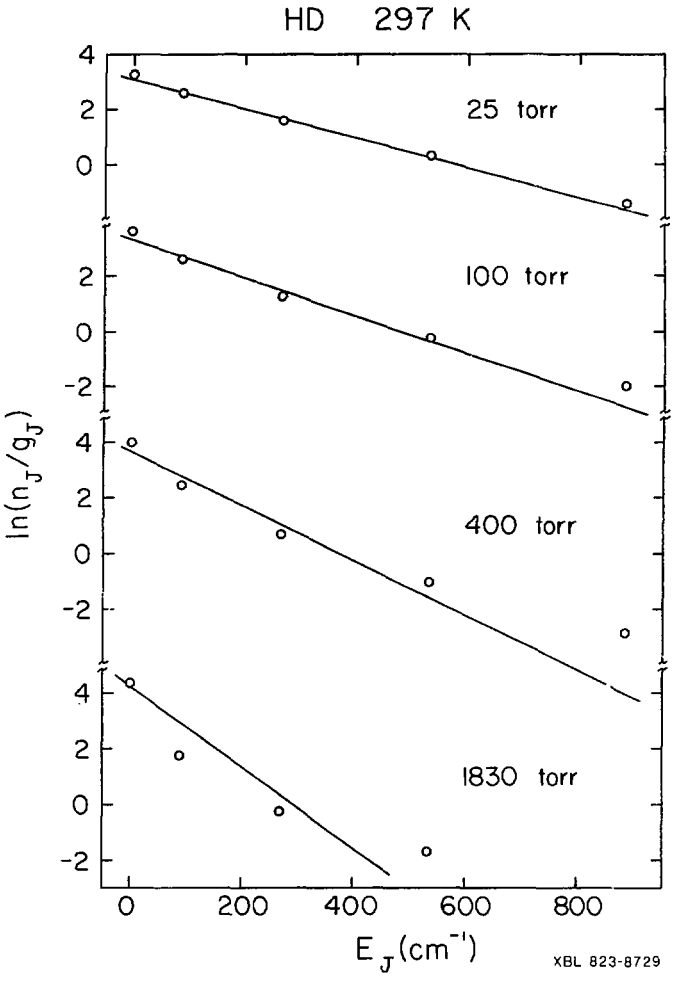
HD 297 K
25 torr
100 torr
400 torr
1830 torr
ln(n_J/g_J)
E_J (cm^-1)
0
200
400
600
800
XBL 823-8729

Figure 8

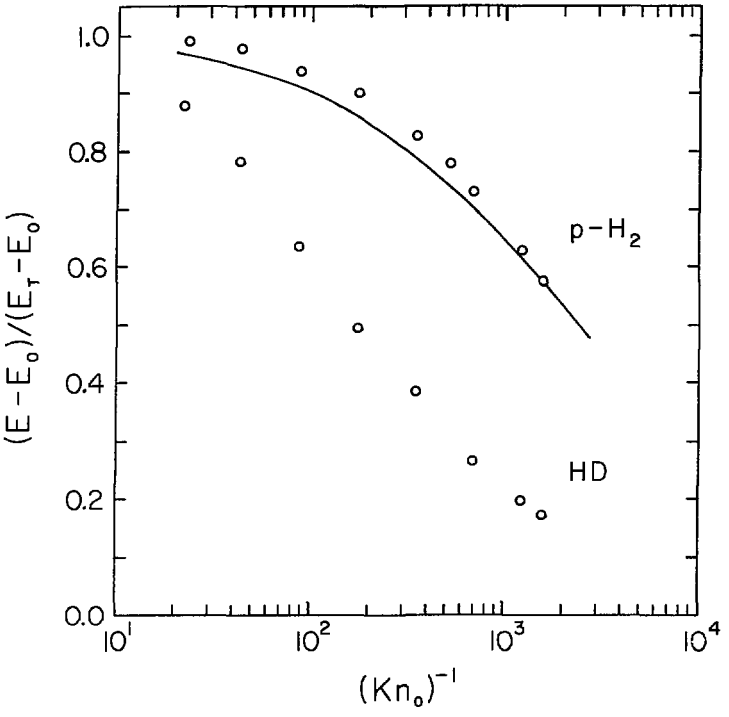

XBL 824-9113

Figure 9

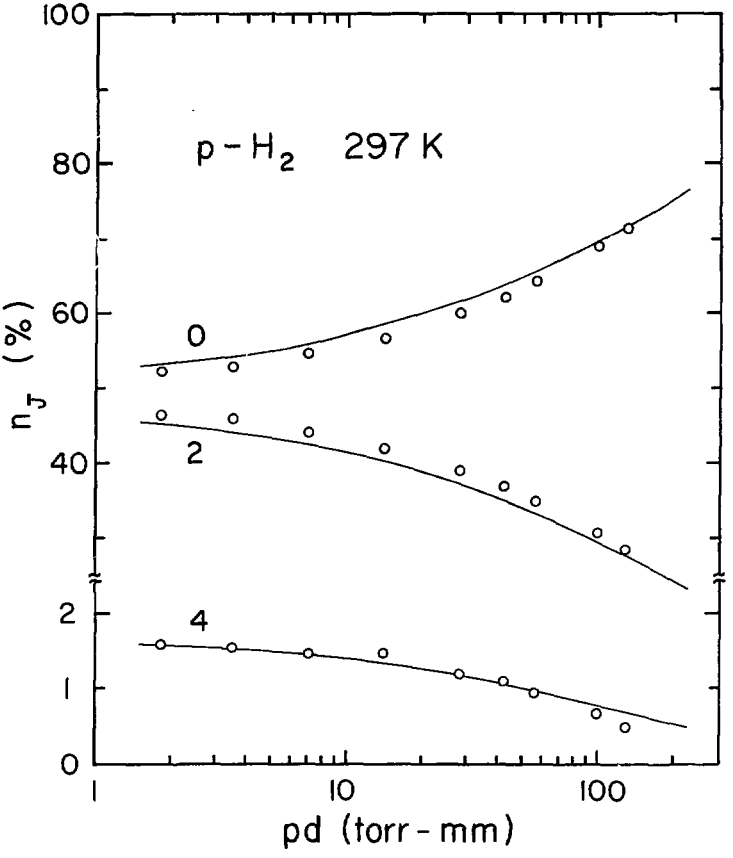

XBL 824-9114

Figure 10

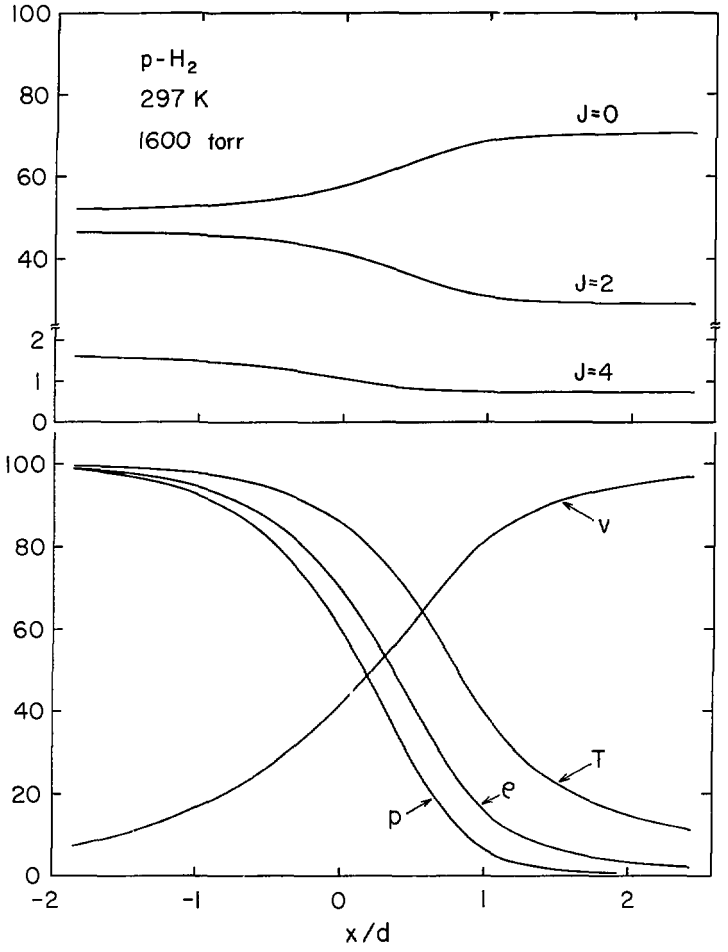

XBL 824-9112

Figure 11

VI. CONCLUSIONS

In this chapter I will give an evaluation of the performance of the apparatus and indicate what steps should be taken to improve on this prototype. It seems fair to say that many of the rather adventurous aspects of the design have worked out well, in spite of misgivings expressed by some of the visitors to our lab during the period of construction. The following points are particularly to be stressed:

1) The use of supersonic beams will be a necessity for future efforts in the realm of high resolution molecular photoelectron spectroscopy. We have demonstrated that the number density in the beam is adequate for the experiment and that the resolution is significantly enhanced by the elimination of Doppler and rotational broadenings.

2) The use of a double analyzer with an intermediate retarding lens has made a major improvement in the quality of the spectra by greatly reducing the troublesome background of stray electrons. The experiments reported here would have been seriously compromised without this feature.

3) Multichannel detection has made it feasible to obtain high resolution spectra typically in a matter of a few hours. An added benefit is the ease with which the instrument can be tuned up, by virtue of looking at a large energy window at all times.

4) The two-stage retarding/accelerating lens system has generally performed as designed, giving access to a wide range of pass energies and kinetic energies.

5) Constructing the electron optical elements from molybdenum-coated aluminum has the advantages of low cost, ease of machining, and light weight. A notable disadvantage is that the alignment surfaces are prone to damage by galling. Although we have not made a comparative study of the relative merits of Mo/Al and other standard materials, our experience suggests that this is a satisfactory surface preparation for low energy electron optics.

6) The vacuum system in the present instrument has several very desirable features. Molecular beam sampling eliminates the problem of pressure effects caused by photoelectrons scattering from the gas molecules. The analyzer and detector are maintained at ultrahigh vacuum while the experiment is running, thereby avoiding the problems of surface contamination and gain loss.

There nevertheless remain a few unsolved problems, some of which seem to be inherent in the design and some of which may yield to further efforts:

1) The kinetic energy offset is large. The electrons typically appear at 0.5 eV below their true kinetic energy, with the result that the very low energy portion of the spectrum is not observable. The photoelectrons are presumably retarded by 0.5 eV as they traverse the distance between the ionization region and the entrance slit of the analyzer. The offset becomes even larger if the beam source reducer is heated slightly.

2) The transmission of the analyzer is not as constant as we had hoped. The N_2 and CO spectra (described in Chapter III) indicate that the transmission probably changes by 20% over the region covered in the complete spectrum of hydrogen. Also, the transmission is rather low in the regions above 10 eV and below 0.5 eV kinetic energy.

3) The dispersion of the analyzer is less than expected at the lower pass energies. The observed resolution is thus worse than the theoretical resolution even when the electron beam is focused to the correct spot size at the entrance aperture of the hemispheres. This problem may be an effect of contact potentials or stray magnetic fields.

4) At low pass energy the signal is lost for the upper 20% of the energy window presented by the multichannel detector, presumably because the electron beam moves off the active area. This effect is likely the result of a stray magnetic field, because it is not as apparent at the higher pass energies. Another possible source is a physical misalignment of the lenses and analyzer.

5) The absence of an isolation valve on the analyzer requires that it be vented along with the rest of the chamber when performing routine maintenance on the lamp or beam source. This feature is at the very least a nuisance, and at worst it introduces the hazard of surface contamination after frequent pump-down cycles.

6) The assembly of the analyzer in its vacuum chamber is an awkward procedure and poses many risks of damage to the instrument. The problem stems in a large part from the complexity of the mumetal shielding and the arrangement for differentially pumping the analyzer.

7) The position encoding system currently requires 6 μsec to process each event, which limits the maximum random count rate to about 15 kHz. This is not a serious limitation for most experiments, but it does pose a problem when looking for features arising from clusters in the presence of an intense monomer signal.

I believe that a second generation apparatus could be made to work as well at 5–6 meV resolution as the present one works at 10–12 meV. The photon linewidth of the helium lamp would present a limitation at about 2–4 meV, which might be overcome in the future by high resolution VUV lasers or by very intense synchrotron radiation sources (neither of which are presently feasible, however). The route to better resolution is likely to be contained in the following points:

1) Construct a double analyzer with multichannel detection similar to the present one. The hemispheres could be somewhat larger (ca. 15 cm mean radius) if better magnetic shielding were devised.

2) Decrease the length of the electron flight path and simplify the design by using a single-stage kinetic energy scanning lens. This would likely restrict the operation to pass energies of 0.5 and 1.0 eV only, but the transmission function would be better behaved than at present. A shorter flight path would also permit the entire analyzer to be more compact and thereby fit within a single set of mumetal cans. These cans would be simpler to fabricate and would do a better job than the present shields which consist of multiple interlocking shapes. In addition the physical alignment of the lens and analyzer would be easier to achieve if the system were more compact.

3) Move the beam source further away and use UHV construction around the ionization region in order to overcome the problem of the kinetic energy offset. The reduced number density could be compensated to some extent by better pumping speed on the beam source exhaust chamber, thus permitting higher nozzle throughput.

4) Add a second stage of differential pumping on the beam source with an isolation valve that would be used to close off the ionization region and analyzer from the beam source for maintenance purposes. With an additional stage on the beam source there would be less need for keeping the analyzer and ionization chamber as separate vacuum regions. An enormous simplification in the design of the mumetal shields would be possible if the analyzer and ionization region were contained in single differential pumping region.

5) Increase the speed and accuracy of the position encoding system through the use of the newer wedge-and-strip metal anode designs.

ACKNOWLEDGMENTS

I would first like to thank my research director, Dave Shirley, for his support during my five years at LBL, and for providing me on many occasions with sage advice on both scientific and nonscientific questions.

I have also had the benefit of collaborating with Yuan Lee, who has frequently offered his technical expertise and given me much-needed encouragement.

Dennis Trevor has been my coworker since I arrived in Berkeley and has contributed to all aspects of the work described here. I am grateful as well for the efforts of my other coworkers on MBPES: Janice Reutt (since Fall 1980) and John Hepburn (on the laser experiment).

I wish to thank my immediate contemporaries in the Shirley group for their friendship and good humor. Among these are Rich Davis, Steve Kevan, Danny Rosenblatt, Steve Southworth, Jim Tobin, Chris Parks, Paul Kobrin, Dennis Lindle, Carlton Truesdale, Albert Baca, and Lennie Klebanoff. Special thanks go to John Barton and Charlie Bahr for help with computational problems.

Wini Heppler and Barbara Moriguchi have performed countless services essential to keeping the group operating under steady-state conditions.

I have been directly aided in my experimental work by numerous members of the LBL staff. Prominent among these are: Joe Katz, Dick Strudwick, and Brian Ng of Electronics Engineering; Dick Escobales,

Don Malone, and Warren Harnden of Mechanical Engineering; and Charlie Taylor, Larry Ornelas, Bert Watkins, Ed Voronin, Allan Susoeff, Will Lawrence, Karl Scheu, and Tom Gee of the Mechanical Shops.

I would like finally to thank my parents and family for their constant love, support, and understanding.

This work was supported by the Director, Office of Energy Research, Office of Basic Energy Sciences, Chemical Sciences Division of the U.S. Department of Energy under Contract No. DE-AC03-76SF00098.